EFFECTS OF FRONT-LOADING AND STAGGER ANGLE ON ENDWALL LOSSES OF HIGH LIFT LOW PRESSURE TURBINE VANES

DISSERTATION

M. Eric Lyall, Captain, USAF

AFIT/DS/ENY/12-05

DEPARTMENT OF THE AIR FORCE
AIR UNIVERSITY

AIR FORCE INSTITUTE OF TECHNOLOGY

Wright-Patterson Air Force Base, Ohio

AFIT/DS/ENY/12-05

EFFECTS OF FRONT-LOADING AND STAGGER ANGLE ON ENDWALL LOSSES OF HIGH LIFT LOW PRESSURE TURBINE VANES

DISSERTATION

Presented to the Faculty

Department of Aeronautical and Astronautical Engineering

Graduate School of Engineering and Management

Air Force Institute of Technology

Air University

Air Education and Training Command

In Partial Fulfillment of the Requirements for the

Degree of Doctor of Philosophy in Aeronautical Engineering

M. Eric Lyall, B.S.M.E, M.S.M.E

Captain, USAF

September 2012

AFIT/DS/ENY/12-05

EFFECTS OF FRONT-LOADING AND STAGGER ANGLE ON ENDWALL LOSSES OF HIGH LIFT LOW PRESSURE TURBINE VANES

M. Eric Lyall, B.S.M.E., M.S.M.E

Captain, USAF

Approved:

///SIGNED///	7 Sep 2012
Paul I. King	Date
///SIGNED///	5 Sep 2012
Marcus D. Polanka	Date
///SIGNED///	3 Sep 2012
David J. Bunker	Date
///SIGNED///	5 Sep 2012
Rolf Sondergaard	Date
///SIGNED///	7 Sep 2012
John P. Clark	Date

Accepted:

///SIGNED///	18 Sep 2012
M. U. Thomas	Date
Dean, Graduate School of Engineering and Management	

Abstract

Past efforts to reduce the airfoil count in low pressure turbines have produced high lift profiles with unacceptably high endwall loss. The purpose of the current work is to suggest alternative approaches for reducing endwall losses. The effects of the fluid mechanics and high lift profile geometry are considered. Mixing effects of the mean flow and turbulence fields are decoupled to show that mean flow shear in the endwall wake is negligible compared to turbulent shear, indicating that turbulence dissipation is the primary cause of total pressure loss. The mean endwall flow field does influence total pressure loss by causing excessive wake growth and perhaps outright separation on the suction surface. For equivalent stagger angles, a front-loaded high lift profile will produce less endwall loss than one aft-loaded, primarily by suppressing suction surface flow separation. Increasing the stagger setting, however, increases the endwall loss due to the static pressure field generating a stronger blockage relative to the incoming endwall boundary layer flow and causing a larger mass of fluid to become entrained in the horseshoe vortex. In short, front-loading the pressure distribution suppresses suction surface separation whereas limiting the stagger angle suppresses inlet boundary layer separation. Results of this work suggest that a front-loaded low stagger profile be used at the endwall to reduce the endwall loss.

Acknowledgements

First I want to thank God for blessing me in this life with a wonderful family and great people to work with. I know I don't really deserve what He's given me and I'm thankful for it.

Secondly, there are several folks that have helped so much that this document probably wouldn't have been written without them. My advisor Dr. Paul King spent many hours going over documents and challenging my work. On several occasions his advice got me over hard-to-climb hills that I probably couldn't have overcome on my own. I owe many thanks to Drs. Rolf Sondergaard and John Clark at AFRL. You both provided resources for the work and listened patiently to my random thoughts and ideas. You also gave good advice when I needed it. My other committee members, Drs. Marc Polanka and David Bunker, gave many insights into organizing the work and showing me weaknesses in how it's communicated and I'm grateful for that.

I also owe thanks to Stuart Benton of Ohio State that helped get the rig ready and for many discussions about endwall work (and occasionally politics☺). Jeff Downie of the Air Force Academy drew up and fabricated the fillet modification at the end of the research. I probably wouldn't have run that test without his help.

Finally, I want to thank my beautiful wife Laura and our three sons, Alex, Seth and Evan. They had so much patience with me when I was at home pondering about LPT endwall flows when I really shouldn't have been. I also want to thank my parents for teaching me to always do my best and what's right in life.

Table of Contents

List of Figures

Page

List of Tables

Page

Nomenclature

Symbols

a_{ij}	=	turbulence anisotropy tensor, $\langle u_i u_j \rangle - \frac{2}{3} k\delta_{ij}$, [$m^2/s^2$]
C_{ax}	=	axial chord, [m]
C_p	=	pressure coefficient, $C_p = (P_s - P_{s,in})/0.5\,\rho U_{in,st}^2$, []
$C\omega_s$	=	secondary vorticity coefficient, see Eq. (5.2), []
$\partial_s P_t$	=	non-dimensional total pressure change along local streamline, see Eq. 6.11, []
e	=	specific internal energy, [J/kg]
F_M	=	in-plane mean flow shear force parameter, see Eq. (6.17), []
F_T	=	in-plane turbulent shear force parameter, see Eq. (6.18), []
H	=	blade span, [m]
k	=	turbulent kinetic energy, $k = \langle u_i u_i \rangle/2$, [$m^2/s^2$]
L	=	turbulence integral length scale, [m]
M	=	Mach number, []
$\vec{n}$	=	unit vector in mean flow direction, []
P_s	=	static pressure, [N/m^2]
P_t	=	total pressure, [N/m^2]
Re	=	Reynolds number based on inlet velocity and axial chord, []
Re_θ	=	inlet boundary layer momentum thickness Reynolds number, []
S	=	cascade pitchwise spacing, [m]
SS_L	=	suction surface length, [m]
S_{ij}	=	instantaneous strain rate tensor, $\left(\frac{\partial v_j}{\partial x_i} + \frac{\partial v_i}{\partial v_j}\right)/2$, [1/s]
s_{ij}	=	fluctuation strain rate tensor, $\left(\frac{\partial u_j}{\partial x_i} + \frac{\partial u_i}{\partial v_j}\right)/2$, [1/s]
t	=	time variable, [s]
Tu	=	turbulence intensity, $\sqrt{< u^2 >}/U \times 100\%$, []
U	=	mean velocity in x-direction, [m/s]
u	=	velocity fluctuation in x-direction, [m/s]
V	=	mean velocity in y-direction, [m/s]
V_s	=	mean velocity in y_s direction, [m/s]
v	=	instantaneous velocity for Cartesian index notation, fluctuation velocity in y-direction [m/s]
W	=	mean velocity in z-direction, [m/s]
w	=	fluctuation velocity in z-direction, [m/s]
x	=	distance, usually in the axial coordinate direction, [m]

x_s	=	distance, profile suction surface coordinate or main flow direction coordinate of secondary flow coordinate system, depends on context, [m]
y	=	distance, usually in the pitchwise coordinate direction, [m]
y_s	=	distance, transverse direction of main flow in secondary flow coordinate system, orthogonal to spanwise direction, [m]
Y	=	total pressure loss coefficient, $Y = \left(P_{t,in} - P_t\right)/0.5\,\rho U_{in,st}^2$, []
Y_{2D}	=	pitch-normalized profile loss coefficient, usually based on mass-averaging Y, []
Y_{ps}	=	span and pitch-normalized full passage loss coefficient, usually based on mass-averaging Y, []
Y_{ew}	=	endwall loss coefficient, $Y_{ps} - Y_{2D}$, []
z	=	distance, usually in the spanwise direction, [m]
Z_{TE}	=	penetration height of endwall flow along the airfoil span at the trailing edge, [m]
Z_w	=	Zweifel parameter, $Z_w = 2\left(\frac{S}{C_{ax}}\right)\cos^2\alpha_{ex}\left(\tan\alpha_{in} - \tan\alpha_{ex}\right)$, []

Greek

α	=	cascade gas angle, [˚]
δ_{ij}	=	identity tensor, []
δ_{99}	=	99% boundary layer thickness [m]
λ	=	profile stagger setting, [˚]
μ	=	dynamic viscosity, $\left[\text{kg/m}\cdot\text{s}\right]$
ε_{ijk}	=	alternating unit tensor, []
ρ	=	density, [kg/m^3]
τ	=	wall shear stress, [N/m^2]
υ	=	kinematic viscosity, [m^2/s]
ω	=	turbulence specific dissipation, vorticity, [1/s]

Subscripts

ex	=	exit location
i,j,k	=	Cartesian indices, can be 1, 2, or 3
in	=	inlet location
ps	=	peak suction or passage, depends on context
s	=	secondary coordinate system
st	=	streamwise direction
x,y,z	=	cascade x, y, and z directions
w	=	wall

Operators

$\frac{D(\ )}{Dt}$	=	substantial derivative
Δ	=	differencing operator
∇	=	vector gradient operator
$< >, \langle\ \rangle$	=	angle brackets indicate a time-averaging operator
$\lVert\ \rVert$	=	vector magnitude
$\lvert\ \rvert$	=	absolute value
$\vec{\ }$	=	arrow over variable indicates vector
$\times$	=	vector cross product

Acronyms

AFIT	=	Air Force Institute of Technology
AFRL	=	Air Force Research Laboratory
BLFP	=	boundary layer force parameter, see Eq. 3.10, []
RANS	=	Reynolds-averaged Navier-Stokes
CFD	=	computational fluid dynamics
DNS	=	direct numerical simulation
IMF	=	non-dimensional irreversible mean force, see Table 6.1, []
ITF	=	non-dimensional irreversible turbulent force, see Table 6.1, []
LPT	=	low pressure turbine
PS	=	pressure surface
RANS	=	Reynolds averaged Navier-Stokes
RMF	=	non-dimensional reversible mean force, see Table 6.1, []
RTF	=	non-dimensional reversible turbulent force, see Table 6.1, []
SKE	=	secondary kinetic energy, Eq. 2.1 [m^2/s^2]
SS	=	suction surface
TDAAS	=	turbine design and analysis system
TKE	=	turbulent kinetic energy, $\langle u_i u_i \rangle/2$, [$m^2/s^2$]
USAF	=	United States Air Force
2D	=	two-dimensional
3D	=	three-dimensional

EFFECTS OF FRONT-LOADING AND STAGGER ANGLE ON ENDWALL LOSSES OF HIGH LIFT LOW PRESSURE TURBINE VANES

1. Introduction

The low pressure turbine (LPT) in modern high bypass ratio aero-engines is a vital component that is central in determining overall engine performance and efficiency. Howell et al. (2002) reported that the LPT-driven fan produces up to 80% of engine thrust and the LPT can contribute to as much as a third of the overall engine weight. Recently, there has been increased interest in high lift LPT airfoils to reduce weight. The increased aerodynamic loading, however, results in more highly curved airfoils that potentially have stronger adverse pressure gradients on the suction surface, causing stall Reynolds numbers to increase. The challenge is to reduce the blade count in the LPT while maintaining good efficiency over the operational Reynolds number range.

Since LPT airfoils tend to have large aspect ratios (span to axial chord ratios), most high lift LPT research has focused on profile (midspan) performance while neglecting endwall effects. Both McQuilling (2007) and Praisner et al. (2008) demonstrated improved low Reynolds number profile performance for high lift designs with more than 38% higher loading than a conventionally loaded baseline design, designated Pack B. In both studies, good low Reynolds number performance was achieved for the high lift designs by using more front-loaded pressure distributions compared to Pack B (i.e., peak suction occurred closer to the leading edge than for Pack B). Praisner et al. (2008) also demonstrated for a high lift design, designated Pack DF which has 25% higher aerodynamic loading than Pack B, that increasing the loading level can lead to unacceptably high endwall loss.

1.1 The Need for an Improved Understanding of Endwall Loss

Elevated endwall loss limits the practical loading levels of high lift LPT profiles. Several passive flow control methodologies have been attempted to reduce endwall loss, including boundary layer fences, leading edge modifications, profile-endwall fillets, and non-axisymmetric endwall contouring. Although these concepts are quite different, they all attempt to manipulate the vortex structures of the endwall flow to reduce the total pressure loss. Among these flow control techniques, the literature reports that non-axisymmetric endwall contouring has been the primary technique applied to high lift LPT profiles. Praisner et al. (2008) and Knezevici et al. (2009) found, however, that the endwall loss remained beyond practical limits for the high lift Pack DF profile, even after implementing non-axisymmetric endwall contouring. Other approaches may need to be considered to reduce the endwall loss of high lift designs to acceptable levels.

As will be shown in the literature review, endwall loss is still not fully understood, thus hindering the development of endwall loss reduction techniques. An improved understanding of endwall loss is needed to support future endwall loss reduction research.

1.2 Research Objectives

The objective of the present research was to investigate the cause of elevated endwall loss of high lift profiles and to recommend design changes that might reduce the losses of such designs. This study focuses on two major aspects of endwall loss production. First is the physics of freestream mixing and loss production in the endwall flow at the differential fluid element level, considering the roles of the mean and

turbulent flow fields. Secondly are the effects of high lift profile geometry on endwall loss.

As will be shown, turbulent shear is the dominant cause of mixing loss in the endwall flow. The mean flow components of the vortex structures contribute negligibly to the mixing loss. Rather than mixing, the mean flow components of the vortex structures cause excessive growth of the suction surface boundary layer, and possibly separation.

The profile shape strongly influences separation effects due to the endwall flow, which can be reduced with front-loaded pressure distributions. It will be shown that the profile stagger angle influences inlet endwall boundary layer separation, with high stagger settings promoting separation and high endwall loss. Past high lift profiles usually had high stagger settings, which may partially explain the excessive endwall loss. In the present study, results suggest that low stagger front-loaded profile designs may provide reduced endwall loss compared to past high lift designs that tended to be front-loaded with high stagger settings.

The overall dissertation is organized as follows. Chapter 2 reviews the relevant literature, focusing on the description of typical endwall flow fields, effect of the pressure loading distribution, loss mechanism studies, and endwall loss reduction techniques. Chapter 3 shows the research profiles used in this study to explain the differences between high and conventional lift profiles. Chapters 4 and 5 focus on experimental and computational methods, respectively. Chapter 6 provides a detailed discussion of the fluid mechanics of endwall loss production. Chapters 7 and 8 discuss high lift geometric effects on endwall loss, the pressure loading distribution and stagger angle, respectively.

Chapter 9 presents the design and application of an airfoil modification used to apply front-loading and low stagger angle at the endwall to reduce the endwall loss. Chapter 10 includes a summary of the results with conclusions and recommendations for future work. Several appendices are also included at the end of the document and are called out in the body of the text to provide additional details regarding the work.

2. Literature Review

This chapter provides a discussion of the relevant literature pertaining to LPT endwall flow and loss generation. Being most relevant to the present research, the discussion will focus on the following topics: endwall flow field, loss mechanism studies, effect of the pressure loading distribution, and loss reduction techniques. This review highlights key findings and conclusions from the literature.

2.1 Description of the Endwall Flow Field

Endwall flow formation is well documented so only a brief discussion will be given here. Several variations of endwall flow models exist but I will only consider the dominant features, shown in Fig. 2.1 using the model of Sharma and Butler (1987). As shown upstream of the leading edge, the inlet endwall boundary layer separates, forming a horseshoe vortex. The pressure side leg of the horseshoe vortex is swept across the passage towards the adjacent suction surface by the cross passage pressure gradient, eventually becoming the passage vortex. The passage vortex climbs the suction surface and separates as it rotates. Meanwhile, the suction side leg of the horseshoe vortex remains close to the suction surface and rotates in opposite sense to the passage vortex. Sharma and Butler (1987) also point out that the suction side leg may orbit around the axis of the passage vortex. In the literature, the terms secondary flow and endwall flow are used interchangeably as generic names for the collective flow patterns just described. Regarding loss production, Fig. 2.1 suggests that flow separation at the inlet and on the suction surface will give rise to mixing losses within and downstream of the blade row. Keep in mind, however, that friction on the profile and endwall also represents a source

of loss and will be driven by the wetted area of the blade row. The following section provides a more detailed discussion of endwall loss mechanisms.

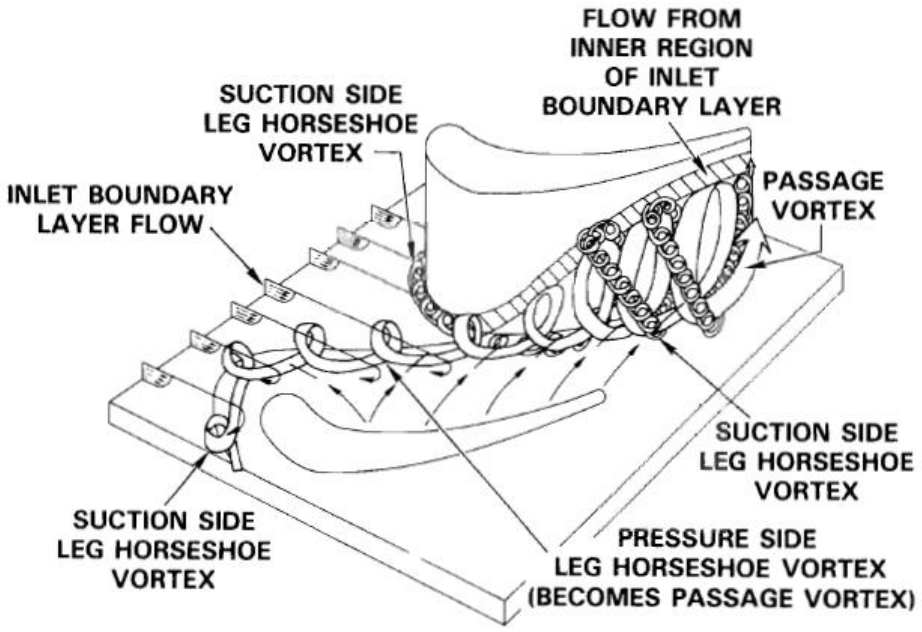

Fig. 2.1 Endwall flow model of Sharma and Bulter (1987)

2.2 Endwall Loss Mechanism Studies

The cause of total pressure loss can broadly be categorized into two groups: boundary layer friction effects and freestream mixing effects. Harrison (1990) investigated the influence of wall friction on total pressure loss. That author used an analytical expression to obtain the local dissipation within the blade and endwall surface boundary layers, based on velocity measurements at the edge of the boundary layers. Harrison (1990) found that dissipation in the boundary layers reasonably accounted for the measured through-passage total pressure loss up to approximately $0.84C_{ax}$, after which the technique underpredicted the measured loss. The technique was most accurate

prior to peak suction. Furthermore, the estimated loss incurred from mixing out the flow to a uniform state from a plane $0.23C_{ax}$ downstream of the blade row was over a quarter of the measured loss coefficient at that location, indicating the importance of mixing effects in loss generation.

Mixing effects may have a larger contribution to the total losses of high lift profiles compared to conventional lift profiles. The reason is that for high lift profiles, the pitchwise spacing between blades is larger, indicating reduced total wetted area but with a higher fraction at the endwall where secondary flows are produced. Several studies have investigated freestream mixing effects, focusing mainly on dissipation of the vortical structures by studying the secondary kinetic energy (SKE) and the role of turbulence. This section presents both topics. Although such studies have provided some insight into loss production, they do not provide insight into how to reduce the endwall loss.

For the mean flow field, the rotational energy at the endwall is typically quantified by the magnitude of SKE. Using the mass-averaged exit flow angle, or the mean camber line angle at the trailing edge as the primary reference direction (depending on the researcher), SKE is defined as half the sum of squared mean velocity components normal to the primary reference direction. The mathematical definition is given as,

$$\mathrm{SKE} = \frac{1}{2}\left(V_s^2 + W^2\right). \tag{2.1}$$

Moore and Adhye (1985) measured SKE at three downstream planes of a low speed linear turbine cascade. They suggested that the increased loss is almost entirely explained by a decrease in SKE at downstream planes. More recently, MacIsaac et al. (2010) also reported endwall flow loss development downstream of a low speed linear

turbine cascade. They observed that reduction in SKE only accounted for 42% and 64% of the mixing losses in the second and third downstream mixing planes, respectively.

The differing conclusions of these two studies regarding SKE may be due to boundary conditions. It is worth noting that the Moore and Adhye (1985) cascade had an aspect ratio of unity, whereas the MacIsaac et al. (2010) cascade had an aspect ratio of 2.8. Besides incompressible flow, no other geometric or flow conditions were matched. The significant differences in test conditions provide a good pair of test cases for assessing the utility of SKE as an indicator of passage loss. The differing conclusions suggest that SKE may not be a good indicator of measured losses. I do not present SKE measurements in the present study.

Studies focusing on the role of turbulence have shed more light on endwall loss production than ones focusing on SKE. Moore et al. (1987) studied turbulent Reynolds stresses in downstream mixing in a low speed linear turbine cascade. They found that the integrated deformation work term that exchanges mean flow kinetic energy and TKE (also called the turbulence production term) agreed very closely with the rate of total pressure loss production. MacIsaac et al. (2010) also studied turbulence production in downstream measurement planes of a low speed linear turbine cascade. Their results supported Moore et al. (1987), in that turbulence production plays a significant role in the mixing process and loss production. MacIsaac et al. (2010) pointed out that the magnitude of the turbulence production term should be comparable to the dissipation term.

In summary, losses are generated due to friction on solid surfaces and freestream mixing within and downstream of the blade row. For high lift profiles that have less total

wetted area than conventional lift designs, it is suggested that freestream mixing may have a more important role in loss production than for conventional lift profiles. In the freestream, turbulence has an important role in the mixing process, yet the role of the mean flow structures in loss production is unclear. We know, however, that the SKE of the mean flow structures will be dissipated downstream of the blade row. Although Moore et al. (1987) and MacIsaac et al. (2010) demonstrated a link between freestream turbulence and mixing loss through use of the turbulence production term, the governing equation they used precludes decoupling local mixing effects. Thus, I present an alternative approach in Chapter 6 to study the fluid mechanics of loss production that includes both mean flow and turbulence effects. Appendix A presents a comparison of the current approach with that of Moore et al. (1987) and MacIsaac et al. (2010). I discuss the effect of the pressure loading distribution on endwall loss in the following section.

2.3 Effect of the Pressure Loading Distribution

The pressure loading distribution is an important geometric parameter for high lift LPT airfoils, primarily because it is manipulated to preserve low Reynolds number performance (cf., McQuilling (2007) and Praisner et al. (2008)). For high lift LPT airfoils, front-loading the pressure distribution increases stall resistance at low Re. Front-loading can be achieved in two ways, increasing the stagger angle (Korakianitis, 1993) or for a fixed stagger angle, thickening the leading edge (Korakianitis and Papagiannidis, 1993).

Several studies in the literature have concluded that front-loading increases endwall loss, including those of Weiss and Fottner (1995), Zoric et al. (2007), Praisner et al. (2008), and Knezivici et al. (2009). The front-loaded profiles in all of those studies were designed with increased stagger settings compared to the companion aft-loaded profiles. No studies in the literature have considered the effect of the pressure loading distribution for profiles with fixed stagger angles. As will be shown in Chapter 7, front-loading reduces the endwall loss of profiles with fixed stagger angles. The following section discusses endwall loss reduction techniques. Appendix B discusses several endwall loss correlations that indicate other geometric features influencing endwall loss, such as overall gas turning, passage acceleration and aspect ratio.

2.4 Endwall Loss Reduction Techniques

Several passive flow control methods have been used for reducing endwall loss, including boundary layer fences, endwall contouring, and leading edge bulbs and fillets. For all of these methods, the goal is to favorably influence the development of the rotational component of the endwall flow in ways to reduce total pressure loss. The reasoning for using each method, however, can be quite different. Prümper (1972) proposed boundary layer fences as a means of hindering the cross passage boundary layer flow and reducing endwall loss. Harvey et al. (2000) implemented nonaxisymmetric endwall contouring to reduce endwall total pressure loss. In this case, the cross passage pressure gradient was weakened to reduce the strength of the passage vortex. As described by Langston (2001), the concept of leading edge bulbs is to strengthen the counter vortex, which has the opposite sense of the passage vortex, thus weakening the

overall vortex system that comprises the endwall flow. On the other hand, Zess and Thole (2002) showed that a leading edge fillet can reduce or eliminate the horseshoe vortex that forms as the inlet boundary layer separates. Becz et al. (2003) showed that in their cascade, a leading edge bulb and fillet produced nearly the same aerodynamic loss reduction. Only nonaxisymmetric endwall contouring has been applied to high lift LPT profiles with aerodynamic loading levels as high as those of the current study.

In summary, several methods can be found in the literature to mitigate endwall losses. Nonaxisymmetric endwall contouring is the primary method reported for reducing the endwall loss of high lift LPT profiles. What all of these methods have in common is that they attempt to manipulate the vortex structures in a favorable way to reduce the endwall loss. As will be shown in Chapter 9, the emphasis of the current work is on reducing flow separation and not on manipulating the vortex structures. Reducing flow separation, however, will influence vortices by reducing the amount of fluid they contain.

2.5 Uniqueness of the Current Research

There are several aspects of endwall loss that are not well understood, including the fluid mechanics and profile geometry effects. First are the roles of the mean and turbulent flow fields in mixing loss production. A strong correlation has been found between turbulence production and total pressure loss, but the role of the mean flow structures in generating total pressure loss is unclear. In the present study, a method is presented to analytically decouple the roles of the mean and turbulent flow fields. It will be shown that mean flow shear is negligible, even inside the vortex cores with relatively

strong vorticity. Additionally, experimental flow field and loss measurements using profile boundary layer fences suggest that mean flow structures have a role in causing flow separation from the profile. (Separated flows cause elevated mixing losses.)

The effects of pressure loading distribution and stagger angle are not well understood. Benner et al. (2006b) suggested that a high stagger angle mimics a front-loaded pressure distribution, while Korakianitis and Papagiannidis (1993) show that front-loading can be achieved by thickening the profile near the leading edge. In the present study, the effects of pressure distribution and stagger setting are treated separately. It is suggested that a front-loaded profile with fixed stagger setting reduces endwall loss but increased stagger angle increases endwall loss.

Unlike past studies that have attempted to manipulate and reduce endwall losses of high lift profiles, the focus of the current work is to recommend profile shapes that have lower endwall loss given high loading levels. A loss reduction method that focuses on the airfoil can be combined with endwall contouring methods to obtain acceptable performance while maintaining high lift. The research profiles used in the current study are presented in the following chapter.

3. Research Profiles and Reynolds Lapse

In this chapter I describe the research profiles used in the current study. These profiles were designed at the Propulsion Directorate of the Air Force Research Laboratory for studying high lift and low Reynolds number LPT aerodynamics. Endwall effects were neglected during design but as will be shown in Chapters 6 through 9, endwall loss significantly influences the overall performance. A goal of the current work is to understand the implications on endwall loss of design choices made based on midspan performance. All profiles of the current study were designed to the approximate gas angles of the Pratt & Whitney Pack B profile, differing mainly by the aerodynamic loading level, pressure loading distribution and stagger setting.

The first section presents the cascade nomenclature and important non-dimensional parameters. Discussed next are the differences between the research profiles, including low Reynolds number performance. Finally I derive a boundary layer force parameter (BLFP) that explains why some profiles perform well at low Reynolds numbers and others do not.

3.1 Nomenclature and Non-dimensional Parameters

The cascade nomenclature used in the following discussion is shown in Fig. 3.1. The sign convention of the flow angles is consistent with Wilson and Korakianitis (1998). The stagger setting, λ, is defined as a positive angle. The cascade Reynolds number is defined as,

$$\mathrm{Re} = \frac{\rho U_{in,st} C_{ax}}{\mu}. \tag{3.1}$$

As Re decreases, the suction surface boundary layer thickens, increasing the pressure loss and the likelihood of stalling the profile. Losses across the blade row are described with total pressure loss coefficients,

$$Y = \frac{P_{t,in} - P_{t,ex}}{P_{t,in} - P_{s,in}}. \tag{3.2}$$

The dependency of average Y on Re is commonly referred to as the Reynolds lapse. The pressure loading distribution around profiles is described using static pressure coefficients,

$$Cp = \frac{P_s - P_{s,in}}{P_{t,in} - P_{s,in}}. \tag{3.3}$$

The aerodynamic loading level is typically characterized by the Zweifel loading coefficient,

$$Z_w = 2\left(\frac{S}{C_{ax}}\right)\cos^2\alpha_{ex}\left(\tan\alpha_{in} - \tan\alpha_{ex}\right). \tag{3.4}$$

Equation (3.4) shows that for profiles with the same flow angles and C_{ax}, Z_w primarily describes the pitchwise spacing of cascades, S. For engines, blade rows with large values of Z_w will require fewer airfoils, thus providing weight and cost reductions through the need for fewer precision castings.

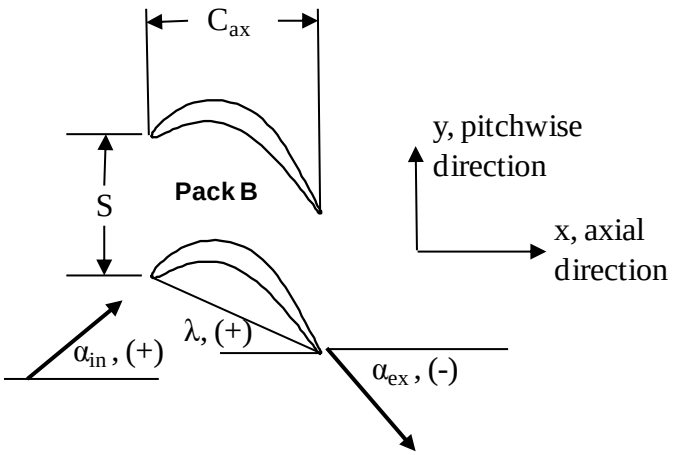

Fig. 3.1 Cascade definitions

The current work supports the goal of increasing Z_w while maintaining levels of Y consistent with conventionally loaded profiles. Hill and Peterson (1992) stated that the optimum spacing for maximum efficiency typically leads to $Z_w = 0.8$. The trend in research has been to increase the optimum level of Z_w. Wilson and Korakianitis (1998) specified a range of practical loading levels as $0.9 < Z_w < 1.2$. As shown in the following section, the current study focuses on profiles with loading levels in the range of $1.13 \leq Z_w \leq 1.59$.

3.2 Description of Research Profiles

The profiles used in the current study are shown in Fig. 3.2. The Pratt & Whittney Pack B profile represents a conventional lift baseline design, with $Z_w = 1.13$ and within the range recommended by Wilson and Korakianitis (1998). Workers at AFRL/RQTT produced the L1 and L2-series profiles using the Turbine Design and Analysis System (TDAAS). TDAAS employs the Wildcat code of Dorney and Davis (1992), coupled with the separated flow laminar-turbulent transition model of Praisner

and Clark (2007) for calculating the performance of design iterations. McQuilling (2007) documented the design process for L2F, but the same procedure was applied for the other research profiles: L1A, L1M, and L2A.

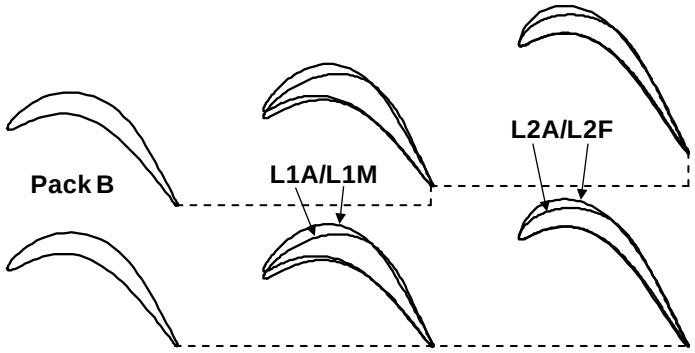

Fig. 3.2 Diagram of research profiles

Relevant geometric and aerodynamic properties are shown in Table 3.1. I used the LEO code, discussed later in Chapter 5, for calculating the flow angles. The pair of L1 profiles, representing the first level increase in loading, has 14% larger pitchwise spacing than Pack B. L1A is an aft-loaded profile whereas L1M is considered mid-loaded. Aft, mid or forward loading refers to the location in the passage where peak suction occurs (i.e., for a front loaded profile peak suction occurs closer to the leading edge than an aft-loaded profile). The pair of L2 profiles, representing the second level increase in loading, has 38% larger pitchwise spacing than Pack B. L2A is considered aft-loaded whereas L2F is front-loaded. The stagger settings of the Pack B and L1-series profiles (see Table 3.1) are consistent with the recommendations of Kacker and Okapuu (1982). The stagger setting of the L2-series profiles, however, is approximately 8.7˚ larger than for the Pack B and L1-series.

Table 3.1 Research profile geometric and aerodynamic properties (The flow angles were computed using the Leo code.)

	Pack B	L1A	L1M	L2A	L2F
S/C_{ax}	0.885	1.011	1.011	1.221	1.221
α_{in}, deg	35.00	35.00	35.00	35.00	35.00
α_{ex}, deg	-58.48	-57.40	-57.63	-57.77	-58.12
λ, deg	25.90	23.50	25.80	34.60	34.60
Z_w	1.13	1.33	1.32	1.59	1.57

The pressure loadings of the research profiles, obtained with fully turbulent calculations using the LEO code, are shown in Fig. 3.3. With peak suction approximately at $0.65C_{ax}$, the baseline Pack B profile is aft-loaded. The L1A profile is also aft-loaded with peak suction just beyond $0.60C_{ax}$. The L1M profile, however, has peak suction near $0.50C_{ax}$ indicating mid-loading. Peak suction occurs approximately at $0.60C_{ax}$ and $0.25C_{ax}$ for L2A and L2F, respectively, indicating aft and forward-loading for these two profiles.

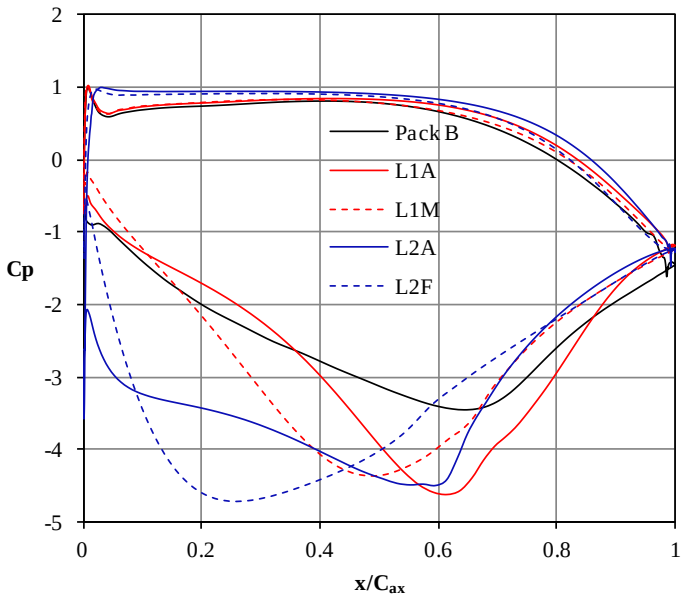

Fig. 3.3 Research profile pressure loading distributions

The Reynolds lapse of the research profiles is shown in Fig. 3.4. All Reynolds lapse data were acquired in the AFRL low speed wind tunnel with inlet turbulence levels between 3% and 4%. Only data for the L2A and L2F profiles in Fig. 3.4 were acquired as part of the current study. I discuss the tunnel setup for acquiring the L2A and L2F Reynolds lapse data in Appendix C. Consistent with all profiles in Fig. 3.4 is that the loss increases with decreasing Reynolds number. The suction surface boundary layer thickens with decreasing Reynolds number, making the profiles more susceptible to flow separation. For the Pack B profile, Y_{2D} begins to grow rapidly below Re = 52,500. The sudden change in slope of the Reynolds lapse is commonly referred to as the "knee" of the lapse curve. For increased loading levels, it is desirable to preserve the low Reynolds number performance of conventionally loaded profiles. The L1A profile has the loss knee occurring at about Re = 70,000 and performs poorly at low Re. The loss knee of L1M is approximately at Re = 59,000, yet the profile loss does not exceed that of Pack B until Re < 50,000. The loss knee of L2A is nearly the same as for Pack B at Re = 50,000, but the loss increases more rapidly with decreasing Re for L2A. The most notable result of Fig. 3.4 is that the best performing profile is L2F, despite 38% larger pitchwise spacing than Pack B.

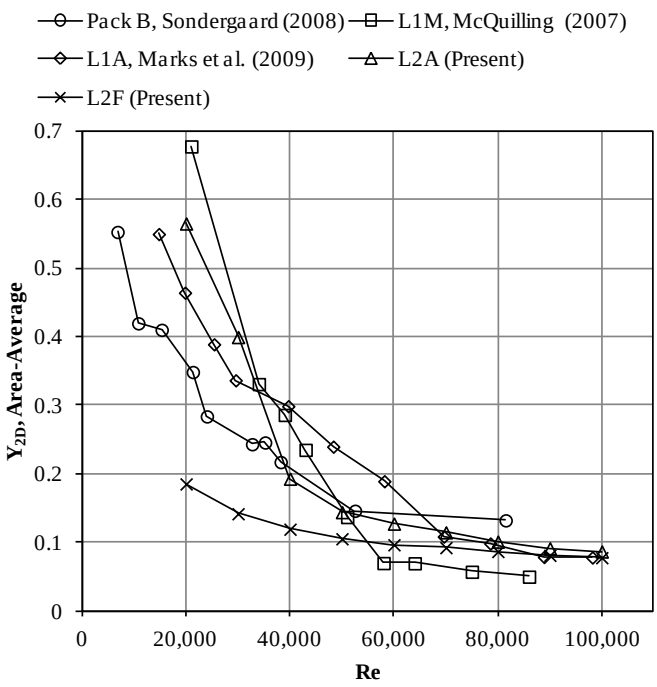

Fig. 3.4 Research profile Reynolds lapse

The pressure loadings of Fig. 3.3 provide insight into the differences between the lapse curves of Fig. 3.4. In general, aft loaded profiles tend to have relatively short diffusion lengths on the suction surface, thus strengthening the adverse pressure gradients to increase boundary layer growth at low Re. On the other hand, front loaded profiles tend to have longer diffusion lengths with weaker adverse pressure gradients, improving performance at low Re. Differences in low Re performance, however, cannot be fully explained by the pressure loading distributions. As shown in Fig. 3.3 for Pack B and L2F, peak suction occurs at $0.65C_{ax}$ and $0.25C_{ax}$, respectively. The Pack B and L2F adverse pressure gradients appear to be of similar strength, yet L2F performs much better at low Re. In the following section I derive a parameter to give more insight into differences in profile performance at low Re.

3.3 Derivation of the Boundary Layer Force Parameter (BLFP)

The BLFP number derived in this section gives insight into stall resistance and provides a measure of how forward or aft-loaded a profile is. Before starting the derivation, first consider that high lift LPT profiles commonly operate with closed separation bubbles on the suction surface. Praisner and Clark (2007) formulated a separated flow transition model to predict the length of the separation bubble as a function of momentum thickness Reynolds number just prior to separation. Their model relied on the premise that the length of the separation bubble scales with the state of the boundary layer at separation. Furthermore, their model suggests that thinner boundary layers with higher wall shear stress will produce smaller separation bubbles, thus making profiles more stall resistant. This idea can be extended by considering that the adverse pressure gradient eventually drives the wall shear to zero as the separation bubble forms. Thus, a scale parameter that compares the friction force in the boundary layer prior to peak suction to the adverse pressure gradient aft of peak suction may provide insight into stall resistance of LPT profiles.

Factors influencing the suction surface boundary layer are shown in Fig. 3.5 along with variables that will be used in deriving the boundary layer force parameter (BLFP). The BLFP number is written as,

$$\mathrm{BLFP} = \frac{\dfrac{\tau_{w,ps}}{\delta_{99,ps}}}{\dfrac{P_{s,ex} - P_{s,ps}}{SS_L - x_{ps}}}, \tag{3.5}$$

where $\tau_{w,ps}$ is the wall shear stress, $\delta_{99,ps}$ is the 99% boundary layer thickness, $P_{s,ex} - P_{s,ps}$ is the pressure rise from peak suction to the trailing edge, and $SS_L - x_{ps}$ is the suction

surface distance from peak suction to the trailing edge. Using flat plate similarity solutions to provide scales for the friction force (cf., Schlichting and Gersten, 2000),

$$\frac{\tau_{w,ps}}{\delta_{99,ps}} \approx \frac{\rho\, U_{ps}^2}{x_{ps}}. \tag{3.6}$$

Using static pressure coefficients,

$$P_{s,ex} - P_{s,ps} = \left(Cp_{ex} - Cp_{ps}\right)\frac{\rho U_{in,st}^2}{2}. \tag{3.7}$$

Combining Eqs. (3.6) and (3.7),

$$BLFP = \frac{\left(SS_L - x_{ps}\right)}{x_{ps}\left(Cp_{ex} - Cp_{ps}\right)}\frac{U_{ps}^2}{U_{in,st}^2}. \tag{3.8}$$

Assuming inviscid flow for a streamline with flow accelerating from $U_{in,st}$ to U_{ps},

$$\frac{U_{ps}^2}{U_{st,in}^2} = 1 - Cp_{ps}. \tag{3.9}$$

Substituting Eq. (3.9) into Eq. (3.8) and rearranging, the final form of BLFP is,

$$BLFP = \frac{\left(1 - Cp_{ps}\right)\left(1 - x_{ps}/SS_L\right)}{x_{ps}/SS_L\left(Cp_{ex} - Cp_{ps}\right)}. \tag{3.10}$$

Given the surface coordinates of the profile and the pressure loading distribution, the BLFP number can be calculated for any airfoil. The suction surface can be defined starting from the stagnation point near the leading edge out to the maximum axial coordinate. For convenience, the minimum axial coordinate is usually near the stagnation point and will also work well as the starting point for defining the suction surface. Due to difficulties in computing Cp values at trailing edges, Cp_{ex} can be defined using the exit static pressure downstream of the blade row. In the following discussion of BLFP numbers for the research profiles, the suction surface is defined using the minimum and

maximum axial coordinates of the profiles. I calculated the Cp_{ps} values using the data of Fig. 3.3 and the outlet static pressure of LEO predictions to compute Cp_{ex} values. Although the LEO calculations were viscous, inviscid Cp predictions will also work for calculating BLFP numbers.

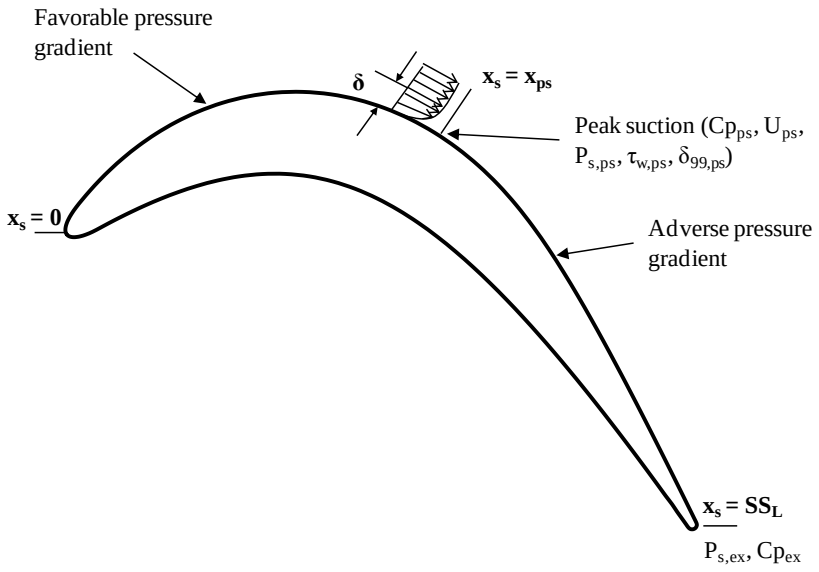

Fig. 3.5 Diagram of factors influencing the suction surface boundary layer

The BLFP number is plotted against x_{ps}/SS_L in Fig. 3.6 using the Pack B and L2F Cp values to show the effects of the pressure loading distribution and aerodynamic loading level. As shown, BLFP increases significantly with decreasing x_{ps}/SS_L, or equivalently as profiles become more front-loaded. The reason is that the boundary layer becomes much thinner as the suction peak moves closer to the leading edge, increasing the wall shear prior to peak suction. The increased loading level of L2F shifts the overall curve below the Pack B curve. Peak suction for L2F and Pack B, however, are at 23% and 52.5% of the suction surface length, respectively, resulting in an L2F BLFP number

more than twice that of Pack B. As a result, the good low Reynolds number performance of L2F shown in Fig. 3.4 is likely attributed to an extremely thin boundary layer on the suction surface prior to peak suction. Presumably, separated flow laminar-turbulent transition and subsequent reattachment occurs more easily given the thin boundary layer upstream of the separation bubble. As will be shown in Chapter 7, L2F has a separation bubble for Re as high as Re = 100,000. McQuilling (2007), however, was unable to detect a separation bubble for L2F with hot-wire probes 1mm from the suction surface for a test blade with C_{ax} = 152.4 mm.

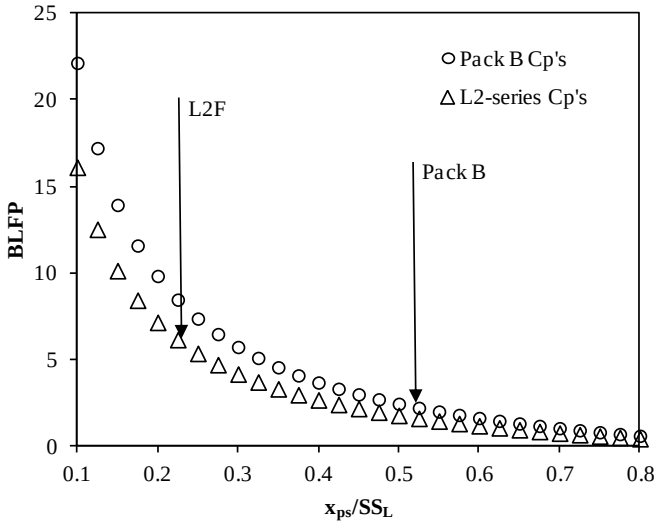

Fig. 3.6 Dependence of BLFP on location of peak suction, x_{ps}/SS_L

The BLFP numbers for all of the research profiles discussed so far are shown in Fig. 3.7. It is useful to compare the magnitude of the BLFP numbers to the knees of the lapse curves in Fig. 3.4. As shown in Fig. 3.7, L1A has the smallest BLFP number, correlating to the highest Re loss knee compared to the other profiles, at approximately Re = 70,000. The knees in the lapse curves of Fig. 3.4 are similar for Pack B, L1M and

L2A, correlating to a narrow spread of BLFP numbers for these profiles. The L2F BLFP number is twice that of L1M, the profile with the next highest BLFP number. Accordingly, L2F performs best at low Re.

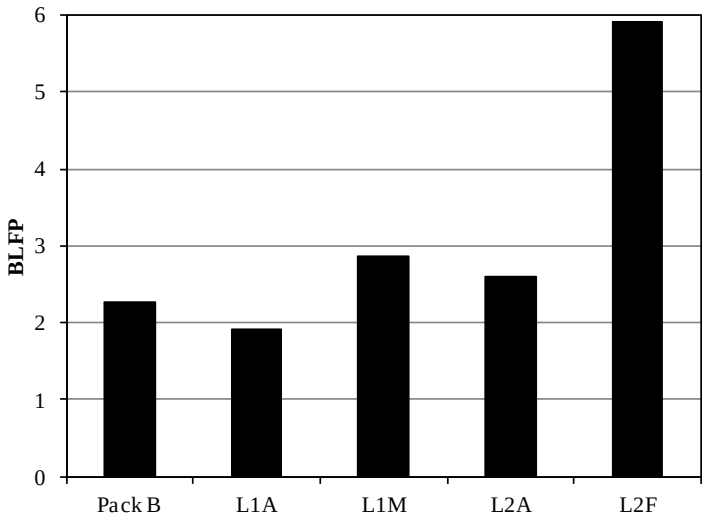

Fig. 3.7 Comparison of BLFP numbers between research profiles (BLFP is strongly dependent on the location of peak suction, x_{ps}/SS_L.)

A practical application of the BLFP number is for profile design. The idea is to manipulate the profile shape to match the BLFP number of another profile with known desirable Reynolds lapse performance to achieve good performance with the new profile. Appendix K documents this approach for designing a new profile to achieve low Re performance similar to L2F while also limiting the endwall loss. The BLFP number also provides a quantifiable measure of how front or aft-loaded a profile is.

3.4 Chapter Summary

High lift profiles can be designed that preserve or even improve upon the midspan low Reynolds number performance of conventional lift profiles. The L2F profile with 38% larger pitchwise spacing than Pack B performed much better at low Reynolds

number. L2F performs better than Pack B due to being significantly more front-loaded. Geometrically, L2F is thicker near the leading edge with a stagger setting 8.7˚larger than Pack B. As will be shown in Chapter 8, calculations using LEO unfortunately suggest that L2F has approximately 37% higher endwall loss at design than Pack B, consistent with the experiments of Zoric et al. (2007). Furthermore, it is suggested in Chapter 8 that the elevated endwall loss of L2F is attributed to the high stagger setting. Endwall loss should be considered for designing profiles.

4. Experimental Methodology

This chapter presents the experimental setup for acquiring endwall flow measurements, mixing forces, loss measurements and surface flow visualizations. The first section discusses the wind tunnel configuration and the position behind the blades where measurements were taken. The following sections discuss the instrumentation and associated experimental uncertainties.

4.1 AFRL Low Speed Wind Tunnel

The experiments were conducted in the AFRL low speed wind tunnel facility located at Wright-Patterson Air Force Base. This wind tunnel is an open loop induction type, with the flow that enters a bell-mouth contraction passing through a turbulence-generating grid, through the cascade and exiting via a fan. The turbulence grid is comprised of a lattice of horizontal and vertical 25.4 mm round bars, with 76.2 mm center spacing. The turbulence grid produces a turbulence intensity of $Tu_{in,st}$ = 3.0%, with an integral scale of $L_{in,st}$ = 39.4 mm at about $1.4C_{ax}$ upstream of the cascade, where C_{ax} is blade axial chord. The center blade of the cascade is approximately 90 bar diameters downstream of the grid.

A schematic of the test section is shown in Fig. 4.1. The cascade is comprised of seven airfoils. The outer tailboard and end-flow adjusters are used to obtain periodic inlet conditions. A splitter plate assembly provides inlet boundary layer control for endwall studies. The distance between the splitter plate and the tunnel roof creates an effective span to axial chord ratio of 3.5. The splitter inlet plate leading edge was designed

according to the recommendations of Narasimha and Prasad (1994). Note that the splitter plate assembly is described in more detail in Appendix D.

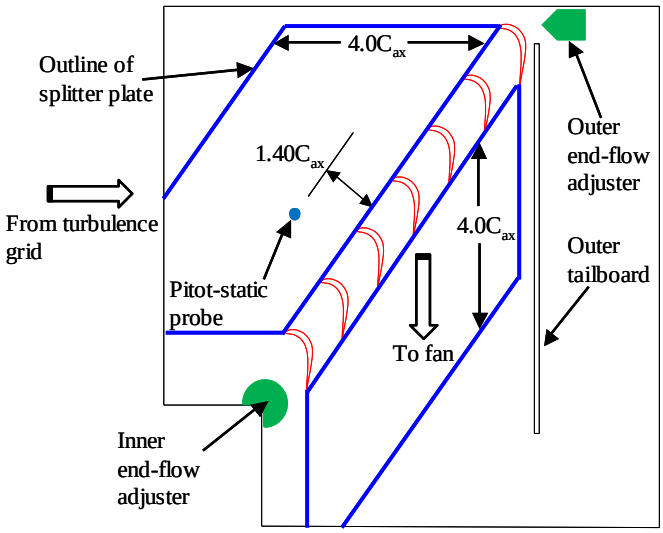

Fig. 4.1 Schematic of AFRL low speed wind tunnel test section

Figure 4.2 shows the cascade and secondary flow coordinate systems. The secondary coordinate system is indicated with the subscript s and rotated 58˚ off axial, the predicted mean profile exit flow angle for L2A and L2F (See Table 3.1). Exit measurements were taken 0.58C_{ax} downstream of the blade row, placing the center airfoil wake near the middle of the measurement plane. Table 4.1 summarizes the cascade geometry and flow conditions. One notes in Table 4.1 that the inlet boundary layer thickness is quite small. Though the inlet boundary layer thickness will influence the size of the horseshoe vortex and the overall measured losses downstream of the blade row, this work focuses on the physics of how losses are generated and differences in loss between profiles. Hence, the effect of the boundary layer thickness is not emphasized. Nevertheless, the inlet boundary layer thickness is consistent among the test profiles for both experiments and CFD.

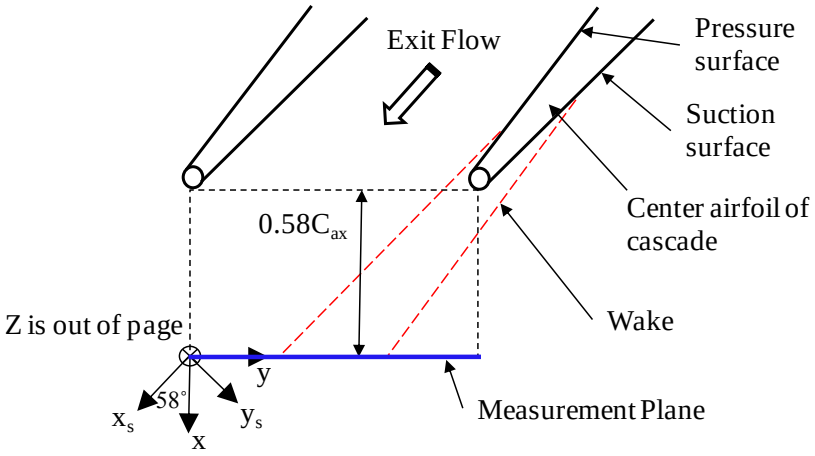

Fig. 4.2 Schematic depicting the cascade and secondary flow (subscript s) coordinate system definitions

Table 4.1 Cascade Geometry and Flow Properties

Cascade Geometry		
Axial chord, C_{ax}	152.4 mm	
Pitch/axial chord, S/C_{ax}	1.221	
Span/axial chord, H/C_{ax}	3.5	
Inlet Turbulence Conditions, $1.4C_{ax}$ upstream		
Turbulence Intensity, $Tu_{in,st}$	3.0%	
Streamwise integral scale, $L_{in,st}$	$0.26C_{ax}$	
Inlet Flow Conditions, $1.4C_{ax}$ upstream		
Re, ($U_{in,st}$ and C_{ax})	100,000	
Mach number, M_{in}	0.03	
Inlet boundary layer parameters, $1.4C_{ax}$ upstream		
δ_{99}/H	0.025	
Re_θ	655	
Shape factor	2.2	
Flow Angles	**L2A**	**L2F**
Inlet flow angle (from axial), α_{in}	35˚	35˚
Predicted mean profile exit angle (Table 3.1), α_{ex}	-57.77˚	-58.12˚
Measured mean passage exit flow angle, α_{ex}	-55.1˚	-58.4˚

4.2 Instrumentation

Except for ambient pressures, data were sampled using National Instruments hardware and software. An upstream stationary pitot-static probe and a kiel probe in the exit measurement plane were used to measure total pressure loss. A custom in-line kiel probe was designed for use in this study and is described in more detail in Appendix E. At 3.2 mm diameter, the kiel probe was less than 2% of the cascade pitch, providing

sufficient resolution within the wakes. I used Druck LPM 5481 pressure transducers, calibrated using a Ruska 7250LP laboratory standard (the reported accuracy is within 0.16% of the inlet dynamic head at Re = 100,000), to measure total pressure differences across the blade row and the inlet dynamic head. The ambient pressure was measured with a laboratory barometer, and freestream fluid temperatures were measured using type J thermocouples. An IFA300 constant temperature anemometer was used with single normal hot-film probes (TSI 1210-20 and 1211-20) for obtaining velocities and turbulence measurements at the inlet. The velocities for setting the inlet Reynolds number were measured using the upstream pitot-static probe. A TSI 1299-18-20 triple sensor hot-film probe was used to obtain velocity and turbulence measurements downstream of the blade row. The three sensors of the triple probe were contained within a 2 mm measurement diameter. The probe stem was 4.6 mm in diameter.

All hot-film probes were calibrated using a TSI Model 1127 velocity calibrator. Typical calibration curves included 18 points, spanning the measured velocity range in the experiment. Calibrations spanned $2 < U < 14$ m/s and $5 < U < 29$ m/s for inlet and exit measurements, respectively. During calibration, the triple sensor probe was placed in a zero pitch/yaw configuration for the entire velocity range. An analytical technique, similar to that described by Lekakis et al. (1989), combined with the table look-up procedure of Gieseke and Guezennec (1993) was used for obtaining velocity magnitudes and angles, given effective cooling velocities. The triple sensor hot-film probe data reduction procedure is described in more detail in Appendix F. In the experiment, average flow angles relative to the probe axis were typically within 10˚. Angle

measurements on the calibration stand were within ± 0.9˚ of the actual velocity vector for ±18˚ pitch and yaw, indicating reasonable bias error.

A mixture of one part black chalk line chalk to approximately 20 parts mineral oil was used for suction surface flow visualization on the center blade of the cascade. The color of the blades was beige, so the black chalk provided a good contrast using a halogen lamp for illumination. The camera used for capturing images was mounted to view through a hole in the outer tailboard (see Fig. 4.1), orienting the suction surface nearly orthogonal to line of sight of the camera. I provide a more detailed discussion of the flow visualization test procedures in Appendix G.

4.3 Experimental Uncertainty

All uncertainties were estimated at 95% confidence. Uncertainties for the Reynolds number and total pressure loss coefficients were estimated using the partial derivative and root-sum-square method of Kline and McClintock (1953). The loss coefficients at each point were estimated to within ± 0.01, approximately 1% of the inlet dynamic head. The Reynolds number was estimated to be within about 1% of the measured value. The uncertainty of mean velocities for the exit flow field was estimated to be within 1.5% of the measured values. Sampling times were also sufficiently long to ensure independence of the samples in the presence of unsteadiness. When acquiring data for computing three-dimensional mixing forces that are discussed later in Chapter 6, it was important to limit the precision error to allow quality gradient calculations within the turbulence field. Approximately 7,000 independent samples were acquired at each

measurement location to limit the mean-square fluctuation to within 3.5% of the measured values.

Three-dimensional mixing forces were obtained from triple sensor hot-film measurements. Derivatives were calculated using second order centered finite differences given by Tannehill et al. (1997) for three-point stencils without interpolation between measurement points. For computing the derivatives, the grid spacing was set at $\Delta x = 0.083C_{ax}$, $\Delta y = 0.028C_{ax}$, and $\Delta z = 0.042C_{ax}$ with the center of the stencil within the measurement plane of Fig. 4.2. Forty-five independent quantities comprised of velocity and turbulence measurements were required to compute $\partial_s P_t$ at a single position, risking elevated precision uncertainty. (Note that $\partial_s P_t$ is the non-dimensional rate of change of total pressure along the local streamline used to study mixing forces, defined later in Eq. 6.11.) The uncertainty in $\partial_s P_t$ was estimated using the sequential perturbation technique of Moffat (1988). Results of $\partial_s P_t$ with 95% confidence bands at 20% span for L2A, along with total pressure loss coefficients for reference are shown in Fig. 4.3. Positive and negative $\partial_s P_t$ indicates energy addition to and extraction from the mean flow, respectively. As will be shown in Chapter 6, the differences in the mixing forces that sum together to give $\partial_s P_t$ are larger than the error bars, indicating that meaningful conclusions can be obtained regarding the role of the different mixing forces. The Reynolds stress measurements had the largest uncertainty.

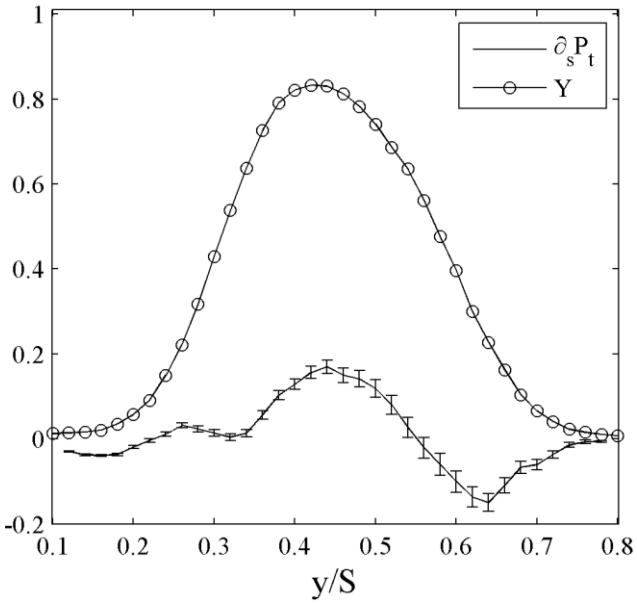

Fig. 4.3 L2A $\partial_s P_t$ and Y measurements at 20% span

5. Computational Methodology

In this study CFD results are used to investigate profile geometry effects on endwall loss. First discussed in this chapter are the grid generator and flow solver, followed by a discussion of benchmarking and limitations of the CFD analysis.

5.1 Grid Generator and Flow Solver

The grid generator and flow solver are the codes WAND and LEO, respectively, available through ADS (Aerodynamic Solutions Inc., 2012). These codes were developed specifically for turbomachinery applications. WAND functions as the preprocessor, generating the computational grid and assigning boundary conditions for use with the flow solver LEO.

WAND produces multi-block structured grids for both 2D and 3D applications, an example of which is shown in Fig. 5.1 with the blocks segregated by color. The grid shown has an OHH topology with an O-grid used for discretizing the blade boundary layer and H-grids above and below the profile for discretizing the freestream. Additional blocks are included for resolving effects near the leading and trailing edges. Although Fig. 5.1 shows a 2D grid, 3D grids are generated using multiple planes of 2D grids stacked along the span, referred to as k-planes. For both 2D and 3D flow domains, grids are stretched and smoothed using elliptic PDE methods to better capture gradients in the flow.

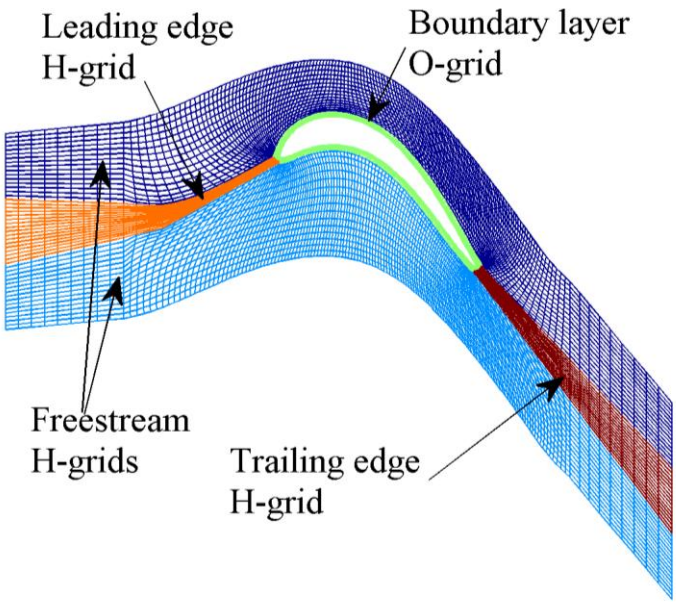

Fig. 5.1 Structured 2D grid of L2F flow domain generated using WAND (11,813 mesh points)

Figure 5.2 shows the results of a grid independence study using the L2F passage total pressure loss, Y_{ps}, at Re = 100,000 (includes endwall effects). Total pressure loss is the figure of merit for evaluating grid independence because it is a direct indicator of the presence of numerical dissipation (i.e., entropy generation due to the grid), a critical issue in CFD (Hirsch, 2007). Furthermore, airfoils in this study are compared based on loss production. As shown, the results are essentially grid-independent with 544,065 mesh points. For all meshes the y^+ levels on the walls are less than unity. One notes for the coarsest mesh that Y_{ps} is only +3.5% different than Y_{ps} of the finest mesh, suggesting that numerical dissipation due to the grid is quite small. Nevertheless, I ran all cases discussed later in Chapters 7 through 9 using the finest grid having 767,845 mesh points.

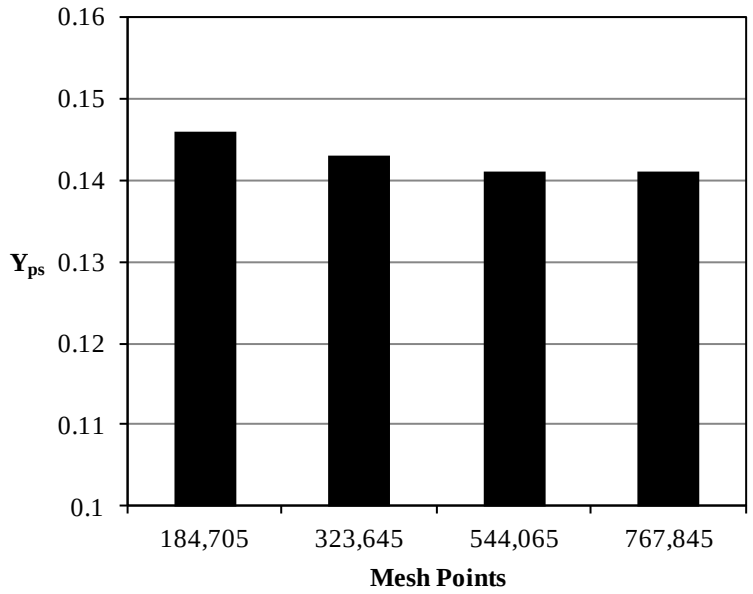

Fig. 5.2 Results of the grid independence study using the L2F passage loss, Re = 100,000

LEO requires an inlet Mach number (M_{in}), total pressure ($P_{t,in}$), and an outlet static pressure ($P_{s,ex}$) as flow field boundary conditions. I set M_{in} = 0.15 for all cases, resulting in M_{ex} = 0.23. Note that M_{ex} = 0.053 in the experiment for Re = 100,000. The purpose of increased M_{ex} for the CFD was to reduce stiffness of the governing equations, thus accelerating convergence while maintaining incompressible flow. The $P_{t,in}$ and $P_{s,ex}$ settings adjusted the Reynolds number by manipulating the fluid density instead of the inlet velocity, which was set by M_{in}. WAND also requires an inlet boundary layer thickness for modeling the endwall flow, which was set to 2.5% span, consistent with the experiments.

Turbulence effects are modeled in LEO via the Wilcox (1998) k-ω model, thus requiring turbulent boundary conditions at the inlet. I set the inlet turbulence intensity to $Tu_{in,st}$ = 1% and the integral length scale to $L_{in,st} = 0.0017C_{ax}$ for all cases. Note, however, that these turbulent boundary conditions are quite different than the

experimental values of $Tu_{in,st}$ = 3.0% and $L_{in,st} = 0.26C_{ax}$ given in Table 4.1 for the endwall experiments. Using experimental values of $Tu_{in,st}$ and $L_{in,st}$ resulted in profile loss predictions significantly higher than the experimental values, primarily due to excessive turbulent diffusion of the boundary layers. Wilcox (2006) shows that the k-ω model is sensitive to finite freestream boundary conditions, so appropriate values had to be chosen for the flows in this study. Appendix H contains a more detailed discussion of the sensitivity of the k-ω model to the inlet boundary conditions and the choice of boundary conditions used in this study.

The flow solver LEO is a compressible finite volume code. The code employs a cell-vertex discretization scheme that is 2^{nd} order accurate in space. Time integration can be for either steady or time accurate simulations. For the current study that focuses on single blade rows, all solutions are steady. For convergence acceleration the code employs local time stepping and multi-grid techniques. The code also uses a preconditioner to reduce stiffness of the governing equations and accelerate convergence for low Mach number flows. The following section discusses the strengths and weaknesses of the CFD analysis using LEO.

5.2 Benchmarking and Limitations of the CFD Analysis

Turbulence modeling remains a challenge in CFD. In fact, turbulence models are often blamed when computational predictions are inaccurate. For LPT flows with Re values in the range considered in the current study, profile boundary layers tend to be transitional, increasing the complexity of the problem. Harrison (1990) suggested that endwall boundary layer flows are also transitional. The LEO code provides options for

either the fully turbulent or transitional versions of the Wilcox (1998) k-ω turbulence model. This model is a two-equation eddy viscosity type. For flows considered in the current study, differences in pressure loss between the transitional and fully turbulent versions were negligible, so only results for the fully turbulent version are presented. As will be shown, LEO is suggestive of the way profiles operate at high Re and can be used for comparing profile designs. LEO, however, under-predicts the dependency of the pressure loss on Re and this is the primary limitation of the code. Both profile and endwall losses are considered.

Figure 5.3 compares the midspan Reynolds lapse of the L2F profile computed using LEO with experiment and two other codes, Fluent and Wildcat. For the commercial code Fluent, I selected for use the Walters and Leylek (2005) k-k_l-ω transitional turbulence model. This model is a three-equation eddy viscosity RANS type that was recently developed for turbomachinery flows. (Appendix I contains a discussion of the k-k_l-ω model and the computational methods using Fluent.) Dr. John Clark of AFRL/RQTT provided the predictions using Wildcat, the code used in AFRL/RQTT's turbine design and analysis system (TDAAS). The Wildcat code employs the separated flow transition model of Praisner and Clark (2007). As shown in Fig. 5.3, LEO agrees reasonably well with the experiments, but under-predicts the slope of the lapse curve. Fluent is quite accurate for Re > 50,000, but predicts stall prematurely for Re < 50,000. Wildcat is in good agreement with the experiments for all Re values with only a slight negative bias.

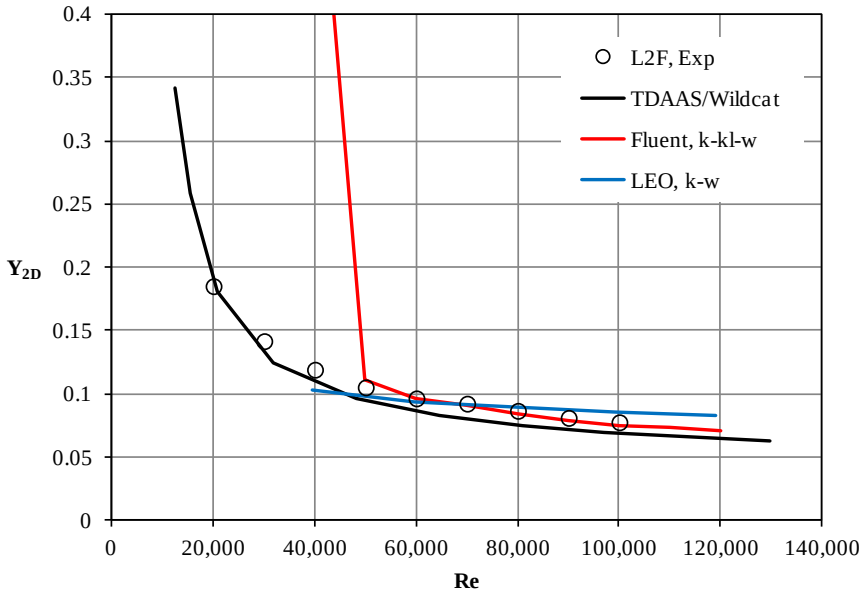

Fig. 5.3 Comparison of L2F Reynolds lapse between experiment and the Wildcat, Fluent and LEO codes

Reynolds lapse predictions for the L2A profile using LEO are shown in Fig. 5.4 and compared with experiment, Fluent and Wildcat. Unlike L2F, the experimental results indicate that L2A stalls for Re < 40,000 with a stronger dependency of Y_{2D} on Re for Re > 40,000. LEO, however, predicts a weak dependency of Y_{2D} on Re, similar to L2F in Fig. 5.3. Fluent again appears to be more accurate for higher Re values, yet it predicts stall to occur at nearly twice the experimental stall Re value. The Wildcat code predicts stall reasonably well for L2A, but under-predicts the slope of the lapse curve prior to stall as Re decreases.

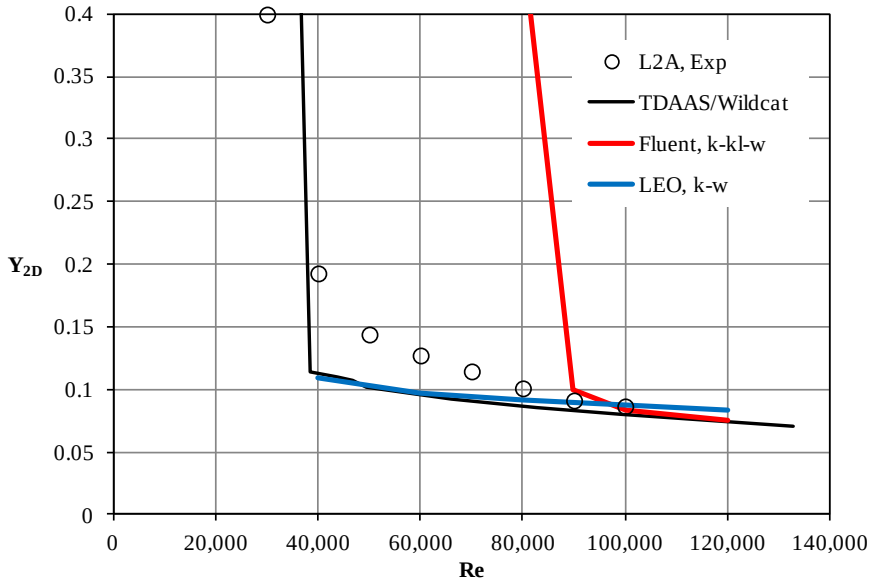

Fig. 5.4 Comparison of L2A Reynolds lapse between experiment and the Wildcat, Fluent, and LEO codes

As shown in Figs. 5.3 and 5.4, all the CFD codes considered reasonably agree with experiments at high Re. Calculations at low Re, however, are quite challenging, primarily due to complex flow physics on the suction surface of high lift LPT profiles. As will be shown using oil flow experiments in Chapter 7, closed separation bubbles are present for L2A and L2F at Re = 100,000. As Re decreases, the increase in Y_{2D} is strongly dependent on the length of the suction surface separation bubble. Stall occurs when the separation bubble fails to reattach upstream of the trailing edge. The Praisner and Clark (2007) separated flow transition model that is employed in Wildcat directly models the growth of the suction surface separation bubble. Their model is correlation based, being derived from turbomachinery cascade flows including both compressor and turbine profiles. Consequently the Wildcat code predicts stall quite well. Walters and Leylek (2005) calibrated their k-k_l-ω model using DNS of channel flow and flat plate boundary layer experiments. High streamline curvature and strain rates in the freestream,

typical of high lift LPT flows were not directly included during calibration, thus providing a possible explanation of why Fluent predicted stall prematurely. The Fluent predictions, however, were quite accurate at high Re. Although the fully turbulent LEO predictions neglected transition effects in the boundary layers, the profile results are in reasonable agreement at high Re with experiments and the other codes that have transition models. At low Re, modeling the boundary layers as fully turbulent in LEO eliminates the separation bubbles, reducing the dependency of Y_{2D} on Re. At high Re with thin separation bubbles, the error due to modeling the boundary layers as fully turbulent is less significant.

Figure 5.5 shows the experimental endwall loss of the L2F and L2A profiles at Re = 100,000 compared with LEO and several loss correlations from the literature. I calculated the endwall loss from the experimental data as the difference between the passage loss and profile loss ($Y_{ps} - Y_{2D}$), the conventional loss breakdown found in the literature. The influence of the inlet boundary layer is not considered in Fig. 5.5 due to the thin boundary layer in the experiment. Using the Sharma and Butler (1987) method for estimating the inlet boundary layer loss, only about 2% of the total loss is due to the inlet boundary layer. As for prediction quality, the LEO predictions arguably agree best with the experiments. Both the Kacker and Okapuu (1982) and Sharma and Butler (1987) correlations significantly over-predict the endwall loss of both profiles. The Benner et al. (2006b) correlation, however, under-predicts the loss. The overall spread of the predictions highlights the difficulty of reliably predicting endwall loss.

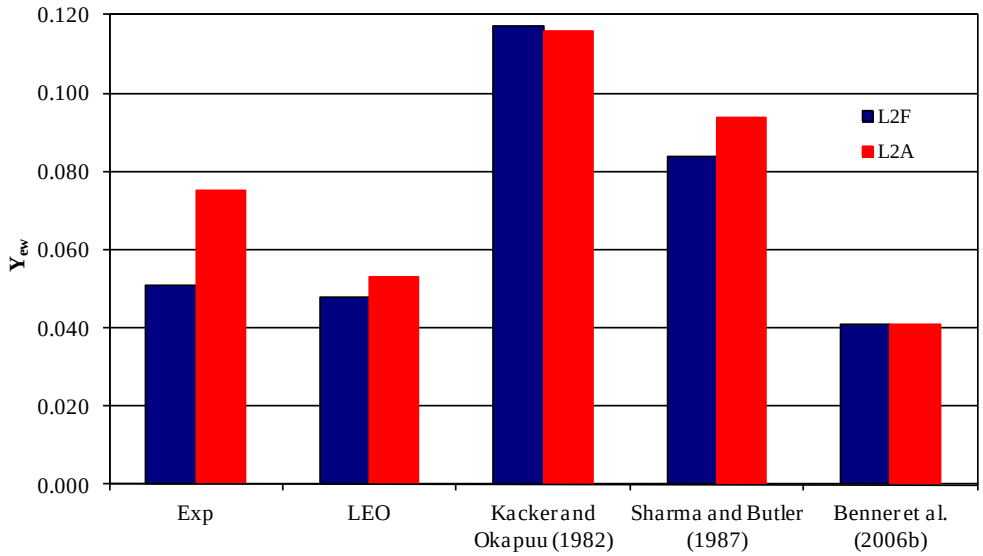

Fig. 5.5 Comparison of experimental endwall loss, Y_{ew}, between LEO and loss correlations (Formulas for the loss correlations are given in Appendix B)

Some additional comments are required regarding the comparison between the experimental data in Fig. 5.5 and the correlation of Benner et al. (2006b). As mentioned above, Y_{ew} based on the experimental data is calculated as the difference between Y_{ps} and Y_{2D}. Benner et al. (2006b), however, defines the loss breakdown as,

$$Y_{ps} = Y_{2D}\left(1 - \frac{Z_{TE}}{H}\right) + Y_{ew}, \tag{5.1}$$

where Z_{TE} is the penetration height of the endwall flow along the span of the suction surface and H is the blade span. Benner et al. (2006a) provide a correlation for Z_{TE}/H. For both L2A and L2F, the penetration height is $Z_{TE}/H \approx 0.15$. Analyzing the experimental data using the loss breakdown of Eq. (5.1) suggests that Y_{ew} for the experiment will be between 15% and 20% larger than what is shown in Fig. 5.5. Therefore, correcting the experimental data according to the loss breakdown of Benner et

al. (2006b) actually increases the discrepancy between the experiments and their correlation.

As for the difference between the L2F and L2A profiles in Fig. 5.5, the experiments indicate that Y_{ew} for L2A is +47% different than L2F. As will be shown in Chapter 7, surface flow visualization indicates that there is more separated flow near the endwall for L2A than L2F, thus causing the increased endwall loss for L2A. The LEO predictions also indicate higher endwall loss for L2A, but only +10.4% different than L2F. The fully turbulent computations cannot reliably model separation effects, so the LEO prediction for L2A is significantly low. It is suggested that the difference in Y_{ew} between L2F and L2A predicted using LEO is more representative of endwall loss at high Re where separation effects are less significant for both profiles. Both the Kacker and Okapuu (1982) and Benner et al. (2006b) correlations predict negligible differences between L2A and L2F, primarily because both profiles have similar flow angles and equal stagger settings. These two correlations do not consider effects that might suggest the presence of flow separation, such as Re. The Sharma and Butler (1987) correlation, however, agrees qualitatively with the experiments and LEO in that Y_{ew} for L2A is +11.9% different than L2F. Their model suggests that Y_{ew} is proportional to the profile loss, Y_{2D}. In the experiment, Y_{2D} for L2A is +10.8% different than for L2F.

It is worth noting that the Kacker and Okapuu (1982) correlation was originally developed for rotating rigs. In fact, Benner et al. (2006b) suggested a scale factor of 0.23 to adjust the Kacker and Okapuu (1982) predictions for use with linear cascade data. Applying this correction results in Y_{ew} = 0.027 in Fig. 5.5, so agreement with the experiment is still poor. Both the Sharma and Butler (1987) and Benner et al. (2006b)

correlations were developed for linear cascades. These two correlations, however, differ by a factor of two. Despite their shortcomings, RANS based predictions using codes such as LEO appear to be preferable over empirical methods for evaluating endwall loss.

To demonstrate how LEO predicts the endwall flow patterns, Fig. 5.6 shows a comparison between experiment and CFD of total pressure loss coefficients, secondary velocity vectors, and secondary vorticity for the L2F profile. The data are from the measurement plane of Fig. 4.2. The secondary vorticity coefficients, $C\omega_s$, were computed using the method described by Hodson and Dominy (1987),

$$C\omega_s = \frac{\partial W}{\partial y} - \frac{\partial V_s}{\partial z}, \tag{5.2}$$

where the variables were non-dimensionalized according to Table 6.2. The positive axis of vorticity is out of the page. Equation (5.2) will not equal the magnitude of the vorticity vector in the streamwise direction, x_s, but provides a measure of the relative strength of the streamwise vorticity across the measurement area. The measurements of Fig. 5.6a show a strong negative vorticity core associated with the clockwise passage vortex flow, centered approximately at y/S = 0.45 and z/H = 0.07. LEO, however, does not predict a well defined negative vorticity core associated with the passage vortex, but rather a diffuse region of negative vorticity. The positive shed vorticity due to endwall flow interaction with the profile is also more localized in the experiment (y/S = 0.4 and z/H = 0.12), whereas LEO predicts the shed vorticity region to be elongated in the spanwise direction. Overall, the shapes of the wakes as indicated by the Y contours are similar but with some notable differences. LEO predicts endwall effects to propagate to nearly z/H = 0.30, whereas they only propagate to approximately z/H = 0.25 in the

experiment. Furthermore, LEO predicts a narrower wake than the experiment, including higher loss peaks.

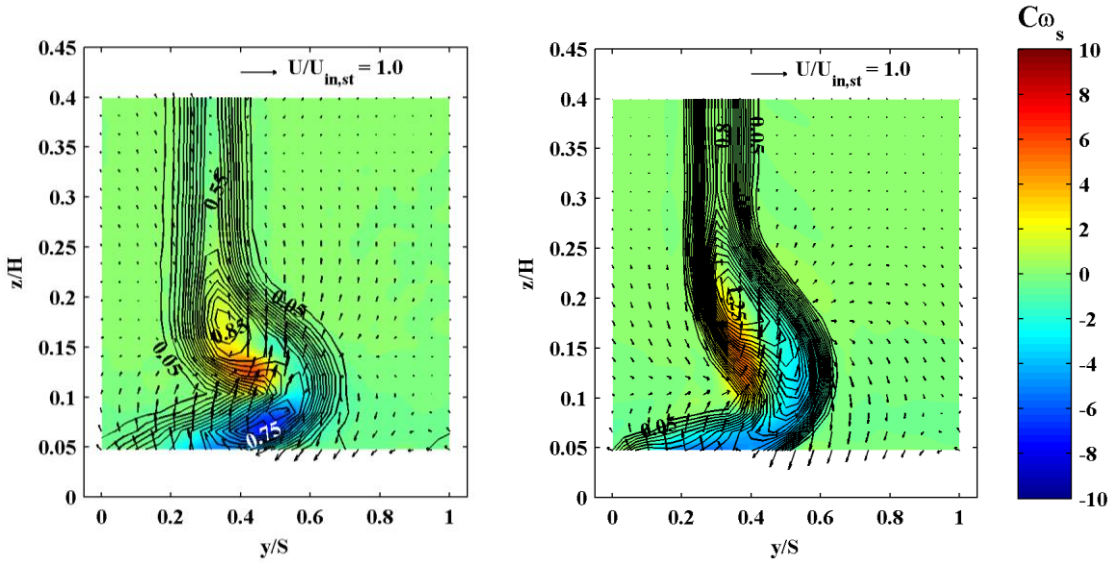

a) Experiment b) LEO

Fig. 5.6 Comparison between experiment and LEO of L2F secondary velocity vectors, secondary vorticity and total pressure loss coefficient contours (ΔY = 0.05)

In summary, the purpose of the CFD predictions using the LEO code is to compare the research profiles and determine significant geometry effects that influence endwall loss. For benchmarking, the LEO Y_{2D} predictions were compared with experiments and the Fluent and Wildcat codes for the L2F and L2A profiles. Overall, LEO predicts Y_{2D} reasonably well at high Re. At low Re, LEO performs poorly for predicting Y_{2D}, primarily because the fully turbulent predictions eliminate separation bubbles on the suction surface. The result is that LEO under-predicts the slope of the Reynolds lapse curve.

Predictions of Y_{ew} using LEO for the L2F and L2A profiles were compared with experiments and three loss correlations from the literature. Results using LEO were

significantly more accurate than the loss correlations and predicted the qualitative differences in Y_{ew} between the L2F and L2A profiles (see Fig. 5.5). Although the LEO Y_{ew} prediction for the L2F profile was within 6% of the experiment, LEO under-predicted Y_{ew} for L2A by 29%, primarily due to a failure to capture endwall flow separation effects. Differences in pressure loss computed using LEO should therefore be regarded as the way the profiles operate at high Re where separation effects are not as significant. Although the LEO code may not reliably capture low Re effects, it is expected to indicate differences in Y_{ew} due to profile geometry.

6. Fluid Mechanics of Endwall Loss Production

The purpose of this chapter is to explain the cause of total pressure loss of endwall flows, providing a basis for interpreting the results of the following chapters that focus on pressure loading and stagger angle effects. The discussion begins with an analysis of loss production, followed by experimental results that decouple the mixing effects in the endwall wake. It will be shown that mean flow shear is negligible in comparison to turbulent shear, indicating that turbulence dissipation is the dominant cause of total pressure loss. Using an experiment with boundary layer fences, it will be shown that rather than contributing to the mixing loss, the mean endwall flow field has a role in causing excessive wake growth and possibly flow separation.

6.1 Total Pressure Loss of Adiabatic and Incompressible Turbulent Flows

For incompressible and adiabatic cascade flows the overall work is zero. For these conditions the first law of thermodynamics can be written as,

$$\frac{\Delta P_t}{\rho} = -\Delta e, \tag{6.1}$$

where e is internal energy. We see that the passage total pressure loss will be due to an increase in internal energy. At a single point in the flow, the equation for internal energy can be written as (cf., Panton, 1996),

$$\frac{De}{Dt} = 2\upsilon S_{ij} \frac{\partial v_i}{\partial x_j}, \tag{6.2}$$

where S_{ij} is the strain rate tensor and v_i is the instantaneous velocity. The velocity gradient tensor of Eq. (6.2) can be rewritten as the sum of symmetric and anti-symmetric

parts. The product of the symmetric strain rate tensor and the anti-symmetric part of the velocity gradient tensor will be zero, so Eq. (6.2) can be rewritten as,

$$\frac{De}{Dt} = 2\upsilon S_{ij}S_{ij}. \tag{6.3}$$

S_{ij} can be represented as the sum of mean and fluctuating components (cf., Pope, 2000),

$$S_{ij} = \langle S_{ij} \rangle + s_{ij}, \tag{6.4}$$

where $\langle S_{ij} \rangle$ is the mean strain rate tensor and s_{ij} is the fluctuation strain rate tensor. Substituting Eq. (6.4) into Eq. (6.3) and Reynolds averaging,

$$\frac{D\langle e \rangle}{Dt} = 2\upsilon\left[\langle S_{ij} \rangle\langle S_{ij} \rangle + \langle s_{ij}s_{ij} \rangle\right], \tag{6.5}$$

where $\langle e \rangle$ is the mean internal energy. The quantities $2\upsilon\langle S_{ij} \rangle\langle S_{ij} \rangle$ and $2\upsilon\langle s_{ij}s_{ij} \rangle$ are the mean flow and turbulence dissipation rates, respectively. These dissipation terms are caused by shear stresses in the fluid. To decouple the roles of the mean and turbulent flow fields in loss production, one could locally measure both dissipation rates to obtain a direct measure of internal energy production and total pressure loss. Integrating the local dissipation measurements across the passage would yield the overall total pressure loss production rate. Unfortunately, measurement of the turbulence dissipation rate is very difficult even for simple flows due to the need to measure instantaneous fluctuation gradients. The terms derived in the following section that influence mechanical energy and total pressure are more easily measured.

6.2 Analytical Decomposition of Mixing Effects

An alternative method to quantify local influences on total pressure can be derived from the RANS momentum equation,

$$\frac{\partial U_i}{\partial t} + U_j \frac{\partial U_i}{\partial x_j} = -\frac{1}{\rho}\frac{\partial P_s}{\partial x_i} + \upsilon \frac{\partial^2 U_i}{\partial x_j \partial x_j} - \frac{\partial \langle u_i u_j \rangle}{\partial x_j}. \tag{6.6}$$

The convection term on the left hand side can be replaced using the following identity given by Panton (1996),

$$U_j \frac{\partial U_i}{\partial x_j} = \frac{\partial}{\partial x_i}\left(\frac{1}{2} U_j U_j\right) + \varepsilon_{ijk}\omega_j U_k, \tag{6.7}$$

where ω_j is the local vorticity vector. Note that the second term on the right hand side of Eq. (6.7) can also be written as $\vec{\omega} \times \vec{U}$. Assuming steady mean flow and substituting Eq. (6.7) into Eq. (6.6), we obtain an expression for the spatial total pressure derivatives,

$$\frac{\partial P_t}{\partial x_i} = \mu \frac{\partial^2 U_i}{\partial x_j \partial x_j} - \rho \varepsilon_{ijk}\omega_j U_k - \rho \frac{\partial \langle u_i u_j \rangle}{\partial x_j}. \tag{6.8}$$

Equation (6.8) can be interpreted as a local description of the force balance in the flow field that causes changes in total pressure. The first term on the right hand side represents a force due to viscous diffusion, an irreversible mean flow friction force (IMF). The second term came from the vector identity of Eq. (6.7) and represents a coriolis force. This vector identity decomposed the convection term present in the inviscid Euler equations and as a result, is a reversible mean force (RMF). The last term of Eq. (6.8) requires more attention. Following Pope (2000), the Reynolds stress tensor can be decomposed as,

$$\langle u_i u_j \rangle = \frac{2}{3} k \delta_{ij} + a_{ij}, \tag{6.9}$$

where $k = 0.5\langle u_i u_i \rangle$ is the turbulent kinetic energy. This decomposition splits the Reynolds stress tensor into isotropic and anisotropic parts, $\frac{2}{3}k\delta_{ij}$ and a_{ij}, respectively. The term a_{ij} is referred to as the anisotropy tensor. The isotropic stress cannot cause shear and as a result, represents a reversible turbulent force (RTF). This is analogous to the absence of pressure from the vorticity equation because of its inability to cause shear. On the other hand, a_{ij} represents a shear stress and as a result, accounts for an irreversible turbulent force (ITF). In summary, we have irreversible mean forces (IMF), irreversible turbulent forces (ITF), reversible mean forces (RMF), and reversible turbulent forces (RTF) that define the total pressure spatial derivatives.

For experiments, it is convenient to non-dimensionalize equations for establishing similarity and to enable scaling. In this study, spatial variables were scaled using the axial chord. Total pressure was scaled by twice the inlet dynamic head. Velocities were scaled by the inlet mean velocity magnitude and turbulence quantities by the square of the inlet mean velocity magnitude. In non-dimensional variables, Eq. (6.8) can be expressed as,

$$\frac{\partial P_t}{\partial x_i} = \frac{1}{Re}\frac{\partial^2 U_i}{\partial x_j \partial x_j} - \varepsilon_{ijk}\omega_j U_k - \left(\frac{2}{3}\frac{\partial k}{\partial x_j}\delta_{ij} + \frac{\partial a_{ij}}{\partial x_j}\right). \tag{6.10}$$

For convenience, the index notation terms of Eq. (6.10) are written out explicitly in Table 6.1 with non-dimensional variables for the x-direction. The forms of the total pressure derivatives in the y and z directions are implied. To expand the index notation terms, substituting 1, 2, or 3 for the indices (i.e., i, j, and k) refers to the x, y, and z coordinate directions, respectively. Table 6.2 lists the scales used for non-dimensionalization.

Table 6.1 Expansion of Eq. (6.10) for the x-direction

$\frac{\partial P_t}{\partial x} = IMF_x + RMF_x + RTF_x + ITF_x$	
IMF_x	$\frac{1}{Re}\left(\frac{\partial^2 U}{\partial x^2} + \frac{\partial^2 U}{\partial y^2} + \frac{\partial^2 U}{\partial z^2}\right)$
RMFx	$(-1)(\omega_y W - \omega_z V)$
RTF_x	$\left(-\frac{2}{3}\right)\frac{\partial k}{\partial x}$
ITF_x	$(-1)\left(\frac{\partial a_{uu}}{\partial x} + \frac{\partial a_{uv}}{\partial y} + \frac{\partial a_{uw}}{\partial z}\right)$

Table 6.2 Summary of Scaling Variables

Quantity	Scale
P_t	$\rho U_{in,st}^2$
Velocity	$U_{in,st}$
Fluctuation or Re Stress	$U_{in,st}^2$
Distance	C_{ax}

Because Eq. (6.10) is an alternative form of the RANS momentum equation (a vector equation), taking the dot product of Eq. (6.10) with the mean velocity vector will result in a mechanical energy equation. The forces will generate work in the flow. By taking the dot product of Eq. (6.10) with a unit vector in the mean flow direction, we obtain a measure of the change in total pressure along the local streamline,

$$\partial_s P_t = \nabla P_t \cdot \vec{n}\,, \tag{6.11}$$

where,

$$\nabla P_t = \frac{\partial P_t}{\partial x}\vec{i} + \frac{\partial P_t}{\partial y}\vec{j} + \frac{\partial P_t}{\partial z}\vec{k}\,, \tag{6.12}$$

and $\vec{n}$ is the unit vector in the mean flow direction. Recognizing that for dimensional variables $\partial_s P_t \left\| \vec{U} \right\|$ has units of energy per unit volume, decomposing the terms that comprise $\partial_s P_t$ indicate the effects that change the mechanical energy of the flow during mixing. Thus, $\partial_s P_t$ is our focus for studying the mixing effects. Upon carrying out the calculation of $\partial_s P_t$ by hand, one finds that the second term on the right hand side of Eq. (6.10) (i.e., term defining RMF) is orthogonal to the mean velocity vector. Thus, RMF has no role in changing the mechanical energy of the flow. The remaining mixing effects are decoupled according to,

$$IMF = IMF_x n_x + IMF_y n_y + IMF_z n_z, \tag{6.13}$$

$$RTF = RTF_x n_x + RTF_y n_y + RTF_z n_z, \tag{6.14}$$

$$ITF = ITF_x n_x + ITF_y n_y + ITF_z n_z, \tag{6.15}$$

and,

$$\partial_s P_t = IMF + RTF + ITF. \tag{6.16}$$

Depending on the application, one may choose to obtain the spatial total pressure gradient in a specific direction rather than a full calculation of $\partial_s P_t$. For example, the total pressure gradient in the cascade axial (x-direction) may be needed. For that case, $\partial P_t / \partial x$ of Table 6.1 can be directly applied. Note that the RMF_x term in Table 6.1 cannot be neglected for that case because the total pressure gradient will not be in the streamline direction. Later in Section 6.4, measurements of $\partial_s P_t$ along with subcomponents (i.e., IMF, RTF, and ITF) are presented to study mixing within the endwall wake. The

following section shows flow and loss measurements within the endwall wake to provide a basis for discussing the mixing effects.

6.3 Flow Field Description of the L2A and L2F Profiles

For convenience, the schematic in Chapter 4 depicting the cascade and secondary flow coordinate systems is shown in Fig. 6.1. As shown, the measurement plane is $0.58C_{ax}$ downstream of the blade row. The wake from the cascade center airfoil passes through the approximate center of the measurement plane.

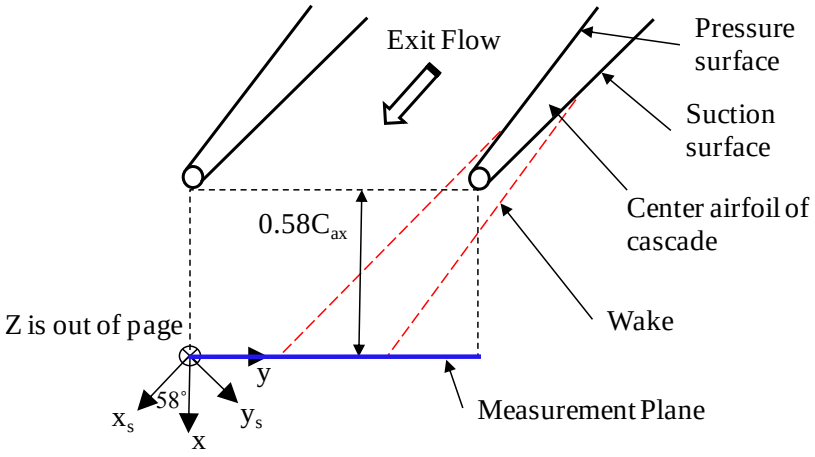

Fig. 6.1 Schematic depicting the cascade and secondary flow (subscript s) coordinate system definitions

Figure 6.2 gives surveys of secondary velocity vectors (V_s, W), secondary vorticity coefficients ($C\omega_s$, See Eq. (5.2)) and total pressure loss coefficients (Y) for the L2A and L2F profiles. The wake behind the center blade of the cascade is shown where the right side of the wake corresponds to the suction surface (see Fig. 6.1). For L2A, the center of the passage vortex is approximately at y/S = 0.48 and z/H = 0.07, as indicated by the secondary velocity vectors in Fig. 6.2a. The passage vortex extends approximately to z/H = 0.10. The clockwise sense of the passage vortex generates strong negative

vorticity. The secondary velocity vectors midwake beyond the passage vortex show a spanwise migration of flow towards midspan. Those vectors indicate that this migrating flow extends to approximately z/H = 0.20. The boundary layer on the suction surface will be skewed due to this migrating flow. Furthermore, the spanwise migration of flow turns away from the suction surface and separates, generating a weaker negative vorticity core at y/S = 0.55 and z/H = 0.16. Also note in Fig. 6.2a that there is a region of positive vorticity that has a peak magnitude at y/S = 0.45 and z/H = 0.12 and extends to nearly z/H = 0.20. This region of positive vorticity (commonly referred to as the shed vorticity) is due to the skewing of the profile boundary layer by the spanwise flow migration.

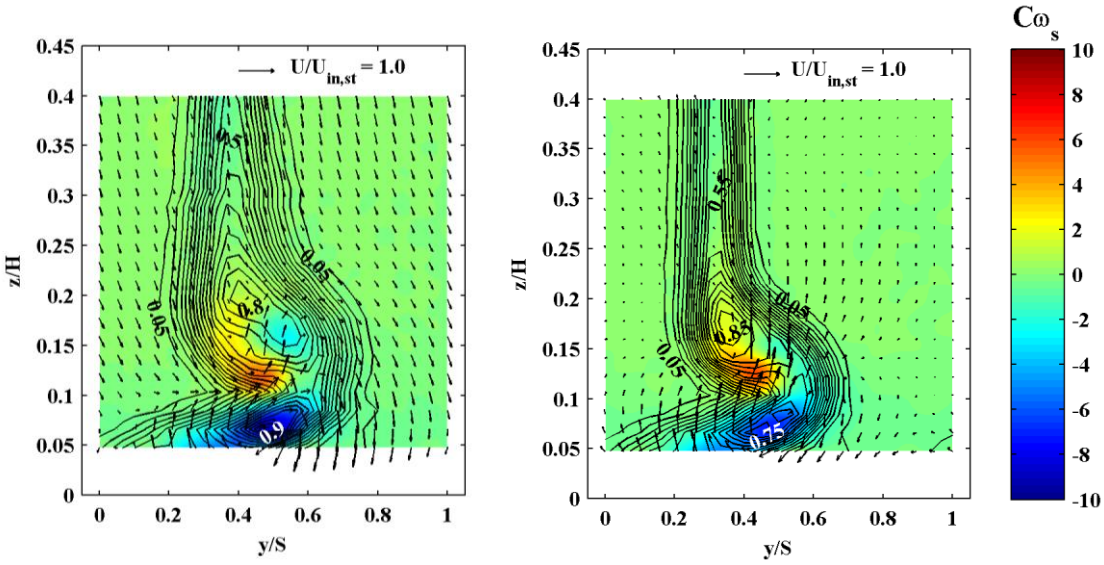

a) L2A b) L2F

Fig. 6.2 Secondary vorticity, total pressure loss coefficients (ΔY = 0.05 for contours), and secondary velocity vectors within the measurement plane of Fig. 6.1 at Re = 100k

The Y contours of Fig. 6.2a for L2A show that there are two regions of low energy cores in the flow field, which is typical of endwall flows. The low energy core closest to the endwall is approximately collocated with the passage vortex, at y/S = 0.48

and z/H = 0.07. A larger low energy region is approximately centered at y/S = 0.45 and z/H = 0.18.

Also note for L2A that there is a z component of the secondary velocity vectors approaching midspan, a region in the measurement area where the z component may be expected to be nearly zero. This z component is due to the extra blockage of the wind tunnel boundary layer at z/H = 1.0, compared to the relatively thin boundary layer on the tunnel splitter plate at z/H = 0 (See Fig. 4.1). Using the splitter plate, the z component of velocity approaching midspan is smaller for cascades that have less secondary loss, such as L2F in Fig. 6.2b.

The L2F Y contours in Fig. 6.2b indicate a much smaller wake than L2A. The peak negative vorticity associated with the passage vortex is centered approximately at y/S = 0.45 and z/H = 0.07. Unlike L2A, the L2F endwall flow does not produce a second, weaker negative vorticity core, but a single region of negative vorticity associated with the clockwise sense of the endwall flow. The L2F velocity vectors midwake beyond the passage vortex do not indicate flow turning away from the profile as shown for L2A, and may be why the second, weaker negative vorticity core does not form for L2F. The L2F positive shed vorticity is similar to L2A.

Also similar to L2A, the L2F Y contours show two regions of low energy cores. The low energy core closest to the endwall is approximately collocated with the passage vortex, at y/S = 0.45 and z/H = 0.07. The larger low energy region has the peak loss approximately centered at y/S = 0.38 and z/H = 0.17.

Having shown that the L2A and L2F total pressure and flow fields are significantly different, this pair of airfoils provides a good set of test cases for studying

freestream loss generation and mixing. In the following section I discuss the mixing force decomposition for both profiles to explain the roles of the mean flow and turbulence fields in mixing loss production.

6.4 Experimental Determination of Mixing Effects

Figure 6.3 shows the mixing force decomposition taken inside the large low energy cores of both profiles of Fig. 6.2. Figure 6.3a shows $\partial_s P_t$ obtained at 20% span of the L2A wake. In relation to mixing, negative $\partial_s P_t$ on the outside of the wake indicates energy extraction from the mean flow, whereas positive $\partial_s P_t$ within the middle of the wake indicates energy addition. Recall from Eq. (6.16) that IMF, ITF, and RTF sum together to give $\partial_s P_t$. One first notes in Fig. 6.3a that the irreversible mean force due to viscous diffusion, IMF, is negligibly small. Secondly, the dominant mixing effect is the irreversible turbulent shear force, ITF. The reversible turbulent force, RTF, plays a secondary role in mixing at this spanwise location for L2A. Figure 6.3b shows $\partial_s P_t$, IMF, ITF, and RTF obtained at 17.7% span of the L2F wake. Similar to L2A, IMF is negligible across the wake while ITF is the dominant mixing force. RTF has a secondary role in mixing for L2F. Considering the dominant shear force, ITF, the magnitudes are similar across the wakes of both profiles.

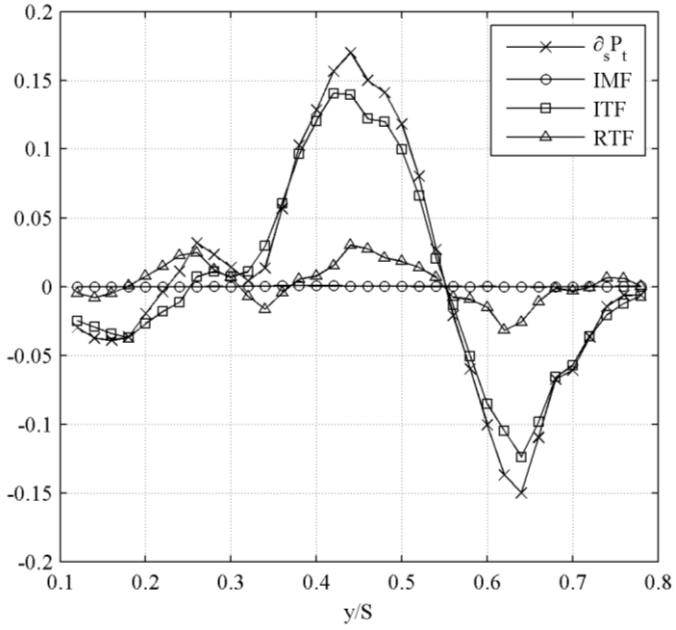

a) L2A, 20% span

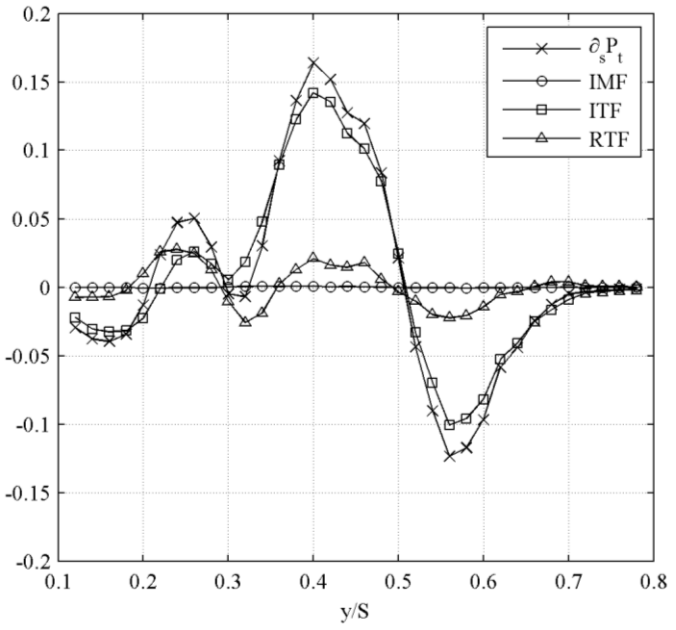

b) L2F, 17.7% span

Fig. 6.3 Decomposition of mixing forces within the dominant endwall loss cores of the L2A and L2F profiles

Figure 6.3 provides insight into how mixing loss is produced in the wakes. In Section 6.1 it was shown that the rate of loss production is due to the sum of the mean

flow and turbulence dissipation rates, both resulting from shear effects that change the internal energy of the flow. In Fig. 6.3, the mixing forces cause changes in the mechanical energy of the flow. Two of the mixing forces, IMF and ITF, are due to shear and therefore indicate the presence of irreversible effects that generate total pressure loss. Since the turbulent shear mixing force in Fig. 6.3, ITF, is dominant over the mean flow shear mixing force, IMF, it is suggested that turbulence dissipation is the primary cause of mixing loss. Furthermore, since the data were captured within the endwall wakes at spanwise locations containing peak loss cores where mixing is expected to be strong, the conclusion of negligible mean flow shear is expected to be independent of span.

Some additional terms are defined for convenience to verify the assumption that the mean flow shear remains negligible across the whole measurement area. Consider mixing in the downstream main flow direction, x_s of Fig. 6.1. By inspection of Table 6.1 and applying the secondary coordinate system, IMF_{xs} will define the mean flow shear force in the main flow direction. IMF_{xs} results from viscous diffusion, or second derivatives of the U_s velocity. A new mean flow shear force parameter is defined as,

$$F_M = \frac{1}{Re}\left(\frac{\partial^2 U_s}{\partial y^2} + \frac{\partial^2 U_s}{\partial z^2} \right), \tag{6.17}$$

with non-dimensional variables according to Table 6.2. The diffusion term in the x_s direction was neglected. Also note in Eq. (6.17) the second derivative in the y direction as opposed to y_s. This change reflects the measurement plane orientation in the y direction. F_M will therefore have a smaller magnitude than expected for IMF_{xs}.

Using similar reasoning as for defining F_M, I define a new turbulent shear force parameter. Recognizing in Eq. (6.9) that $\langle u_i u_j \rangle = a_{ij}$ when $i \neq j$, this parameter is defined by,

$$F_T = -\left(\frac{\partial \langle uv \rangle_s}{\partial y} + \frac{\partial \langle uw \rangle_s}{\partial z} \right), \tag{6.18}$$

with non-dimensional variables according to Table 6.2. F_T will have a smaller magnitude than ITF_{xs} due to the derivative in the y direction as opposed to y_s. The implication of Eqs. (6.17-6.18) is that if F_M/F_T is negligible, then IMF_{xs}/ITF_{xs} will also be negligible. For calculating F_M and F_T over the full area traverse, the velocity and turbulence data were refined using cubic spline interpolation for computing derivatives.

Figure 6.4 shows area plots of F_M and F_T for both profiles as indicated by the color scale. Lines of constant Y (labeled in Figs. 6.4b and 6.4d for visibility) and secondary velocity vectors are shown to visualize the wake. Figures 6.4a and 6.4c compare F_T for L2A and L2F, respectively. As shown for both profiles, F_T is negative on the outside of the wakes as expected, indicating energy extraction from the mean flow. In the middle of the wakes, F_T is positive, indicating energy addition. Figures 6.4b and 6.4d show that F_M is nearly zero over the whole measurement area for both profiles resulting in negligible color variation, indicating that F_M remains negligible compared to F_T. Thus, it appears that turbulent shear almost entirely drives the mixing process. The dominant role of turbulent shear in mixing also suggests that turbulence dissipation is the primary source of loss production across the whole wake.

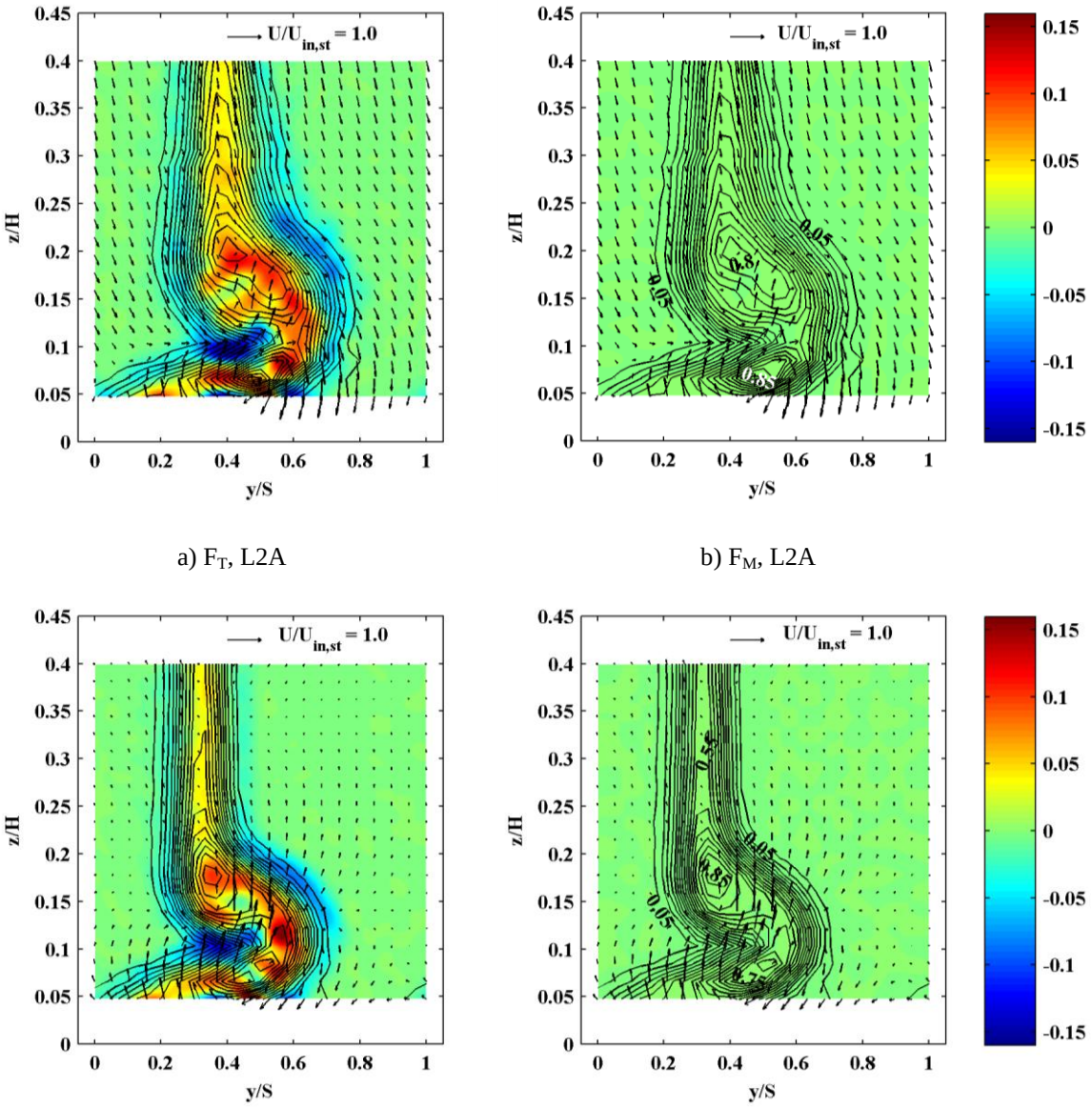

a) F_T, L2A

b) F_M, L2A

c) F_T, L2F

d) F_M, L2F

Fig. 6.4 Flood plots of mixing force variables for the L2A and L2F profiles overlaid with Y contours and secondary velocity vectors (ΔY = 0.05 for contour lines)

A more quantitative comparison between F_T and F_M can be made by calculating pitchwise averages of the absolute values of the mixing forces along the span. Absolute values are recommended for convenience because the mixing forces are both positive and negative across the wake. Averaging the shear strength without taking absolute values falsely suggests that the shear is weak due to positive and negative shear forces nearly

canceling out. Figure 6.5 shows pitchwise averages of the ratio of the absolute value of the turbulent shear strength, $|F_T|$, to the total shear strength, $|F_T| + |F_M|$. For both profiles, turbulent shear accounts for over 98.5% of the total shear strength for all spanwise positions considered. Approaching midspan for both profiles, mean flow shear has slightly more influence due to the wake becoming narrower. Similarly, mean flow shear has more influence approaching midspan for L2F than L2A because the L2F wake is narrower than the L2A wake. Nevertheless, mean flow shear is essentially negligible compared to turbulent shear for all spanwise positions considered.

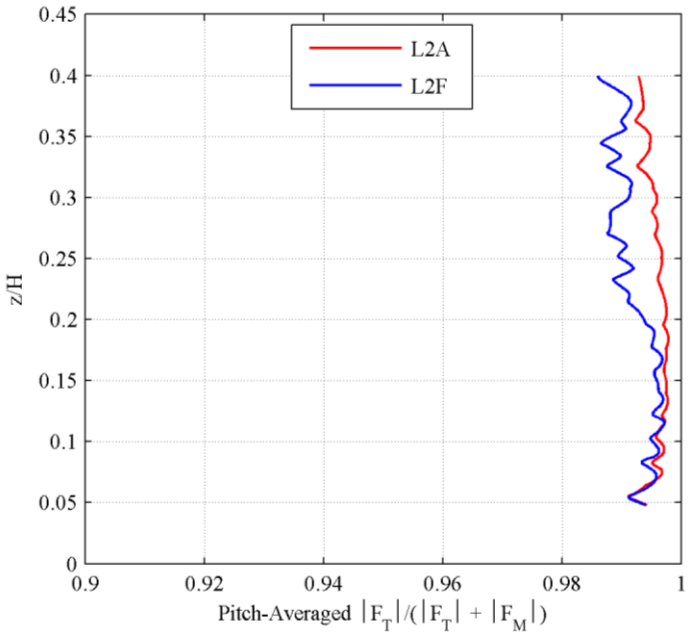

Fig. 6.5 Pitch-averaged variation of the contribution of turbulent shear to the total shear strength

As an additional check of the comparison between mean flow and turbulent shear, I recalculated F_M using both V_s and W. The reason for using V_s and W for checking F_M is because those velocities are used for calculating secondary vorticity coefficients.

Although not shown, the change in the results of Fig. 6.5 was negligible, further supporting the conclusion that mean flow shear is negligible compared to turbulent shear.

Although the mean flow field does not significantly contribute to the mixing loss, it is suggested that it has a role in causing flow separation. An ad hoc experiment using boundary layer fences on the L2A profile is used in the following section to elucidate the role of the mean endwall flow field in loss production. The fences are used to reduce the spanwise extent that the endwall flow can interact with the suction surface. Using the fences, it will be shown that more of the passage flow is 2D, with the wake becoming large primarily in the presence of the endwall flow. Hence, the likely role of the mean endwall flow field in loss production is to cause excessive wake growth or perhaps separation.

6.5 Effect of a Boundary Layer Fence on Suction Surface Separation

The concept of how a profile boundary layer fence operates is shown in Fig. 6.6. Due to overturning inside the passage within the endwall boundary layer, flow is driven across the passage from the pressure to suction side, impinging on the suction surface. Without fences, this cross-passage flow is also driven up the profile along the span, as indicated by the basic endwall flow model of Fig. 2.1. As shown in Fig. 6.6, the fence is used to intentionally turn the cross-passage flow at a spanwise position close to the endwall. Due to a weak spanwise pressure gradient that can potentially cause flow to jump the fence, a relatively short fence can effectively turn the cross-passage flow. The fence limits the spanwise extent of the endwall flow.

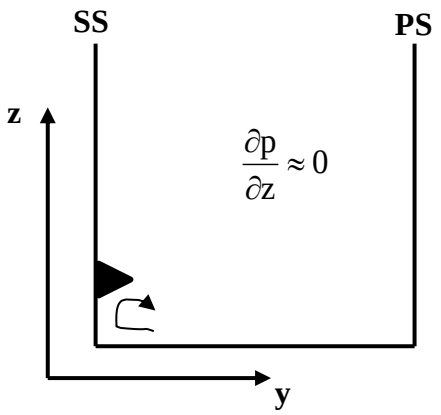

Fig. 6.6 Sketch demonstrating the effect of a suction surface boundary layer fence on the boundary layer flow

Figure 6.7 shows sketches of boundary layer fences installed on the three center airfoils of the L2A cascade. The fences were nominally installed at 3.6% span, a distance above the inlet boundary layer thickness. Bloxham's (2010) particle image velocimetry measurements on the L1A profile, which has nearly the same gas angles as L2A in the present study, indicated that the spanwise flow of the passage vortex remains close to the suction surface inside the passage. Using Bloxham's (2010) measurements as a guide, sheet metal fences were cut to extend into the flow 8.5% pitch from the suction surface. Results of suction surface flow visualization experiments, shown later in Fig. 6.9a, indicated that close to the endwall, the overturned cross-passage flow impinges on the suction surface prior to $x/C_{ax} = 0.50$ inside the passage. For that reason, the fences were cut to wrap around the whole suction surface, tapering into the leading and trailing edges.

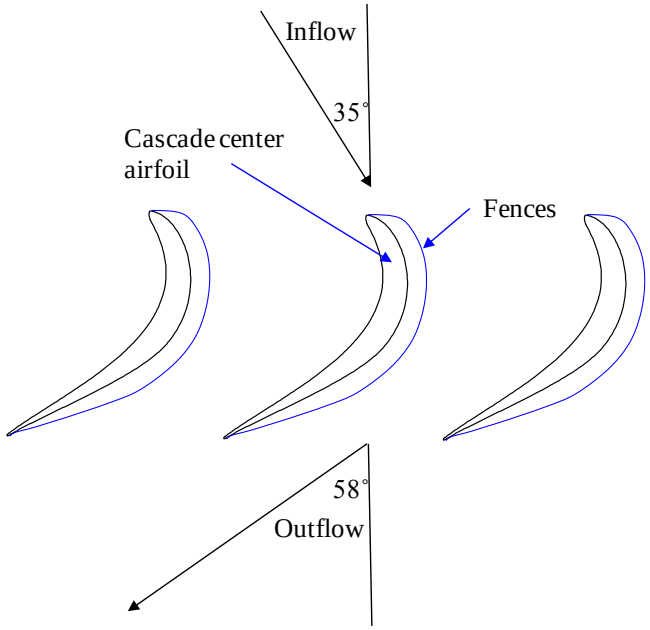

Fig. 6.7 Sketch of three center cascade airfoils with fences attached

The effect of the fence on the cascade center airfoil wake is shown in Fig. 6.8. One first notes in Fig. 6.8b that applying the fence caused a nearly 2D flow from z/H = 0.14 on towards midspan. The region of positive shed vorticity in Fig. 6.8a that has a peak magnitude approximately centered at y/S = 0.45 and z/H = 0.12, is essentially eliminated using the fence. This region of positive vorticity was eliminated because of the absence of spanwise flow along the profile that would normally skew the boundary layer. Furthermore, because of the absence of the spanwise flow, there is no ability for flow separation to propagate towards midspan. The absence of spanwise flow is why the large low energy region of Fig. 6.8a that is approximately centered at y/S = 0.45 and z/H = 0.18 is nearly eliminated using the fence. Without fences, significant endwall effects propagate to approximately 30% span, but to only 14% span with fences. Although fences constrain endwall effects closer to the endwall, the resulting wake occupies a larger fraction of the pitch than without using fences.

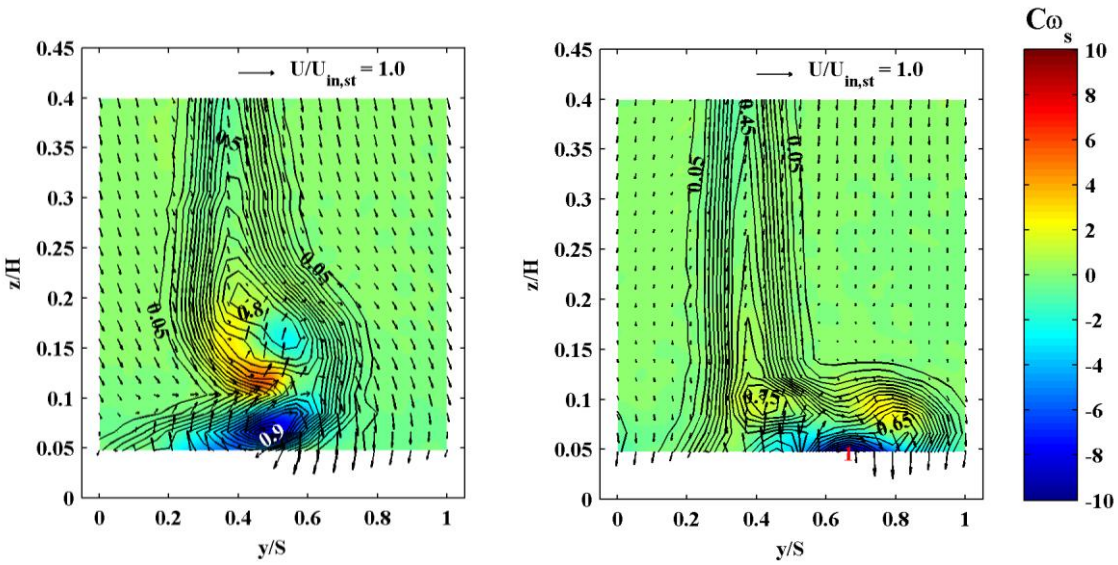

a) L2A, without fences, Re = 100,000 b) L2A, with fences, Re = 100,000

Fig. 6.8 Comparison of L2A secondary vorticity, Y contours and secondary velocity vectors with and without profile boundary layer fences

Surface flow visualizations provide additional insight into the effect of the endwall flow on the suction surface boundary layer. Figure 6.9 shows suction surface flow visualizations of L2A with and without the profile fences. (Appendix G discusses the flow visualization technique.) Without fences, Fig. 6.9a shows several different zones of flow behavior that are identified by the numbers. The blue arrows indicate the approximate flow directions. Zones one, two and three indicate flow upstream, within, and downstream of a closed separation bubble, indicating 2D profile flow behavior. Zones four and five indicate spanwise flow emanating from the endwall. The absence of oil in zone four indicates strong surface shear due to flow impingement from the overturned cross-passage boundary layer flow. No oil flow occurred in zone six, indicating flow separation due to the spanwise endwall flow.

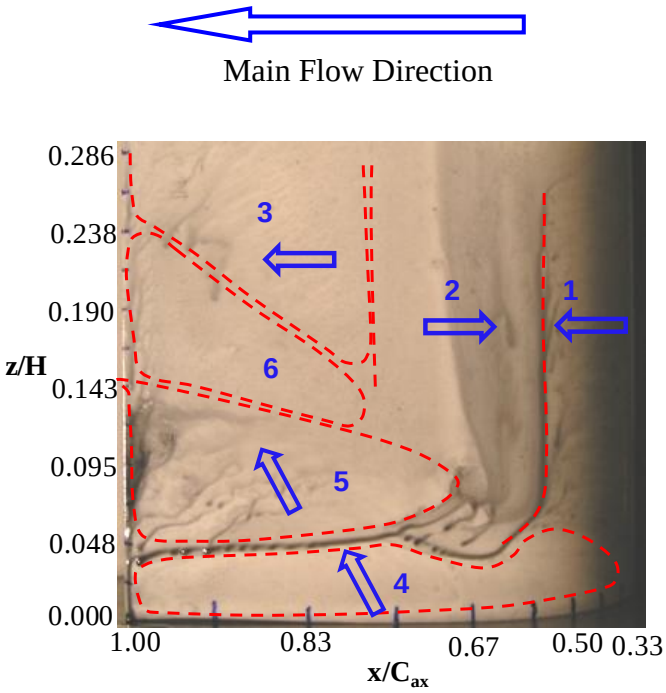

a) L2A, without fences, Re = 100,000

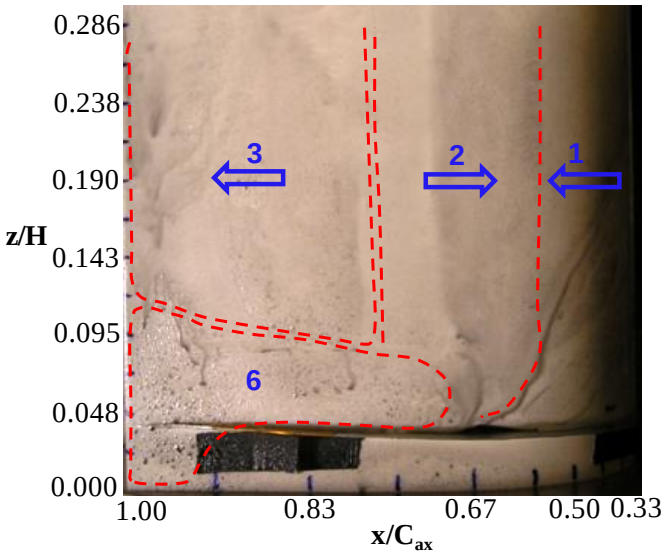

b) L2A, with fences, Re = 100,000

Fig. 6.9 Comparison of L2A suction surface flow visualization with and without profile fences

Similar to without fences, the results with the fence in Fig. 6.9b show well-defined regions of predominantly 2D behavior, zones one, two and three. By limiting the spanwise extent of the endwall flow, the fence allows zone three to extend closer to the endwall than without fences, resulting in the nearly 2D wake down to 14% span in Fig. 6.8b. Between zone three and the endwall using fences, however, the flow separates from the profile. This separated flow region is labeled zone six in Fig. 6.9b. The fence obstructs the spanwise flow, characteristic of zone four and five in Fig. 6.9a, so these two zones are not labeled in Fig. 6.9b with the fence. Instead of remaining close to the suction surface, the adverse pressure gradient in the passage causes the obstructed spanwise flow to separate from the profile. The resulting wake occupies a larger fraction of the pitch than without fences, as shown in Fig. 6.8. Without fences, the low energy cross-passage boundary layer fluid is distributed along a larger spanwise distance to produce a thinner wake in the pitchwise direction.

Common to the L2A results with and without fences is that separation effects on the profile occur in the presence of the endwall flow. As shown in Figs. 6.8 and 6.9, applying the profile fence constrained the endwall flow closer to the endwall. Likewise, the addition of the fence moved the region of separated flow, zone 6, closer to the endwall. These findings suggest that the role of the mean endwall flow field in loss production is in promoting boundary layer growth, and for L2A, outright flow separation.

6.6 Chapter Summary

As shown, the mean flow shear forces in the endwall wake are negligible in comparison to the turbulent shear forces, indicating that turbulence dissipation is the

dominant cause of mixing loss. Rather than causing mixing loss, the experiments using the boundary layer fences showed that the mean endwall flow field causes significant wake growth and flow separation on the suction surface. Flow separation gives rise to mixing, which in turn causes total pressure loss, predominantly by turbulence dissipation.

Endwall loss reduction methods in the literature (e.g., endwall contouring, fences, bulbs and fillets) have typically focused on manipulating the vortex structures to reduce losses. Based on the results of this chapter, however, design changes that attempt to suppress flow separation may also reduce endwall losses. As will be shown in the following chapters, front-loading the pressure distribution and using low stagger settings reduces separation on the suction surface and inlet endwall, respectively.

7. Effect of the Pressure Loading Distribution on Endwall Loss

In this chapter it will be shown that the pressure loading distribution significantly influences endwall loss, with front-loading reducing losses. Both the L1 and L2-series profiles are used in this investigation. For the L1-series profiles, the pitchwise spacing is identical with nearly equivalent stagger settings, leaving the pressure loading distribution as the primary difference between profiles. Similarly for the L2-series, the pitchwise spacing and stagger settings are identical, with the profiles differing only in the pressure loading distribution.

7.1 Experimental Comparison of L2A and L2F

Figure 6.2 shows that L2A produces a much larger wake than L2F, and hence more losses. The loss breakdown for both profiles is shown in Table 7.1. The passage loss, Y_{ps}, was calculated by assuming negligible changes in Y and the velocity field of Fig. 6.2 between 40% and 50% span and mass-averaging all Y downstream of the blade row. The profile loss, Y_{2D}, was calculated as the mass-averaged loss at 40% span. The endwall loss, Y_{ew}, is $Y_{ps} - Y_{2D}$. It is worth noting in Fig. 6.2a that the Y contours indicate that the L2A wake is not completely asymptotic (2D) at 40% span as it is for L2F in Fig. 6.2b. The large endwall wake of L2A combined with the unequal incoming endwall boundary layers on the tunnel roof and splitter plate precludes a well defined symmetry condition for that airfoil. Nevertheless, the change in the slope of the contour lines is small at 40% span and is not believed to change the result that L2A has higher levels of Y_{ps} and Y_{ew} than L2F. In fact, Y_{ew} for L2A is calculated to be +47% different than L2F.

Table 7.1 Experimental loss breakdown for the L2A and L2F profiles

	Y_{2D}	Y_{ps}	Y_{ew}
L2A	0.082	0.157	0.075
L2F	0.073	0.124	0.051

The result that Y_{ew} for the aft-loaded L2A profile is higher than Y_{ew} for the front-loaded L2F profile is significant, disagreeing with results typically found in the literature. Several studies including those of Weiss and Fottner (1995), Praisner et al. (2008), and Knezevici et al. (2009) have all suggested that front-loaded profiles have higher endwall loss than aft-loaded profiles. A common factor among all these studies is that the front-loaded profiles had higher stagger settings than the aft-loaded profiles used for making comparisons. For the current study, the L2A and L2F profiles have identical stagger settings. The results shown in Fig. 6.2 and Table 7.1 suggest that given the same stagger settings, Y_{ew} should be lower for front-loaded than aft-loaded profiles. The following section shows surface flow visualization results for L2A and L2F to explain the difference in Y_{ew}.

7.2 L2A and L2F Suction Surface Flow Visualization

Figure 7.1 shows the flow visualization results for L2A and L2F at Re = 100,000. (Appendix G discusses the flow visualization technique.) For both profiles, six dominant zones can be identified on the suction surface. Zones one to three indicate boundary layer flow upstream, within and downstream of a closed separation bubble, indicating 2D profile behavior. Zones four to six indicate the presence of the endwall flow. For both L2A and L2F, zone four represents a high shear zone, with the flow being driven up the span. Within the endwall boundary layer the fluid kinetic energy is low relative to the

flow closer to midspan, thus causing the fluid near the endwall to be overturned. Overturning causes the cross-passage boundary layer fluid to impinge upon the suction surface, generating the high shear of zone four. Farther away from the endwall in zone five, the surface shear appears to be weaker, but flow still migrates toward midspan. The spanwise migration of flow evident in zone four and five is responsible for generating the positive shed vorticity of Fig. 6.2. The most significant difference between L2A and L2F in relation to endwall loss is the placement and size of zone six. In zone six, the fluid remained stationary during the flow visualization experiment, suggesting separated flow. In Fig. 7.1a for L2A, zone six is quite large, essentially dividing zone three and five to cause endwall effects to propagate farther along the span. For L2F in Fig. 7.1b, zone six occurs closer to the endwall and deeper inside the passage than for L2A, thus limiting the propagation of endwall effects toward midspan. Zone effects are briefly summarized in Table 7.2.

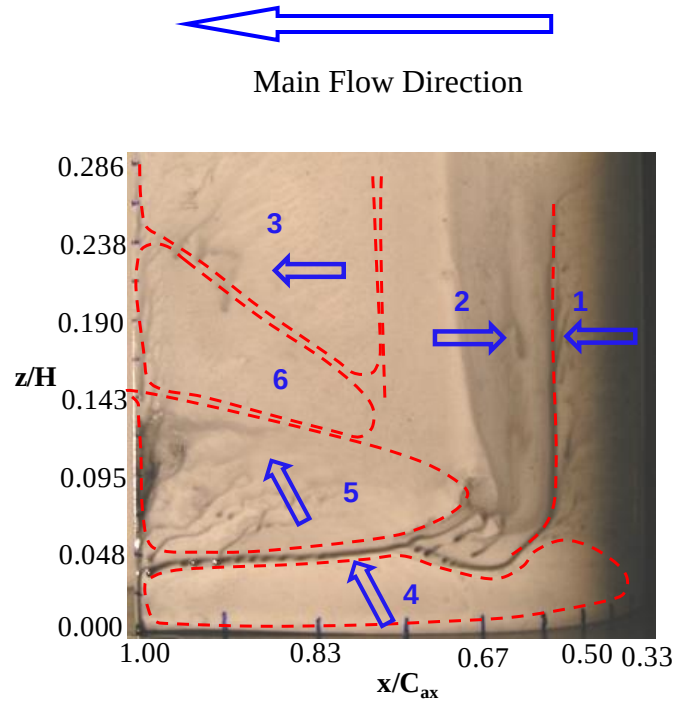

a) L2A, Re = 100,000

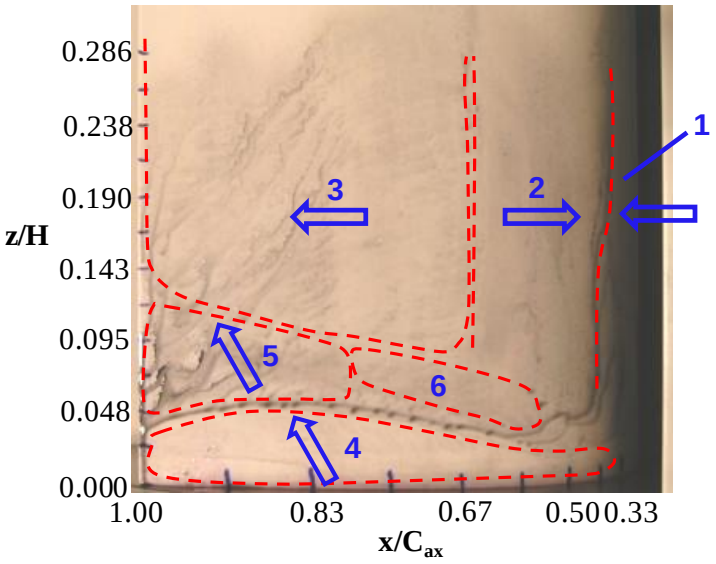

b) L2F, Re = 100,000

Fig. 7.1 Comparison of L2A and L2F suction surface flow visualizations

Table 7.2 Zone descriptions of suction surface flow behavior of the L2A and L2F profiles

Zone	Description
1	2D profile flow upstream of the separation bubble
2	2D profile flow inside the separation bubble; have reversed flow
3	2D profile flow downstream of separation bubble reattachment
4	Spanwise flow; has strong surface shear due to cross-passage flow impingement
5	Spanwise flow; surface shear weaker than zone 4 as the skewed boundary layer thickens
6	No oil flow motion indicating separated flow

The surface flow visualization results of Fig. 7.1 are in good agreement with the flow field and loss measurements shown in Fig. 6.2, in that L2A endwall effects propagate significantly farther toward midspan compared to L2F. Additionally, Y_{ew} for L2A is approximately +47% different than L2F. The large region of separated flow for L2A, zone six of Fig. 7.1a, suggests that the elevated Y_{ew} for L2A results from excessive flow separation due to the endwall flow. Considering the low Re midspan performance of this pair of profiles, it is not surprising that flow separation is a problem for L2A. As shown in Fig. 3.4, L2F performs much better at low Re than L2A. L2F is more resistant to flow separation than L2A due to front-loading.

The following section compares computational predictions using the LEO code of the L1 and L2-series profiles. The fully turbulent computations are useful for investigating the effect of the pressure loading distribution because separation bubbles are eliminated, typical of flows at higher Re than in the experiments for L2A and L2F. As will be shown, the computations indicate that for fixed stagger settings, front-loaded profiles produce less endwall loss than aft-loaded ones, thus agreeing with the experiments that have separation bubbles present.

7.3 Computational Comparison of the L1 and L2-series Profiles

The LEO code was used to calculate the Y_{ew} Reynolds lapse of the L1 and L2-series profiles. Although in general LEO under-predicts the dependency of the pressure loss on Re, results across a range of Re is useful to compare profiles. Y_{ew} is calculated as the difference between the passage loss, Y_{ps}, and the profile loss, Y_{2D}. Note that for calculating Y_{2D}, I used a separate 2D CFD model without endwalls. The reason for separate CFD models is because the midspan loss of the 3D passage is not necessarily equal to the profile loss in the absence of endwall effects, especially at low Re. Basically, the use of two CFD models for each profile allows endwall effects to be isolated from profile effects. Furthermore, Re values for the 2D and 3D CFD models were not identical due to Re being controlled indirectly via the backpressure. To calculate Y_{ew} at a specific Re, I used nonlinear power law curve fits to calculate Y_{ps} and Y_{2D} at the same Re value before taking the difference. Appendix J contains the data used for calculating Y_{ew} of the research profiles.

Figure 7.2 shows the Y_{ew} Reynolds lapse for the L1 and L2-series profiles. Results are shown for the L1A and L1M profiles in Fig. 7.2a. Recall that L1A is as aft-loaded whereas L1M is considered mid-loaded (See Fig. 3.3 to see the differences in pressure loading distribution). Both profiles have stagger settings similar to Pack B, which has $\lambda = 25.9^{\circ}$. As shown, Y_{ew} for L1A has a much stronger dependency on Re than L1M for Re < 90,000. For both profiles, the dependency on Re is quite small for Re > 90,000. For all Re, Y_{ew} is higher for aft-loaded L1A than mid-loaded L1M. The results for L2A and L2F shown in Fig. 7.2b also indicate that the aft-loaded L2A profile has higher endwall loss than the front-loaded L2F profile, agreeing qualitatively with the

experimental results of Table 7.1. Although both pairs of profiles indicate that aft-loading causes higher endwall loss, the L2-series profiles show a weaker dependency of Y_{ew} on Re than the L1-series. The difference in Re dependency between the two pairs of profiles may be due to differences in stagger angle.

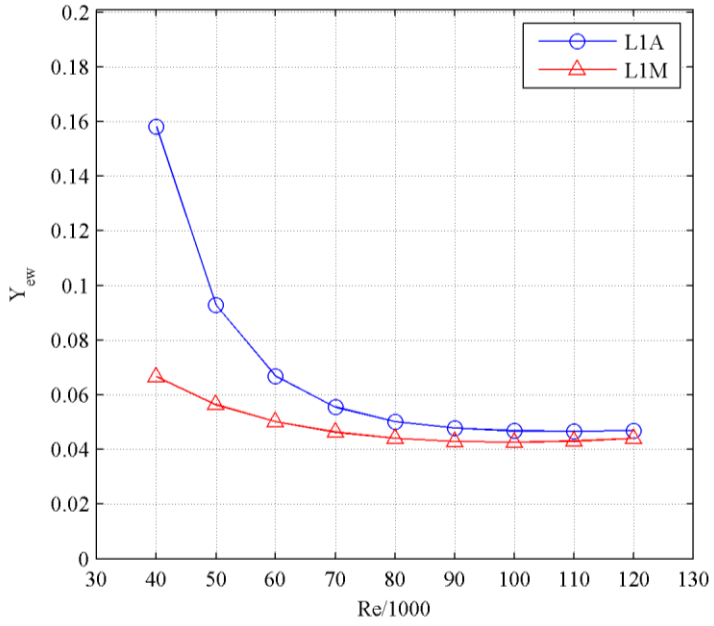

a) L1-series, $\lambda_{L1A} = 23.5^{\circ}$, $\lambda_{L1M} = 25.8^{\circ}$

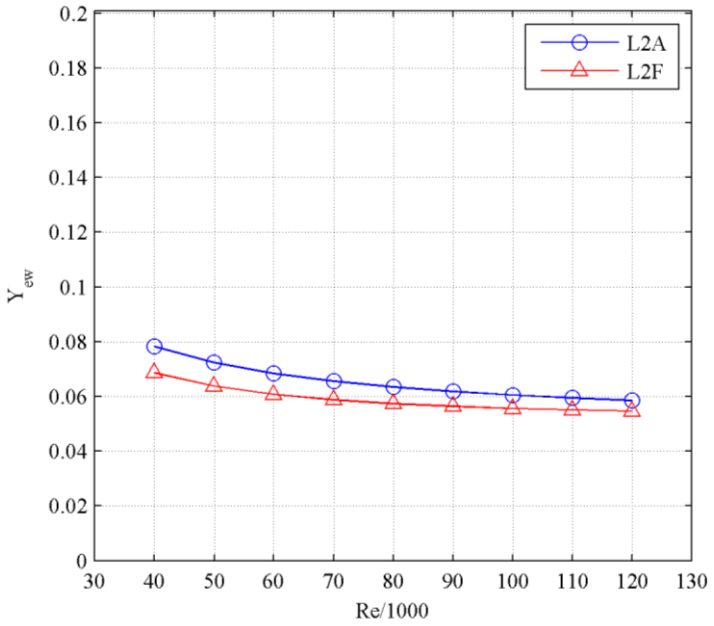

b) L2-series, $\lambda = 34.6^{\circ}$

Fig. 7.2 Effect of the pressure loading distribution on Y_{ew} for the L1 and L2-series profiles

To more easily compare results of the pairs of profiles in Fig. 7.2, Fig. 7.3 shows the ratio of Y_{ew} of the aft-loaded profiles to that of the more front-loaded profiles. As

shown for the L1-series, calculations predict Y_{ew} for L1A to exceed that of L1M by more than a factor of two at low Re. The predictions suggest more modest differences between the pair of L2-series profiles.

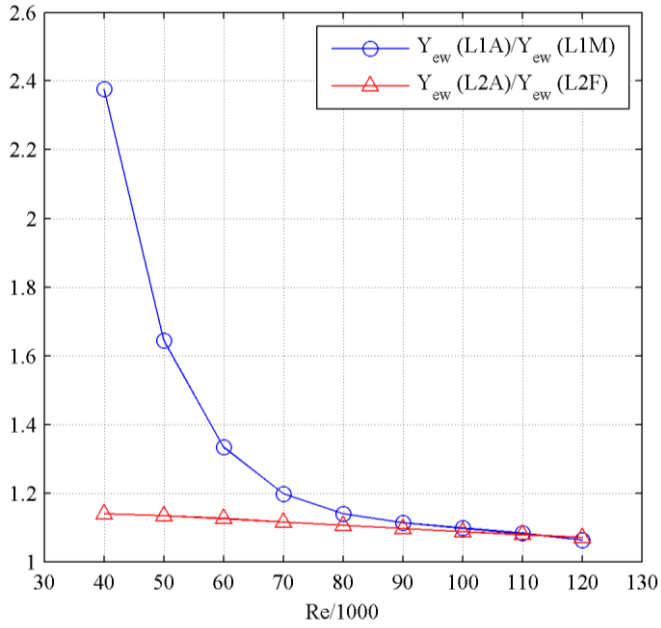

Fig. 7.3 Endwall loss ratio of aft-loaded to more front-loaded profiles

7.4 Chapter Summary

The results of this chapter indicate that for fixed stagger angles, front-loading profiles reduces Y_{ew}. The combination of experiments and fully turbulent CFD suggest that this conclusion regarding the pressure distribution holds at low and high Re (with and without separation bubbles on the profile). Surface flow visualizations suggest that front-loading reduces Y_{ew} by suppressing wake growth and separation on the suction surface.

The contrast with the current work of past studies that concluded that front-loading increases Y_{ew} suggests the presence of another endwall loss-generating

mechanism responsible for the difference. It is suggested that the high stagger angles of the front-loaded profiles of past studies may have led to the conclusion that front-loading increases Y_{ew}. The following chapter investigates the effect of the stagger angle on Y_{ew} to isolate the effects of the stagger angle and pressure loading distribution.

8. Effect of the Stagger Angle on Endwall Loss

This chapter presents the results of a computational study of the influence of the stagger angle on endwall loss, Y_{ew}. All results were computed using the LEO code. To begin the discussion, results for the L1M and L2F research profiles are compared with those of Pack B. L1M has a similar stagger angle as Pack B, whereas the L2F stagger angle is 8.7˚ higher than for Pack B. The computational results are compared to a similar set of airfoils from the literature. To provide a more direct comparison of stagger angle effects, results for L2F are also compared to a new profile, designated L2F-LS (L2F-"low stagger"). The L2F-LS profile was designed to the same gas angles and pitchwise spacing with similar front-loading as L2F, but with the L1M stagger angle. (Appendix K documents the design of L2F-LS.) Results of this chapter indicate that increasing the stagger angle increases Y_{ew}.

8.1 Computational Comparison of L1M and L2F with Pack B

To investigate the effect of the stagger angle, Y_{ew} of the L1M and L2F profiles is compared with that of Pack B. For context, the computational results are compared to the experiments of Zoric et al. (2007) who compared Y_{ew} of the Pack DA and Pack DF profiles to that of Pack B. Cascade geometries of the profiles just mentioned are shown in Table 8.1. Both the L1M and Pack DA profiles have stagger angles similar to Pack B, whereas L2F and Pack DF have significantly higher stagger angles. One problem with using the L1M and L2F profiles to demonstrate the effect of the stagger angle is that the pitchwise spacing is not matched, arguably confounding the results. The Pack DA and Pack DF profiles, however, have identical pitchwise spacing and differ only by the

stagger setting and pressure loading distribution, with the latter effect demonstrated in the previous chapter. Pack DA and Pack DF are aft and front-loaded, respectively. Therefore, it is believed that meaningful conclusions can be drawn regarding the effect of the stagger angle using results of the available profiles. The results will be shown for Re = 80,000 to correspond to the test condition of Zoric et al. (2007). Also note that the results of Zoric et al. (2007) that will be shown are with approximately 4% inlet turbulence levels.

Table 8.1 Comparison of profile geometries used to study stagger angle effects

	Pack B, LEO	L1M, LEO	L2F, LEO	Pack B, Zoric et al. (2007)	Pack DA, Zoric et al. (2007)	Pack DF, Zoric et al. (2007)
Re	80,000	80,000	80,000	80,000	80,000	80,000
S/C_{ax}	0.885	1.011	1.221	.885	1.105	1.105
H/C_{ax}	3.5	3.5	3.5	2.69	2.67	2.67
$\lambda, ^\circ$	25.9	25.8	34.6	25.9	26	35.4
$\alpha_{in}, ^\circ$	35	35	35	35	35	35
$\alpha_{ex}, ^\circ$	-58.5	-57.63	-58.12	-60*	-60*	-60*
Z_w	1.13	1.32	1.57	1.08	1.37	1.37

* Praisner et al. (2008) states that these angles are metal angles, not flow angles

Figure 8.1 shows the ratio of Y_{ew} of the L1M, L2F, Pack DA and Pack DF profiles to that of Pack B. First considering the results using LEO for the L1M and L2F profiles, Y_{ew} of low stagger L1M exceeds Y_{ew} of Pack B by approximately 5%. Y_{ew} of high stagger L2F, however, exceeds Y_{ew} of Pack B by approximately 37%. Zoric et al. (2007) also shows significant differences between the low and high stagger profiles. The low stagger Pack DA profile actually has approximately 7% lower Y_{ew} than Pack B. Similar to L2F, the high stagger Pack DF profile produces Y_{ew} levels exceeding Pack B by approximately 39%. In their paper, Zoric et al. (2007) attributed the difference in Y_{ew} between the Pack DA and Pack DF profiles to the effect of the pressure loading

distribution. Results of the current work, however, indicate that given the same stagger angles, aft-loaded profiles are expected to have higher Y_{ew} than front-loaded profiles. Therefore, the difference in Y_{ew} between L1M and L2F and between Pack DA and Pack DF is likely due to the difference in stagger angle.

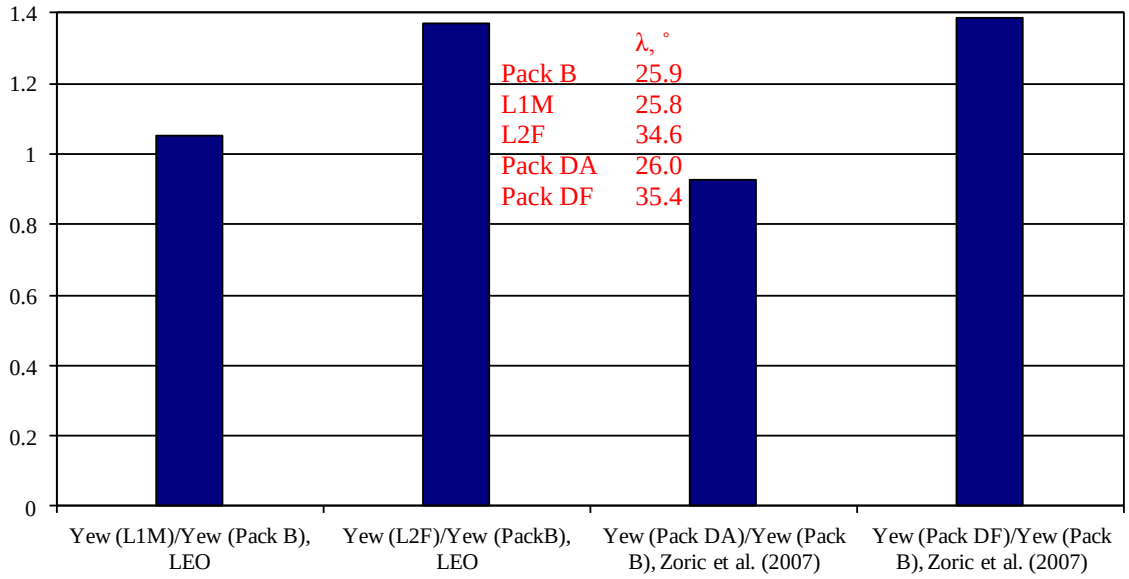

Fig. 8.1 Comparison of the ratio of Y_{ew} of several profiles to Y_{ew} of Pack B to show stagger angle effects

The reason the stagger angle influences Y_{ew} can be found by investigating the effect of the static pressure field on the incoming inlet boundary layer flow. As will be shown, a high stagger angle causes a larger fraction of the inlet boundary layer to separate, generating a larger blockage near the passage inlet and increasing the total pressure loss. The separated inlet boundary layer flow is driven across the passage to the neighboring suction surface, increasing the size of the endwall wake.

Figure 8.2 shows the effect of the static pressure field on the inlet boundary layer flow of the low stagger Pack B and high stagger L2F profiles. The Cp contours are

drawn in a spanwise plane at ½ the inlet boundary layer thickness. Accordingly, the streamlines are released from the same plane as they enter the flow domain. As shown for both profiles in Figs. 8.2a and 8.2b, the streamlines indicate that the inlet boundary layer fluid cannot enter the high-pressure region of the passage, as indicated by the Cp = 0.5 contour line. For the high stagger L2F profile, the Cp = 0.5 line becomes nearly orthogonal to the incoming boundary layer fluid near the leading edge. As a result, the saddle point of the inlet boundary layer separation for L2F is moved away from the leading edge into the passage. This effect on the inlet boundary layer separation can also be seen in Figs. 8.3a and 8.3b, which show close-up images of the horseshoe vortex formation of Pack B and L2F, respectively. As shown, the horseshoe vortex forms near the Pack B leading edge, but more offset from the L2F leading edge. The significance of the horseshoe vortex moving off the leading edge is that more fluid is likely to be entrained in the horseshoe vortex to be driven across the passage.

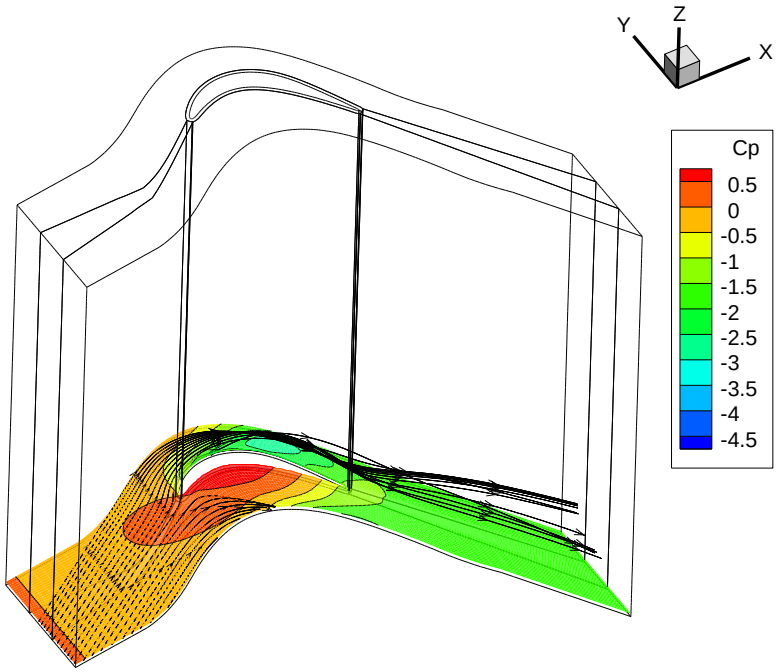

a) Pack B inlet boundary layer streamlines

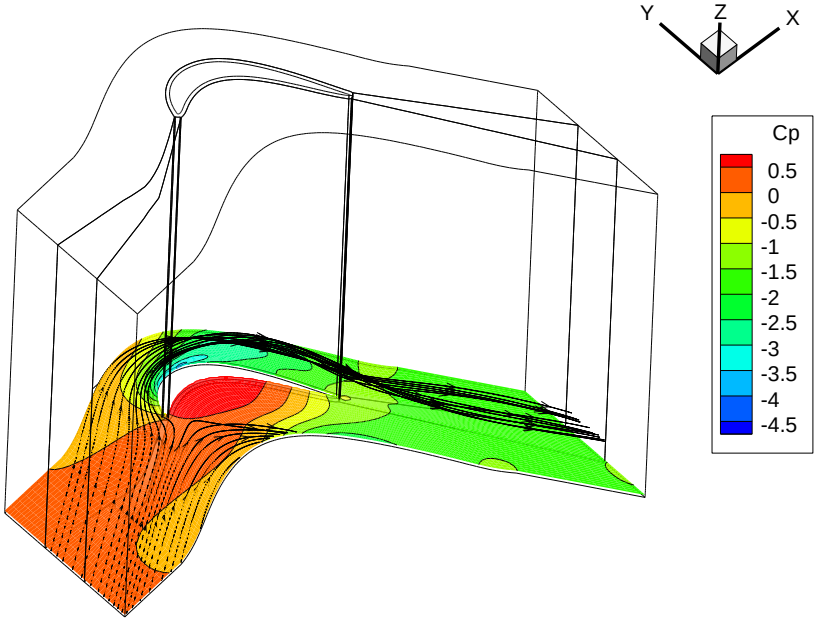

b) L2F inlet boundary layer streamlines

Fig. 8.2 Effect of the static pressure field on the inlet boundary layer flow for the Pack B and L2F profiles (Streamlines initiated at ½ the inlet boundary layer thickness)

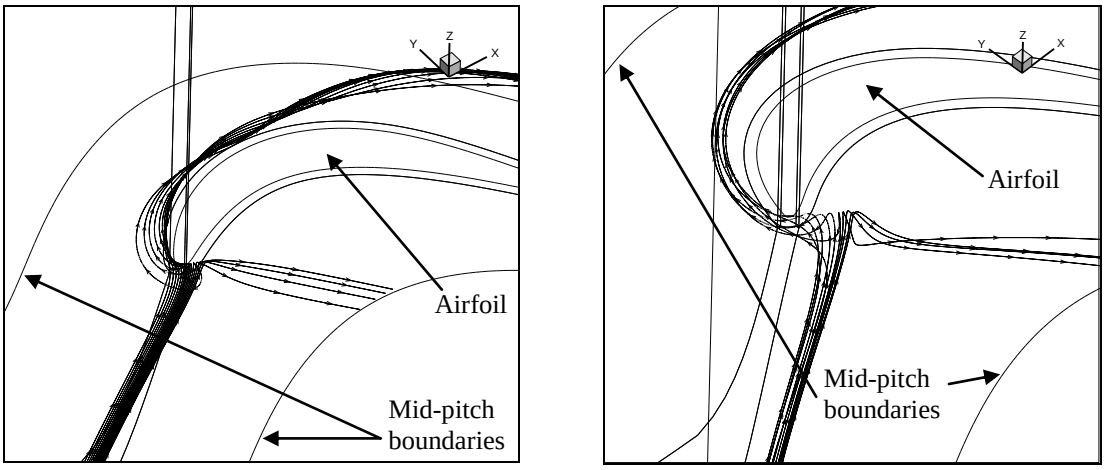

a) Pack B b) L2F

Fig. 8.3 Horseshoe vortex formation of the Pack B and L2F profiles (Streamlines initiated at ½ the inlet boundary layer thickness)

To further demonstrate the effect of the stagger setting on the inlet boundary layer separation, Fig. 8.4 shows streamlines approaching the leading edge of the Pack B and L2F profiles initiated at the edge of the inlet boundary layer as opposed to half the inlet boundary layer height. As shown for Pack B, the streamlines pass through the passage. For L2F, however, streamlines are still entrained as part of the horseshoe vortex. It is the pressure side leg of the horseshoe vortex that is driven across the passage to the neighboring profile suction surface to increase the size of the endwall wake.

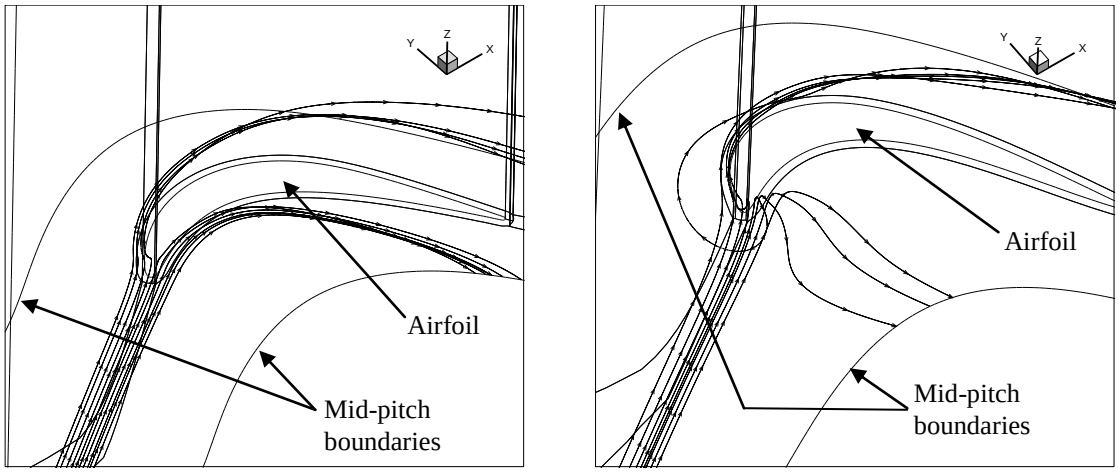

a) Pack B

a) L2F

Fig. 8.4 Leading edge streamlines showing more entrainment of inlet boundary layer fluid for L2F compared to Pack B (Streamlines released at the edge of the inlet boundary layer)

To avoid concerns of confounding the results when investigating stagger angle effects, the following section compares L2F predictions with the new L2F-LS profile. (Appendix K documents the design of L2F-LS.) Both profiles have the same pitchwise spacing and approximate gas angles. Front-loading and stall resistance, similar to L2F, is achieved during design by manipulating the boundary layer force parameter (BLFP), defined in Eq. 3.10. The stagger angle of L2F-LS, however, is 8.8˚ smaller than for L2F, the only significant difference between the two airfoils. Passage and endwall performance are shown to compare the two profiles.

8.2 Computational Comparison of the L2F and L2F-LS Profiles

Predicted Y_{ew} and Y_{ps} calculations using LEO for L2F and L2F-LS are shown in Fig. 8.5. Although the LEO code is expected to under-predict the Re dependency compared to experiments, results over a range of Re are still useful to compare profiles. As shown in Fig. 8.5a, there is little difference in Y_{ps} between the two profiles for Re >

80,000. Y_{ew} of L2F-LS is significantly lower compared to L2F at high Re, yet excessive Y_{2D} causes Y_{ps} to be nearly equivalent for the two profiles. At low Re, however, the low stagger L2F-LS profile is predicted to have a stronger Re dependency in Y_{ew} than L2F, leading to increased Y_{ps} at low Re. Considering results of Y_{ps} across the whole Re range, L2F can arguably be considered the better performing profile. The low Y_{ew} of L2F-LS, however, is a desirable design feature. As shown in Fig. 8.5b, L2F-LS produces over 20% less Y_{ew} than L2F for Re > 70,000.

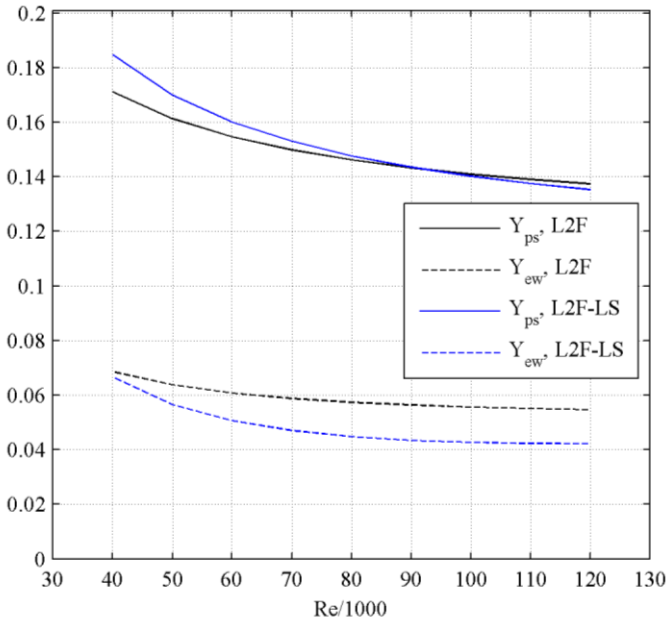

a) Comparison of Y_{ew} and Y_{ps}

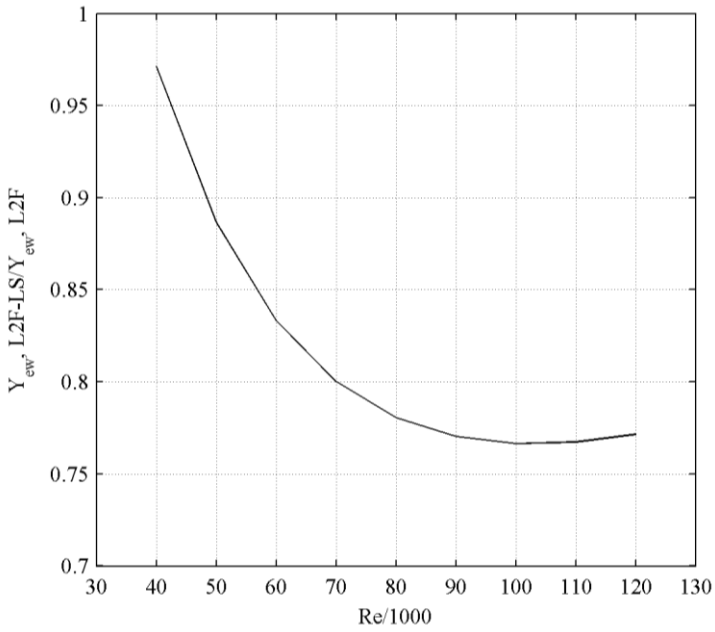

b) L2F-LS Y_{ew} reduction

Fig. 8.5 Comparison between L2F and L2F-LS Y_{ew} and Y_{ps} performance

The results of Fig. 8.5 support the hypothesis that the stagger setting, λ, has a significant effect on Y_{ew}. As suggested in Figs. 8.2 through 8.4, the stagger setting is

expected to influence the inlet boundary layer separation that forms the horseshoe vortex. High stagger profiles tend to produce a stronger blockage relative to the incoming endwall boundary layer flow. As a result, more fluid is entrained in the horseshoe vortex. When in the presence of the adverse pressure gradient adjacent to the suction surface, the higher volume of low energy fluid produces a larger wake.

Figure 8.6 shows surveys of Y and secondary velocity vectors computed using LEO for L2F and L2F-LS to see the qualitative effect of the stagger angle on the endwall wake. The results are plotted to be consistent with the measurement plane of Fig. 4.2. As shown for L2F in Fig. 8.6a, the dominant loss core is located approximately at y/S = 0.35 and z/H = 0.20. The velocity vectors indicate that the passage vortex is approximately centered at y/S = 0.45 and z/H = 0.07. In contrast, the dominant loss core of the L2F-LS profile in Fig. 8.6b occurs much closer to the endwall compared to L2F, approximately at y/S = 0.52 and z/H = 0.11. The L2F-LS passage vortex is centered approximately at y/S = 0.50 and z/H = 0.07. The secondary velocity vectors surrounding the approximate center of the L2F passage vortex appear on average to be longer than for L2F-LS, suggesting a stronger endwall flow. The stronger endwall flow of L2F is a direct result of the high stagger angle that causes a larger mass of the inlet boundary layer to separate and become part of the vortex structures. Accordingly, the stronger endwall flow drives the low energy cores closer to midspan for the high stagger L2F profile.

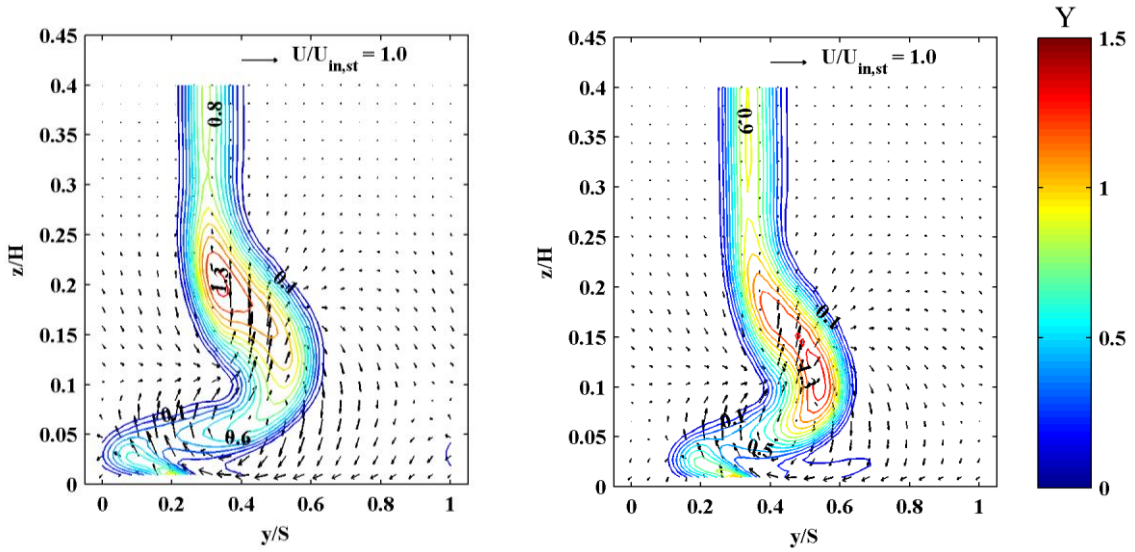

a) L2F b) L2F-LS

Fig. 8.6 Comparison of predicted surveys using LEO of Y (ΔY = 0.1 for contours) and secondary velocity vectors downstream of the blade row at Re = 100k (See Fig. 4.2 for coordinate system origin and orientation)

8.3 Chapter Summary

The results of this chapter indicate that increasing the stagger angle increases endwall loss, primarily by strengthening the inlet boundary layer separation. Hence, high stagger blade rows collect more low energy boundary layer fluid in the horseshoe vortex than low stagger blade rows. Increasing the stagger angle is common to achieve front-loading for high lift LPT profiles and may explain why several past studies have concluded that front-loaded profiles have higher endwall loss than aft-loaded ones.

The low stagger version of L2F designed to study stagger angle effects, L2F-LS, reduced endwall losses more than 20% for Re > 70,000. High profile loss, however, negated the benefit of the reduced stagger angle, leading to similar overall passage loss for L2F and L2F-LS. The following chapter presents the results of an attempt to exploit the benefit of reduced stagger angle through use of profile contouring at the endwall of

the L2F airfoil. As will be shown, using a low stagger profile at the endwall can provide a significant endwall loss reduction.

9. Endwall Loss Reduction through Use of Profile Contouring

This chapter documents the design and performance of a new airfoil, designated L2F-EF (L2F-"endwall fillet"), that was designed by contouring the L2F airfoil at the endwall to obtain the benefit of low stagger angle. Contouring the airfoil generates a fillet that extends out from the pressure surface, primarily in the pitchwise direction toward the adjacent suction surface. As will be shown, L2F-EF predictions suggest endwall loss reductions between 15% and 20% for Re > 60,000. Experiments at Re = 100,000 showed an approximate 22% endwall loss reduction for the contoured L2F-EF airfoil.

9.1 Design of the L2F-EF Airfoil

The L2F-EF airfoil was designed by contouring the L2F airfoil near the endwall to transition from the L2F profile to L2F-LS at the endwall. L2F-LS is the low stagger version of L2F, the design of which is described in Appendix K. Figure 9.1 shows L2F-EF near the endwall where it transitions from L2F to the L2F-LS profile shape. The fillet shape is visualized in Fig. 9.1 using airfoil coordinates in k-planes near the endwall that were generated using the WAND code for use with the LEO flow solver. The thick blue line in Fig. 9.1 illustrates the transition from L2F-LS at the endwall to the L2F profile. The point where the blue line straightens indicates the fillet height. As will be shown later, Y_{ps} is fairly insensitive to the fillet height.

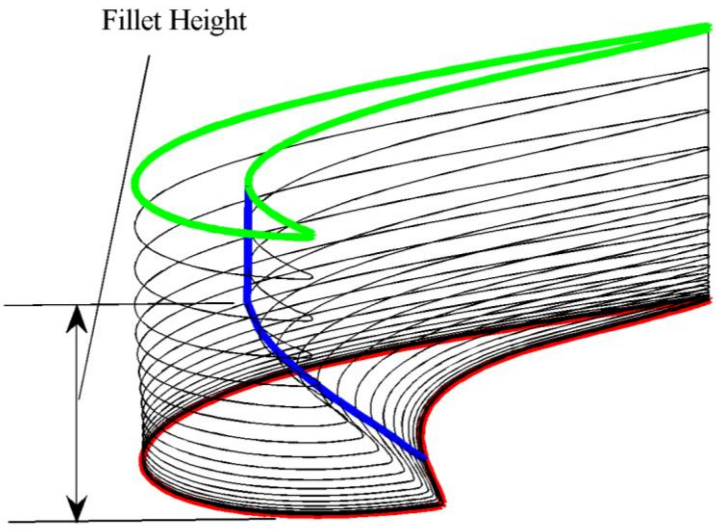

a) Fillet shape

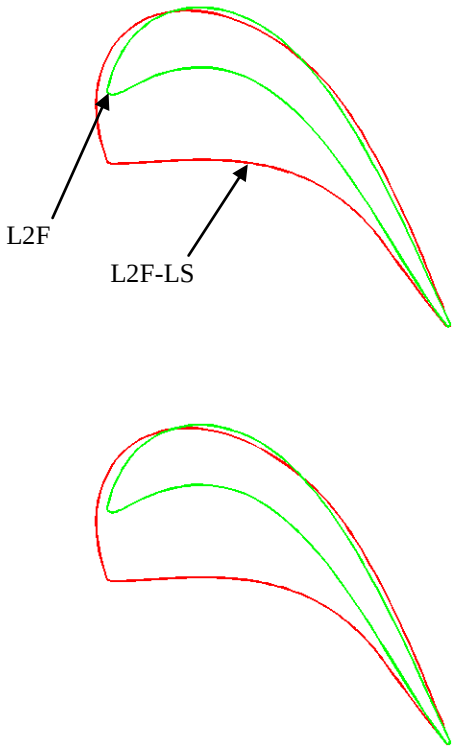

b) Profile comparison

Fig. 9.1 Illustration of the L2F-EF airfoil near the endwall to show the fillet shape

The fillet shape was generated using the WAND code. WAND can be used to generate whole airfoils from a small number of defined profile shapes along the span. For example, a designer may define airfoil shapes at the endwall, at midspan and at the tip to model a rotor blade accounting for radial equilibrium. The WAND code uses spline interpolation to generate the mesh along the whole span that passes through the defining profiles. I used this method to generate the fillet shape of Fig. 9.1 by defining the L2F-LS profile at the endwall and the L2F profile at the chosen fillet height. A second L2F profile shape was placed approximately 2% span on towards midspan, above the chosen fillet height. Together, the two L2F profiles placed at the edge of the desired fillet functioned as control points for the spline interpolation along the span. As shown in Fig. 9.1, the fillet appears smooth.

Intuitively, one might expect the fillet height to influence the total pressure loss. Ultimately a trade-off exists between excessive Y_{2D} of the L2F-LS profile if the fillet height is too large and excessive Y_{ew} due to L2F if the fillet height is too small. (Figure 8.5 shows the limiting cases of straight L2F and L2F-LS airfoils.) To determine the sensitivity I used LEO to calculate Y_{ps} for several fillet heights at Re = 100,000. As shown in Fig. 9.2, the results indicate that Y_{ps} is fairly insensitive to the fillet height. Nevertheless, the fillet height of approximately z/H = 0.095 gives minimum loss among the cases considered, so that fillet height was chosen for the L2F-EF design. The z/H = 0.095 fillet height is the design shown in Fig. 9.1.

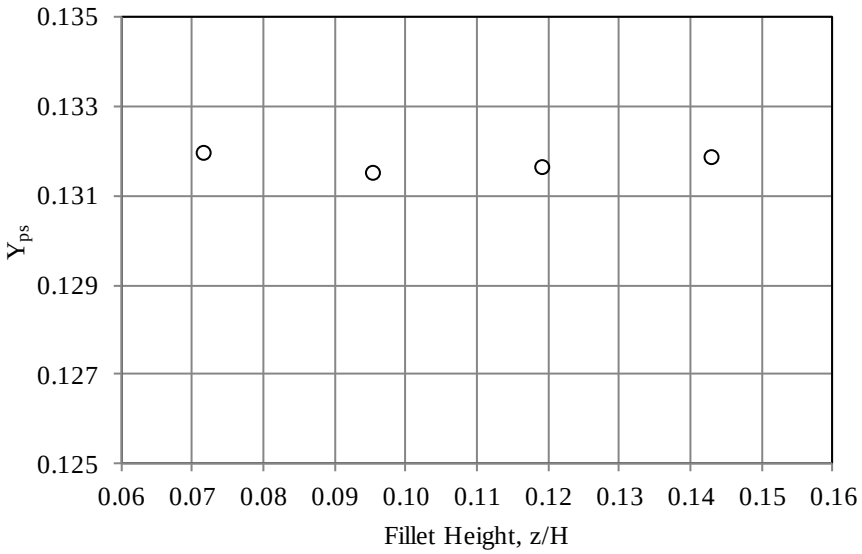

Fig. 9.2 Sensitivity of L2F-EF Y_{ps} to the fillet height, Re = 100k

Based on computational predictions using LEO, the following section discusses how L2F-EF performs compared to L2F. Results are also compared to L2F-LS to determine if using profile contouring to achieve the benefit of low stagger angle (i.e., the technique used to design L2F-EF) retains the endwall loss reduction benefit of L2F-LS. Predictions are also provided to compare the performance of the high lift L2-series airfoils to the conventional lift Pack B baseline design.

9.2 L2F-EF Computational Endwall and Passage Performance

Figure 9.3 compares the reduction in Y_{ew} of L2F-EF with that of L2F-LS. At high Re, the L2F-EF airfoil does not provide as much loss reduction as L2F-LS, but well over half of the loss reduction is retained using the fillet. Because of the transition between the two profile shapes, it is not surprising that L2F-EF does not have as much of a reduction in Y_{ew} as L2F-LS. Nevertheless, the L2F-EF predictions suggest a significant

loss reduction for all Re examined. At Re ≈ 56,000, the two curves intersect due to a strong Re dependency for L2F-LS at low Re. The result of a strong dependence of Y_{ew} on Re for the low stagger L2F-LS profile is in agreement with LEO calculations in Fig. 7.2a for the low stagger L1A and L1M profiles. The addition of the fillet of the L2F-EF airfoil partially retains the weaker Re dependency of Y_{ew} shown in Fig. 7.2b for L2F, yet at high Re Y_{ew} is higher than for L2F-LS. Although L2F-EF does not reduce Y_{ew} as much as L2F-LS, the results still suggest that contouring the airfoil to reduce the stagger angle at the endwall can significantly reduce Y_{ew}.

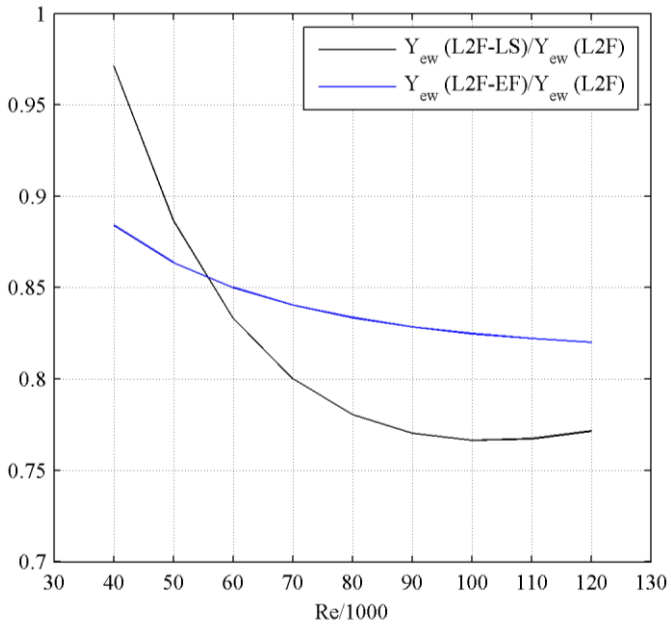

Fig. 9.3 Comparison of Y_{ew} reduction between L2F-LS and L2F-EF

To compare the L2-series airfoils to a conventional lift design, Fig. 9.4 compares Y_{ps} of the high lift profiles with that of Pack B. As shown in Fig. 9.4a, both L2F and L2F-LS have noticeably higher Y_{ps} than Pack B for all Re considered. Although Y_{ps} of

L2F-EF is also higher than for Pack B, Y_{ps} is significantly reduced. To more easily quantify the differences in Y_{ps}, Fig. 9.4b shows the ratio of Y_{ps} of the high lift designs to that of Pack B. According to Zoric et al. (2007), the design Re for Pack B is Re = 80,000. At the design point, predicted Y_{ps} of L2F is nearly 10% higher than for Pack B. The addition of the fillet used for L2F-EF reduces predicted Y_{ps} to within 2.5% of Pack B at the design point. At the low and high extremes of Re, the predicted difference in Y_{ps} between L2F-EF and Pack B is less than 2%. Considering that Pack B is expected to begin to stall for Re < 50,000 (See Fig. 3.4), it is likely that L2F-EF will actually perform much better at low Re than Pack B.

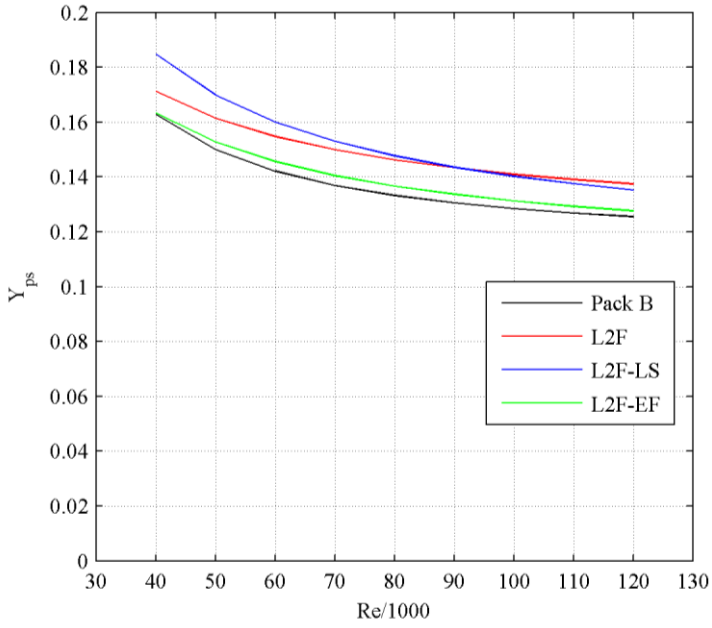

a) High lift Y_{ps} compared with Pack B Y_{ps}

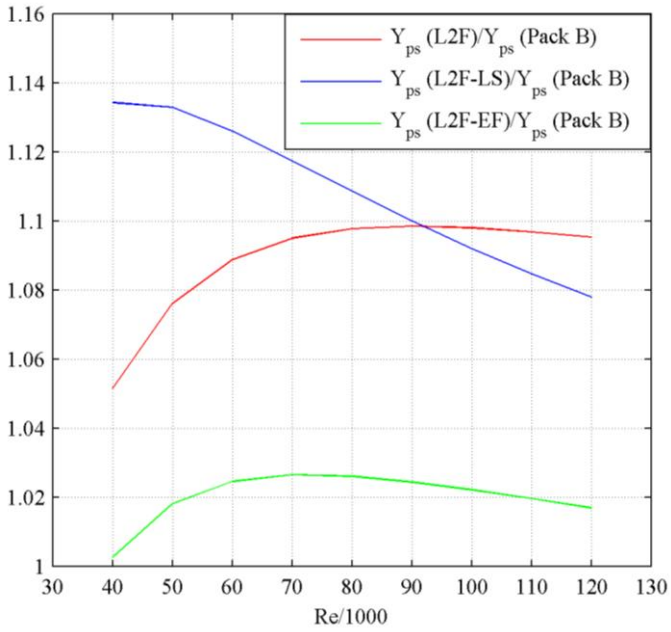

b) High lift Y_{ps} scaled to Y_{ps} of Pack B

Fig. 9.4 Comparison of high lift Y_{ps} to Y_{ps} of the conventionally loaded Pack B

Figure 9.5 shows that elevated Y_{ew} is why Y_{ps} of L2F-EF is predicted to remain slightly higher than for Pack B. At the Pack B design point of Re = 80,000, Fig. 9.5b

shows that Y_{ew} for L2F-EF is estimated to be 14% higher than for Pack B. However, the difference between L2F-EF and Pack B is a significant improvement compared to L2F that has approximately 37% higher Y_{ew} than Pack B.

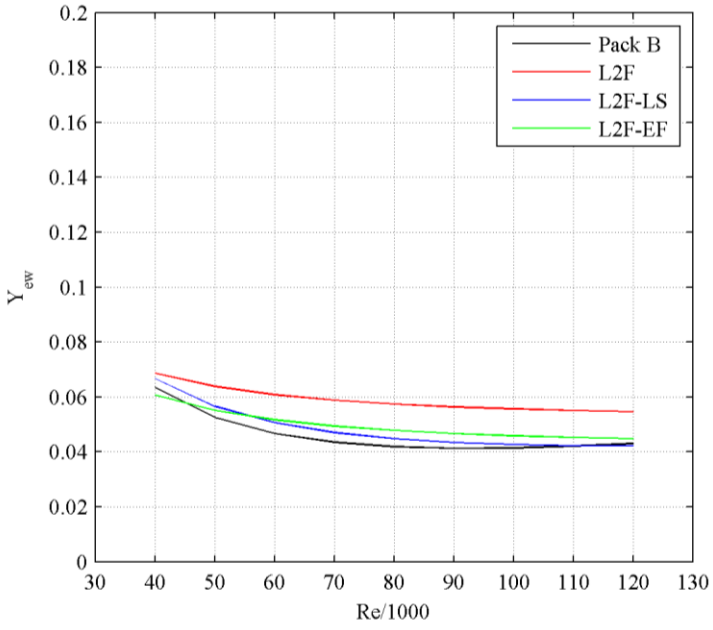

a) High lift Y_{ew} compared with Pack B Y_{ew}

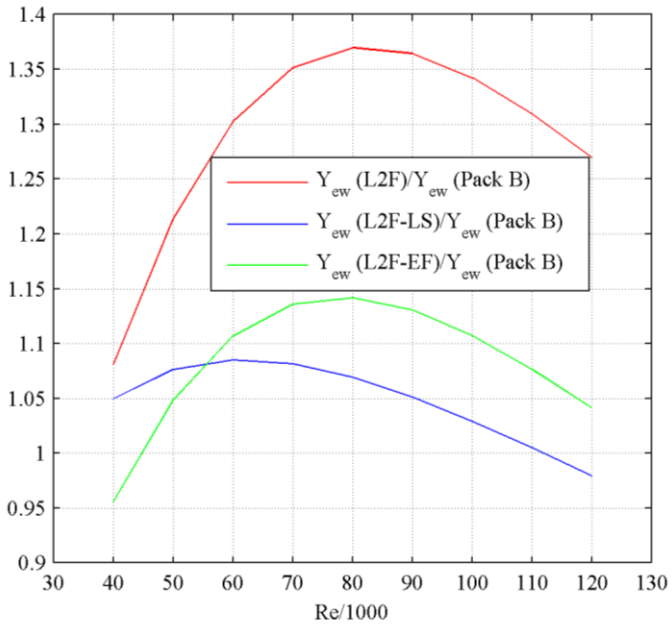

b) High lift Y_{ew} scaled to Y_{ew} of Pack B

Fig. 9.5 Comparison of high lift Y_{ew} to Y_{ew} of the conventionally loaded Pack B

Having shown computationally that contouring the L2F airfoil at the endwall to reduce the stagger angle can reduce Y_{ew}, the following section describes an experiment to validate the computational results.

9.3 L2F-EF Experimental Endwall and Passage Performance

A stereolithography (SLA) model of the fillet at the L2F endwall was fabricated to mimic the design of the L2F-EF airfoil. Fillets were designed and fabricated to be attached to the three center airfoils in the wind tunnel. Figure 9.6 shows a close-up CAD model of the fillet to show how it appears attached to the L2F leading edge. The fillet was designed primarily by subtracting the geometry of the straight L2F airfoil from L2F-EF, leaving the fillet.

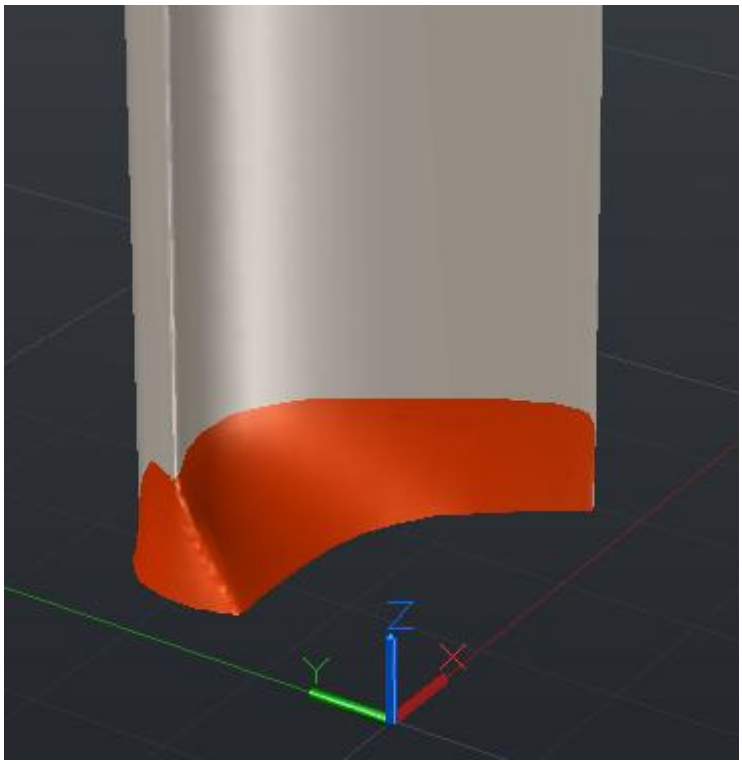

Fig. 9.6 CAD model of the fillet modification used to mimic the L2F-EF airfoil design

The base of the fillet is primarily defined as the L2F-LS profile. As one notes in Fig. 9.1, however, the L2F and L2F-LS suction surfaces intersect twice. During design, material was discarded aft of the first intersection of the profiles closest to the leading edges to permit attaching the fillets to existing airfoils. Thus, the suction surfaces of the resulting airfoils tested in the wind tunnel were slightly different near the endwall than the airfoil modeled in CFD. This difference is expected to be insignificant because close to the endwall, the endwall boundary layer flow is overturned and impinges on the suction surface. Therefore, spanwise flow dominates close to the endwall as opposed to flow parallel to the endwall (See Fig. 7.1).

Table 9.1 shows a comparison of the total pressure loss with and without the fillet at the L2F endwall for Re = 100,000. The results are based on area averages since no velocity data were available for the fillet modification. Since endwall effects can have an influence along the whole span, Y_{2D} is based on the profile loss measurements of Appendix C for both cases to isolate the effect of the fillet. As shown, the fillet reduces Y_{ew} approximately 22%, which falls between the predicted Y_{ew} reductions of L2F-LS and L2F-EF in Fig. 9.3 at Re = 100,000. The reduction in Y_{ew} leads to a 9% reduction in Y_{ps}. Overall, the results of Table 9.1 indicate that profile contouring to implement a low stagger angle at the endwall can effectively reduce endwall losses.

Table 9.1 L2F loss breakdown with and without the fillet (Re = 100k)

	No Fillet, L2F	With Fillet, L2F-EF	% Diff
Y_{2D}	0.078	0.078	0
Y_{ps}	0.133	0.121	-9.0
Y_{ew}	0.055	0.043	-21.8

Figure 9.7 shows Y contours with and without the fillet, captured in the measurement plane of Fig. 4.2 to see the effect of the fillet on the endwall wake. As shown, two low energy cores are present for both cases. The dominant loss core without the fillet, midwake at z/H = 0.18, moves closer to the endwall to z/H = 0.14 with the fillet. The second loss core without the fillet, approximately at z/H = 0.08, moves slightly away from the endwall to z/H = 0.10, resulting in the pair of loss cores covering a smaller area with the fillet. The smaller area coverage of the loss cores suggests that less low energy fluid is contained in the wake, directly resulting from a weakened inlet boundary layer separation (or equivalently a reduced horseshoe vortex) due to the low stagger angle at the endwall.

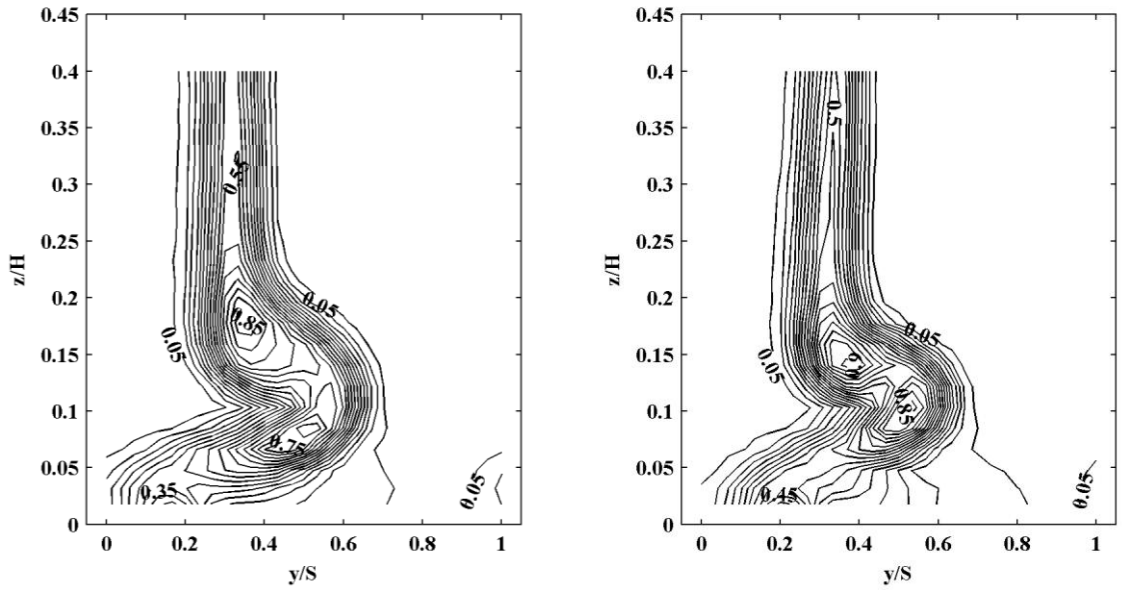

L2F, No Fillet L2F-EF, With Fillet

Fig. 9.7 Comparison of L2F and L2F-EF Y contours (Re = 100k) (ΔY = 0.05)

9.4 Chapter Summary

The results of this chapter, based on both experiments and CFD, suggest that contouring high lift LPT airfoils at the endwall to reduce the stagger angle can reduce endwall losses. Experiments at Re = 100,000 showed a 22% endwall loss reduction, leading to a 9% reduction in passage loss. The loss reduction was achieved by weakening the inlet boundary layer separation that forms the horseshoe vortex, resulting in less low energy boundary layer fluid in the endwall wake.

Past high lift LPT research has shown that non-axisymmetric endwall contouring can also provide significant endwall loss reductions, but with different reasoning than used for profile contouring. Both methods can perhaps be combined to provide further improvements to high lift LPT performance.

10. Conclusions

This chapter discusses conclusions based on the results of the work. The discussion begins with the fluid mechanics of endwall loss production, followed by pressure loading and stagger angle effects. Finally, recommendations for future work are provided.

10.1 Fluid Mechanics Effects on Endwall Loss

The study of the fluid mechanics of endwall loss in this work focused on the roles of the mean flow and turbulence fields. The results suggest a rather simple heuristic view of endwall loss production. Separation of the inlet boundary layer (as the horseshoe vortex forms) and on the suction surface can be viewed as initial steps to loss production. Total pressure loss occurs mainly due to turbulence dissipation as mechanical energy is transferred from high to low speed, separated fluid during mixing. Therefore, design changes that limit flow separation are expected to reduce endwall losses. The pressure loading distribution and stagger angle, discussed in the following section, significantly influence flow separation.

10.2 Front-Loading and Stagger Angle Effects on Endwall Loss

High lift LPT airfoils with good low Reynolds number performance usually have front-loaded pressure distributions with high stagger settings relative to conventional lift airfoils. Past studies have shown that such high lift airfoils produce excessive endwall loss, usually attributing the high loss to the front-loaded pressure distribution. Results of the current work, however, indicate that the high stagger angle, not front-loading is the

cause of high endwall loss. For fixed stagger angles, results indicated that more front-loaded airfoils produce less endwall loss than aft-loaded ones, primarily by suppressing suction surface flow separation near the endwall. Increasing the stagger angle increases endwall loss because the pressure surfaces of the profiles are closer to being oriented orthogonal to the inlet boundary layer flow. Such a realignment of the pressure surface generates a stronger static pressure blockage that causes more inlet boundary layer fluid to be entrained in the horseshoe vortex.

Experimental total pressure loss results of a high lift, front-loaded airfoil that was contoured at the endwall to exploit the benefits of reduced stagger angle indicated a 22% reduction in endwall loss, leading to a 9% overall passage loss reduction. In light of the results of the current work, conventional methods for designing profiles at the middle of an airfoil are believed to be acceptable. At the endwall, however, the stagger angle should be a constraint because of its significant effect on endwall loss.

10.3 Recommendations for Future Work

A recommended direction of future research is to combine the high lift airfoil loss reduction method of profile contouring with other loss reduction techniques. Besides contributing to the understanding of endwall loss of high lift profiles, a goal of the current work was to find an alternative loss reduction technique that can be added to established techniques. The most commonly reported endwall loss reduction method in the literature is non-axisymmetric endwall contouring. Since the focus of the current work was on the effects of the profile shape while maintaining flat endwalls, perhaps contouring the endwall can provide additional loss reduction benefits.

Finally, one must also consider that there are significant differences between linear cascade flows and annular LPT stages. To be practical, design modifications must also provide a benefit to both stationary and rotating blade rows. Besides radial equilibrium considerations and purge and sealing flows, the inlet boundary layer changes reference frames between rotating and stationary blade rows, thus skewing the endwall boundary layer. Additionally, blade rows in real machines experience positive and negative incidence during off design operation, providing additional challenges. For both on and off design operational conditions, high lift airfoils must produce acceptable overall passage loss compared to conventional lift designs to be practical.

Appendix A: Comparison of Current and Past Mixing Analysis Techniques

Moore et al. (1987) and MacIsaac et al. (2010) studied the freestream mixing loss development downstream of low speed linear turbine cascades. First, Moore et al. (1987) sought to determine the downstream axial total pressure gradient, $\partial P_t/\partial x$, based on measurements of the mean flow and turbulence fields. Those authors applied the RANS mean kinetic energy equation as given by Hinze (1975) as a basis for conducting their analysis. Hinze's (1975) equation is given as,

$$\frac{\partial}{\partial t}\left(\rho\frac{U_i U_i}{2}\right)+\frac{\partial}{\partial x_j}U_j\left(P_s+\rho\frac{U_i U_i}{2}\right)+\frac{\partial}{\partial x_j}\left(\rho\langle u_i u_j\rangle U_i\right)-\frac{\partial}{\partial x_j}\left(\mu U_i\left(\frac{\partial U_i}{\partial x_j}+\frac{\partial U_j}{\partial x_i}\right)\right)=$$
$$\rho\langle u_i u_j\rangle\frac{\partial U_i}{\partial x_j}-\mu\left(\frac{\partial U_i}{\partial x_j}+\frac{\partial U_j}{\partial x_i}\right)\frac{\partial U_i}{\partial x_j} \qquad \text{(A.1)}$$

As shown, total pressure is contained in the second term on the left hand side, a gradient of the product of velocity and total pressure. Moore et al. (1987) noted that the third and fourth terms on the left hand side were negligible upon integration. Assuming steady mean flow and applying non-dimensional variables, Moore et al. (1987) approximated the axial loss coefficient gradient as,

$$-\frac{\partial\overline{\overline{C_{Pt}}}}{\partial\left(X/C_{ax}\right)}\cong N\iint_A\rho\langle u_i u_j\rangle\frac{\partial U_i}{\partial x_j}dA-N\iint_A\mu\left(\frac{\partial U_i}{\partial x_j}+\frac{\partial U_j}{\partial x_i}\right)\frac{\partial U_i}{\partial x_j}dA, \qquad \text{(A.2)}$$

where $\overline{\overline{C_{Pt}}}$ is the area-averaged total pressure loss coefficient, N is a constant used for non-dimensionalizing the equation, and A represents the downstream measurement area. To isolate total pressure in Eq. (A.2), Moore et al. (1987) assumed the convection

velocity (U_j in the second term of the left hand side of Eq. (A.1)) to be constant. In fact, the convection velocity became part of the factor N. Since Moore et al. (1987) considered area averages, the assumption of constant U_j is believed to be reasonable. For investigating the local variation of loss production in complex three dimensional endwall flows, the assumption of constant U_j is less likely to be valid.

Moore et al. (1987) concluded that the total pressure gradient is mostly due to turbulence production, the first term on the right hand side of Eq. (A.2) (sometimes called the deformation work). Later, MacIsaac et al. (2010) investigated the local variation of turbulence production downstream of a low speed linear turbine cascade to indicate where losses were produced in the flow. Those authors noted that the production term can be either positive or negative, with negative values indicating a reduction of mean kinetic energy through growth of turbulent kinetic energy. The primary implication is that turbulence that is produced will later be dissipated, representing a loss. However, if the sign of the production term is such that the mean kinetic energy increases (turbulence decreases), it is unclear whether or not losses have been produced from the energy exchange. MacIsaac et al. (2010) showed that within the passage vortex of their cascade (Fig. 10 of their paper), the production term was positive indicating increasing mean kinetic energy. One might suspect loss production to be high within the passage vortex, yet the sign of the production term did not necessarily indicate loss production.

To avoid the ambiguities associated with the use of Eq. (A.1), I derived an alternative approach for studying mixing in Chapter 6. By manipulating the incompressible RANS momentum equation and assuming steady mean flow, the total pressure gradient can be written directly in non-dimensional variables as,

$$\frac{\partial P_t}{\partial x_i} = \frac{1}{Re}\frac{\partial^2 U_i}{\partial x_j \partial x_j} - \varepsilon_{ijk}\omega_j U_k - \left(\frac{2}{3}\frac{\partial k}{\partial x_j}\delta_{ij} + \frac{\partial a_{ij}}{\partial x_j}\right), \tag{6.10}$$

where the first term on the right hand side represents viscous diffusion of the mean flow field (an irreversible mean flow effect), the second term is a coriolis effect (a reversible mean flow effect), the third term containing k is the isotropic effect of turbulence (a reversible turbulence effect), and the final term represents turbulent shear (an irreversible turbulence effect). Section 6.2 explains the terms of Eq. (6.10) in more detail. Like Moore et al. (1987), Eq. (6.10) assumes steady flow, but no other terms are simplified (e.g., the assumed constant convection velocity U_j in the second term on the left hand side of Eq. (A.1) to derive Eq. (A.2)). Equation (6.10) can be evaluated locally in the flow at a point. Rather than turbulence production, the magnitudes of shear effects that change the mechanical energy of the flow are used to indicate where losses are produced. As shown in Chapter 6, turbulent shear predominantly drives the mixing process. The idea is to find where shear is strong in the flow, so contrary to MacIsaac et al. (2010), the sign of the shear terms does not matter in relation to loss production.

It is also worth noting that the derivation of Eq. (6.10) required use of the following vector identity (cf., Panton, 1996),

$$U_j \frac{\partial U_i}{\partial x_j} = \frac{\partial}{\partial x_i}\left(\frac{1}{2}U_j U_j\right) + \varepsilon_{ijk}\omega_j U_k . \tag{A.3}$$

In the following discussion I will provide proof of this identity due to its important role in the derivation of Eq. (6.10). For the term on the left hand side of Eq. (A.3), $\frac{\partial U_i}{\partial x_j}$ is the velocity gradient tensor. Reversing the i and j indices for convenience and recalling that

tensors can be written as the sum of their symmetric and antisymmetric parts, $\frac{\partial U_i}{\partial x_j}$ can be rewritten as,

$$\frac{\partial U_j}{\partial x_i} = \frac{1}{2}\left(\frac{\partial U_j}{\partial x_i} + \frac{\partial U_i}{\partial x_j}\right) + \frac{1}{2}\left(\frac{\partial U_j}{\partial x_i} - \frac{\partial U_i}{\partial x_j}\right). \tag{A.4}$$

Now consider that the dual vector of the velocity gradient tensor can be written as,

$$\omega_i = \varepsilon_{ijk}\frac{\partial U_k}{\partial x_j}. \tag{A.5}$$

The dual vector of the velocity gradient tensor is referred to as the vorticity. Noting that a tensor can be written as the sum of its symmetric part and dual vector, the velocity gradient tensor can be written as,

$$\frac{\partial U_j}{\partial x_i} = \frac{1}{2}\left(\frac{\partial U_j}{\partial x_i} + \frac{\partial U_i}{\partial x_j}\right) + \frac{1}{2}\varepsilon_{ijk}\omega_k. \tag{A.6}$$

Interchanging i and j again and multiplying Eq. (A.6) by U_j,

$$U_j\frac{\partial U_i}{\partial x_j} = \frac{1}{2}\left(U_j\frac{\partial U_j}{\partial x_i} + U_j\frac{\partial U_i}{\partial x_j}\right) - \frac{1}{2}\varepsilon_{ijk}\omega_k U_j. \tag{A.7}$$

Multiplying Eq. (A.7) by two and reversing the order of the cross product of vorticity and velocity, Eq. (A.7) reduces to,

$$U_j\frac{\partial U_i}{\partial x_j} = U_j\frac{\partial U_j}{\partial x_i} + \varepsilon_{ijk}\omega_j U_k. \tag{A.8}$$

Now observe by the product rule of calculus that,

$$\frac{\partial}{\partial x_i}\left(U_j U_j\right) = 2U_j\frac{\partial U_j}{\partial x_i}. \tag{A.9}$$

Equation (A.9) implies that,

$$U_j \frac{\partial U_j}{\partial x_i} = \frac{\partial}{\partial x_i}\left(\frac{1}{2} U_j U_j\right). \tag{A.10}$$

Substituting Eq. (A.10) into Eq. (A.8) we obtain,

$$U_j \frac{\partial U_i}{\partial x_j} = \frac{\partial}{\partial x_i}\left(\frac{1}{2} U_j U_j\right) + \varepsilon_{ijk}\omega_j U_k . \tag{A.3}$$

Appendix B: Summary of Endwall Loss Correlations from the Literature

In this Appendix I summarize the endwall loss correlations used for benchmarking in Chapter 5. Since cascade nomenclature sometimes varies between authors, for consistency I adapted the loss correlations in this appendix to use the cascade nomenclature shown in Fig. B.1.

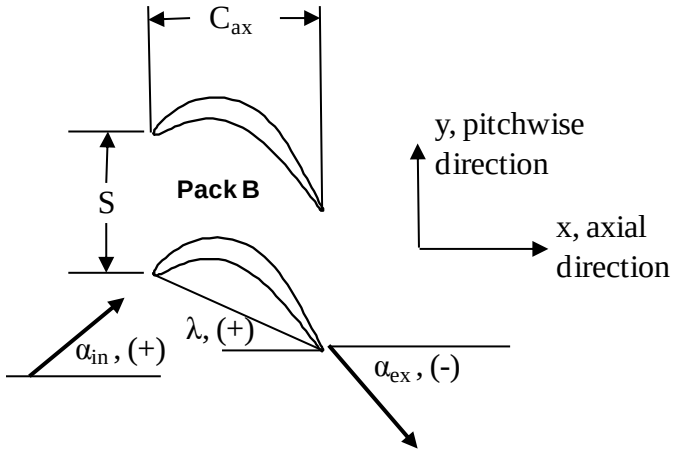

Fig. B.1 Cascade Definitions

In this appendix I focus on the design point correlations of Kacker and Okapuu (1982), Sharma and Butler (1987), and Benner et al. (2006b). The correlation of Kacker and Okapuu (1982) is an update of the work of Dunham and Came (1970), which in turn is an update of the original work of Ainley and Mathieson (1951). The two updates to the Ainley and Mathieson (1951) correlation reflected changes in performance of turbines that occurred over time. The Sharma and Butler (1987) correlation is derived from integral boundary layer methods and relies less on empiricism than the correlations based

on the work of Ainley and Mathieson (1951). The most recent correlation is due to Benner et al. (2006b), which represents an update to the work of Sharma and Butler (1987).

For the Kacker and Okapuu (1982) loss prediction system, passage losses are broken down according to,

$$Y_{ps} = Y_{2D} + Y_{ew}. \tag{B.1}$$

The endwall loss, Y_{ew}, is given as,

$$Y_{ew} = 0.0334 f(AR)\left(\frac{\cos\alpha_{ex}}{\cos\beta_{in}}\right)\left(\frac{C_L}{S/C}\right)^2 \frac{\cos^2\alpha_{ex}}{\cos^3\alpha_m}, \tag{B.2}$$

where,

$$\frac{C_L}{S/C} = 2(\tan\alpha_{in} - \tan\alpha_{ex})\cos\alpha_m, \tag{B.3}$$

$$\alpha_m = \tan^{-1}\left[\frac{1}{2}(\tan\alpha_{in} + \tan\alpha_{ex})\right], \tag{B.4}$$

$$f(AR) = \frac{1 - 0.25\sqrt{2 - H/C}}{H/C}, \qquad H/C \le 2 \tag{B.5}$$

$$= C/H, \qquad H/C > 2,$$

β_{in} is the blade inlet metal angle defined by the camber line, C is the true chord ($C \approx C_{ax}/\cos(\lambda)$), and AR is the aspect ratio. Note that for design incidence, $\beta_{in} \approx \alpha_{in}$. Additionally, Y_{ew} as defined in Eq. (B.2) represents the total pressure loss scaled by the exit dynamic head. To obtain the loss coefficient based on the inlet dynamic head one must multiply Eq. B.2 by $\cos^2\alpha_{in}/\cos^2\alpha_{ex}$.

Sharma and Butler (1987) define the breakdown of the passage loss the same as Kacker and Okapuu (1982) in Eq. (B.1). According to Sharma and Butler (1987) Y_{ew} is defined as,

$$Y_{ew} = Y_{2D}\frac{S\sin(90-\alpha_{ex})-TET}{H}\left(1+4\frac{\varphi}{\sqrt{CR}}\right), \tag{B.6}$$

where S is the pitchwise spacing between airfoils, TET is the trailing edge thickness, H is the airfoil height or span, φ is the total gas turning in radians, and CR is the cascade convergence ratio ($\rho_{ex}U_{ex}/\rho_{in}U_{in}$). Since Y_{ew} in Eq. (B.6) is proportional to Y_{2D}, determining whether Y_{ew} is based on inlet or exit conditions depends on how Y_{2D} is defined.

In their two part paper, Benner et al. (2006a, 2006b) defined a different loss breakdown scheme for describing the overall passage loss compared to the previous authors. Their new loss breakdown scheme is given as,

$$Y_{ps} = Y_{2D}\left(1-\frac{Z_{TE}}{H}\right)+Y_{ew}, \tag{B.7}$$

where Z_{TE} is the penetration height of the endwall flow along the span of the airfoil suction surface and H is the span. The premise of this loss breakdown scheme is that Y_{2D} dominates the passage loss for long blades whereas Y_{ew} dominates for short blades. Benner et al. (2006a) gives the correlation for Z_{TE}/H as,

$$\frac{Z_{TE}}{H} = \frac{0.10F_t^{0.79}}{\sqrt{CR}\left(\frac{H}{C}\right)^{0.55}}+32.70\left(\frac{\delta^*}{H}\right)^2, \tag{B.8}$$

where,

$$F_t = 2\left(\frac{S}{C_{ax}}\right)\cos^2\alpha_m\left(\tan\alpha_{in} - \tan\alpha_{ex}\right), \tag{B.9}$$

CR is the cascade convergence ratio defined above, α_m is given in Eq. (B.4), and δ^* is the inlet boundary layer displacement thickness. Benner et al. (2006b) gives a pair of correlations for Y_{ew} depending on the cascade aspect ratio,

$$Y_{ew} = \frac{0.038 + 0.41\tanh\left(1.20\delta^*/H\right)}{\sqrt{\cos\lambda}\left(CR\right)\left(H/C\right)\left(\frac{C\cos\alpha_{ex}}{C_{ax}}\right)^{0.55}} \qquad \text{for } H/C \le 2.0 \tag{B.10}$$

and,

$$Y_{ew} = \frac{0.052 + 0.56\tanh\left(1.20\delta^*/H\right)}{\sqrt{\cos\lambda}\left(CR\right)\left(H/C\right)\left(\frac{C\cos\alpha_{ex}}{C_{ax}}\right)^{0.55}} \qquad \text{for } H/C > 2.0. \tag{B.11}$$

The correlations for Y_{ew} in Eqs. (B.10) and (B.11) give the total pressure loss due to the presence of the endwall flow scaled by the exit dynamic head. To obtain the loss coefficient based on the inlet dynamic head one must multiply Eqs. (B.10) and (B.11) by $\cos^2\alpha_{in}/\cos^2\alpha_{ex}$.

Although the focus of this appendix is on endwall loss correlations, some clarification is required should an interested reader wish to use these equations to estimate the overall passage loss. In the development of all three correlations considered, Y_{ps} is a combination of Y_{ew} and the profile loss, Y_{2D}. Y_{2D} is defined as the profile loss that occurs without the influence of the endwall flow. To predict the overall passage loss, one can simply use available correlations from the literature (e.g., Wilson and Korakianitis (1998) or Kacker and Okapuu (1982)) to estimate Y_{2D}.

Appendix C: Experimental Setup for L2A and L2F Profile Loss Measurements

In this appendix I briefly describe the AFRL low speed wind tunnel test section when used for capturing profile loss data. A schematic of the test section is shown in Fig. C.1. As shown the cascade is comprised of seven airfoils. The end-flow adjusters were used to control the bypass flow around the outside of the cascade to achieve periodicity. A single outer tailboard was used to set the exit angle at Re = 100,000. It is understood that the exit angle will change as Re decreases approaching stall. Exit traverse data were collected at midspan, $0.75C_{ax}$ downstream of the cascade in the axial direction. The traverse origin is defined downstream of the middle blade as the intersection of the tangent line projected from the pressure side of the trailing edge, and the traverse plane. The tangent line projected from the pressure side of the trailing edge originates from the intersection of the trailing edge circle and the pressure surface. The same cascade definitions are used for both airfoils in the present study, L2A and L2F.

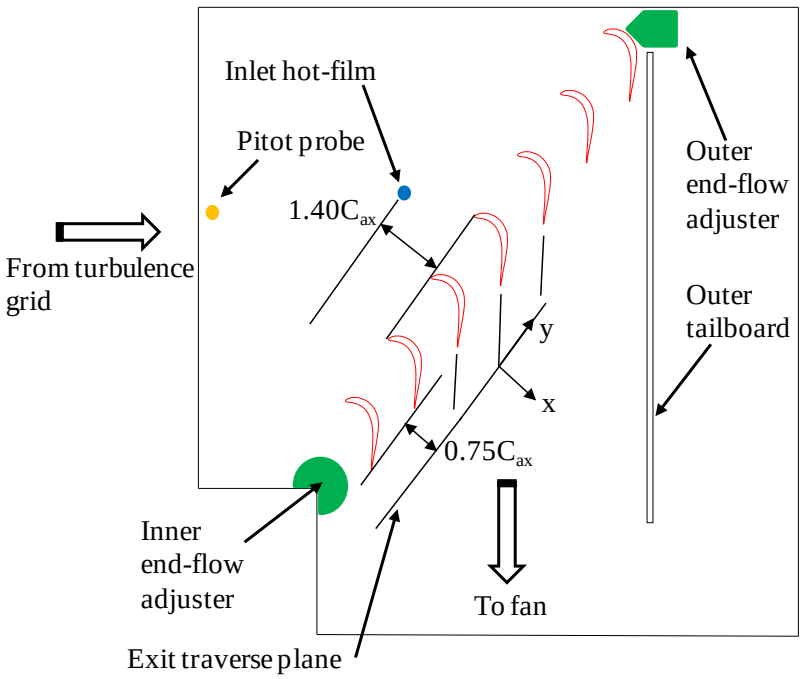

Fig. C.1 Schematic of the AFRL low speed wind tunnel test section when used for capture profile loss data

Table C.1 summarizes the relevant geometric data and flow conditions. The flow angles and resulting Zweifel number are approximate design point values for the L2A and L2F profiles. The cascade aspect ratio, H/C_{ax}, is also quite high to reduce the influence of endwall effects when taking measurements at midspan.

Table C.1 Cascade geometry and flow conditions for profile loss measurements

Axial chord, C_{ax}	152.4 mm
Pitch/axial chord, P/C_{ax}	1.221
Span/axial chord, H/C_{ax}	5.75
Zweifel coefficient, Z_w	≈ 1.59
Inlet flow angle, α_{in}	35˚
Exit flow angle, α_{ex}	≈ 58˚
Inlet turbulence Intensity, $Tu_{in,st}$	3.1%
Streamwise integral scale at inlet, $L_{in,st}$	39.2 mm
Max exit Mach number, M_{ex}	0.053

An upstream stationary pitot probe and a kiel probe in the exit traverse plane were used to measure total pressure loss. At 3.2 mm, the kiel probe diameter was less than 2% of the blade pitch, providing sufficient resolution within the wakes. I used a Druck LPM 5481 pressure transducer that was calibrated using a Ruska 7250LP laboratory standard (the reported accuracy is within 0.16% and 2.4% of the inlet dynamic head at Re = 100k and 20k, respectively) to measure total pressure differences across the blade row. The ambient pressure was measured with a laboratory barometer and freestream fluid temperatures were measured using type J thermocouples. An IFA300 constant temperature anemometer was used with single normal hot-film probes (TSI 1210-20, and 1211-20) for obtaining velocities, turbulence intensities, and integral length scales at the inlet and exit traverse.

Measurements of Y used for calculating the Reynolds lapse of L2A in Fig. 3.4 is shown in Fig. C.2. At high Re, the wind tunnel produces reasonably periodic wakes. As Re decreases, however, the flow separates on the suction surface of L2A causing a change in turning angle as made evident by the wakes moving to the right with decreasing Re. As a result, the wakes of the airfoils closer to the outer tailboard will be suppressed due to the tailboard forcing the flow to turn, thus reducing the periodicity across the wakes. Other workers studying linear cascades of LPT profiles at low Re, such as Ibrahim et al. (2008), have shown the same problem of poor periodicity with decreasing Re. Although it may be tempting to adjust the tailboards and bleeds to achieve periodicity for all Re, an exit angle will have to be assumed that may in fact be incorrect for the cascade. The resulting forced turning angle will influence the measured losses. The primary use of data such as those shown in Fig. C.2 is to estimate Re when

stall occurs, and thus enable comparisons in loss and stall performance between different profiles. For tests at low Re with the cascade in a stalled condition, replicating results between different wind tunnels will be difficult.

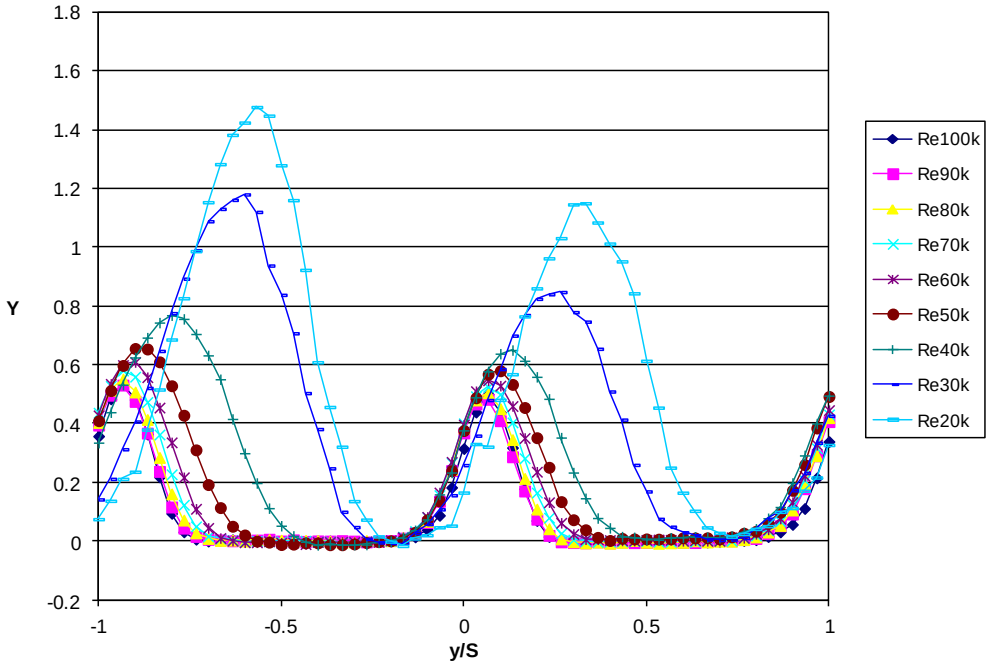

Fig. C.2 Loss data used to compute the Reynolds lapse of the L2A profile

As for calculating the overall profile loss coefficient, Y_{2D}, I integrated Y across the middle wake in the range of $-0.5 \leq y/S \leq 0.5$ to obtain area-weighted averages. At Re = 100,000, a case that included exit velocity data, I found that Y_{2D} based on a mass-weighted average is within about 3 to 4% of the area-weighted average, with the mass-weighted average being the smaller of the two. Since the wakes are fairly well mixed $0.75C_{ax}$ downstream of the blade row, differences in Y_{2D} due to area and mass-averaging are expected to be small.

Measurements of Y used for calculating the Reynolds lapse of L2F in Fig. 4.4 is shown in Fig. C.3. As shown, the L2F profile produces much lower profile losses than L2A in Fig. C.2. In addition because flow separation does not occur for the range of Re tested, the wakes remain reasonably periodic for all cases.

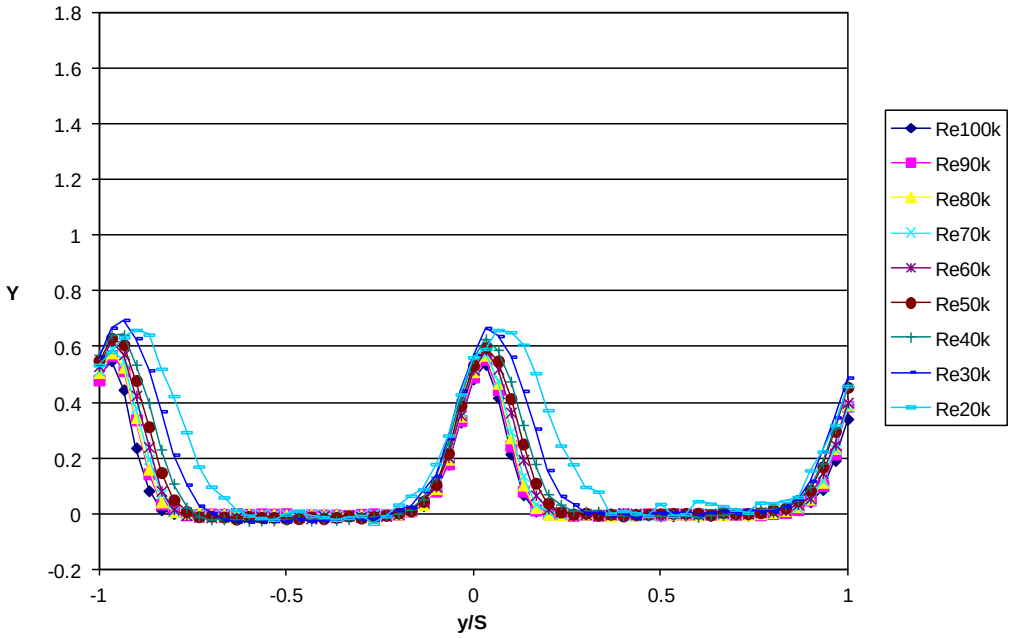

Fig. C.3 Loss data used to compute the Reynolds lapse of the L2F profile

Appendix D: Description of the Splitter Plate Modification for the AFRL Low Speed Wind Tunnel

In this appendix I describe the design of the splitter plate modification for the AFRL low speed wind tunnel. The splitter plate was used to provide a controlled inlet boundary layer for endwall measurements with the option of studying the effects of boundary layer thickness and passing wakes. I also discuss the cascade inlet conditions in this appendix.

D.1 Splitter Plate Design

The top view of the splitter plate is shown in Fig. D.1. The splitter plate assembly fits around the airfoils that are fastened to the floor and ceiling of the tunnel. Segments are used between the airfoils, with slots cut out in between for the airfoils to pass through. The segments are custom machined from 1.27 cm (1/2 in) thick polycarbonate sheeting for both profiles, L2A and L2F. The inlet and exit guide rails shown in Fig. D.1, machined from 6061 T6 Al, hold the segments in place. The combined developing plate and leading edge extend approximately $4.5C_{ax}$ upstream in the streamwise direction, whereas the exit plate extends $4C_{ax}$ downstream in the streamwise direction. The developing plates and leading edge are also machined from 1.27 cm (1/2 in) thick polycarbonate sheeting. Supports around the perimeter of the splitter assembly and underneath the guide rails hold it at the desired spanwise location along the airfoils, creating an effective span to axial chord ratio of 3.5. Measurements are acquired between the splitter plate and tunnel roof. A three-dimensional view of the splitter assembly is

shown in Fig. D.2 to better orient the reader to how the assembly appears when installed in the wind tunnel.

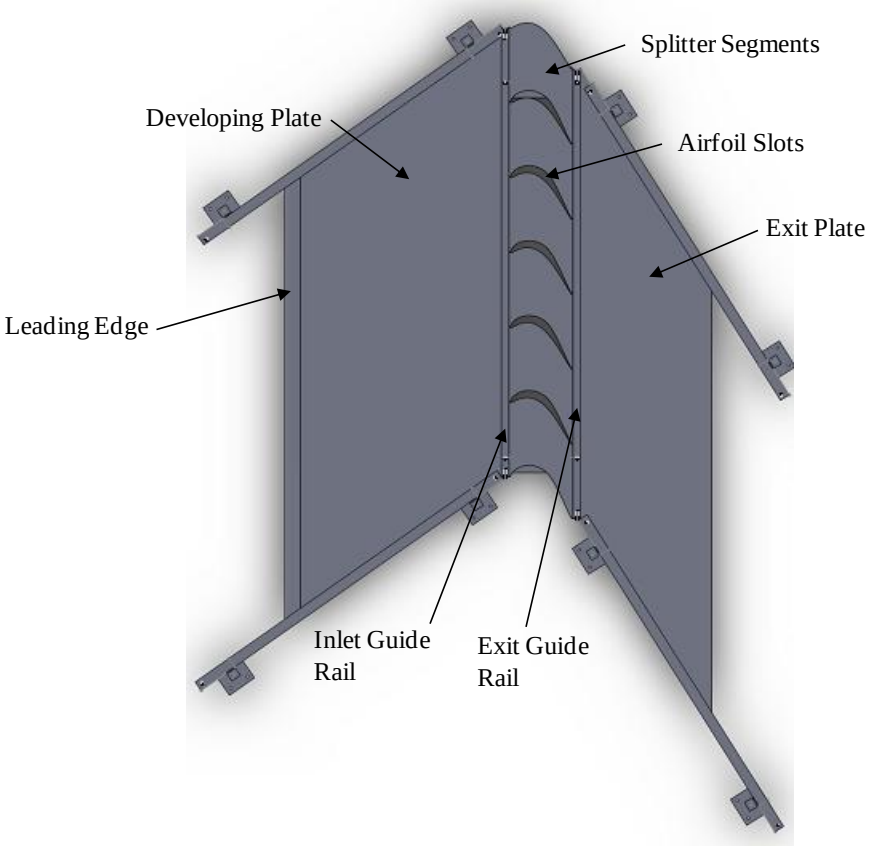

Fig. D.1 Top view of the splitter plate modification

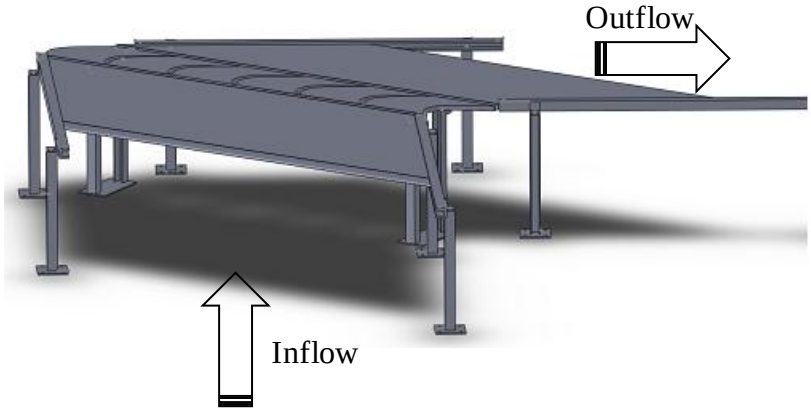

Fig. D.2 Three-dimensional view of the splitter plate assembly

The choice of spanwise location to place the splitter plate assembly depended on a tradeoff between two sources of asymmetry: the unequal boundary layer thickness on the splitter plate and tunnel roof; and the balance in pressure drop between the top and bottom sides of the splitter plate. Figure D.3 is shown to visualize these sources of asymmetry. First consider a case where the splitter plate is at the center of the airfoil. In this case one can expect the pressure drop across the blade row to be nearly equal above and below the splitter plate, thus preserving uniform inlet conditions to the cascade. The resulting measurement passage will still, however, have a thicker boundary layer on the tunnel roof than on the splitter plate. Therefore, it is desirable that the distance between the tunnel roof and splitter plate be large to allow opposing endwall flows to develop independently. As a tradeoff I set the top of the splitter plate approximately at 39% span from the tunnel floor. As mentioned above, the effective span to axial chord ratio of the measurement passage is 3.5.

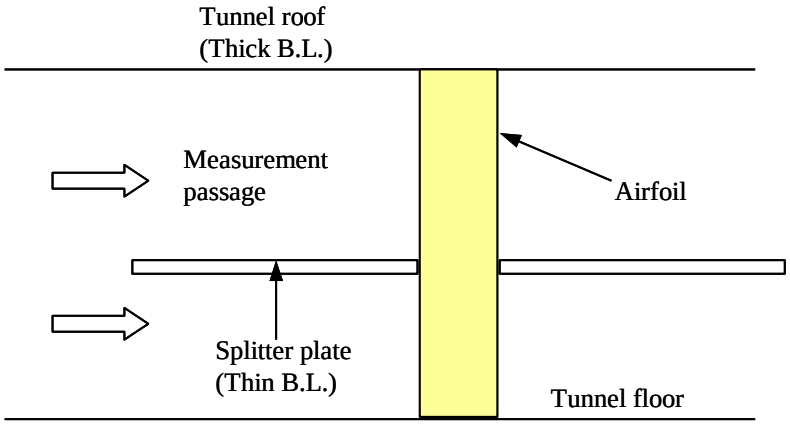

Fig. D.3. Diagram of possible sources of flow asymmetry using the splitter plate

The streamwise length of the developing plate determines the cascade inlet boundary layer thickness. Therefore to accommodate inlet boundary layer thickness

control, the leading edge was designed and built separately to attach to any length of developing plate using a tongue and groove joint. The leading edge shape was defined as a cubic super-ellipse,

$$\left[(1.5-x)/1.5\right]^3+\left(y/0.25\right)^3=1, \qquad \text{(D.1)}$$

where x and y are in inches. The leading edge shape is plotted in Fig. D.4 as it appears normal to the leading edge, and also aligned with the incoming velocity vector. Narasimha and Prasad (1994) recommended this leading edge shape to provide incidence tolerance by preventing a separation bubble from forming at the leading edge/developing plate junction.

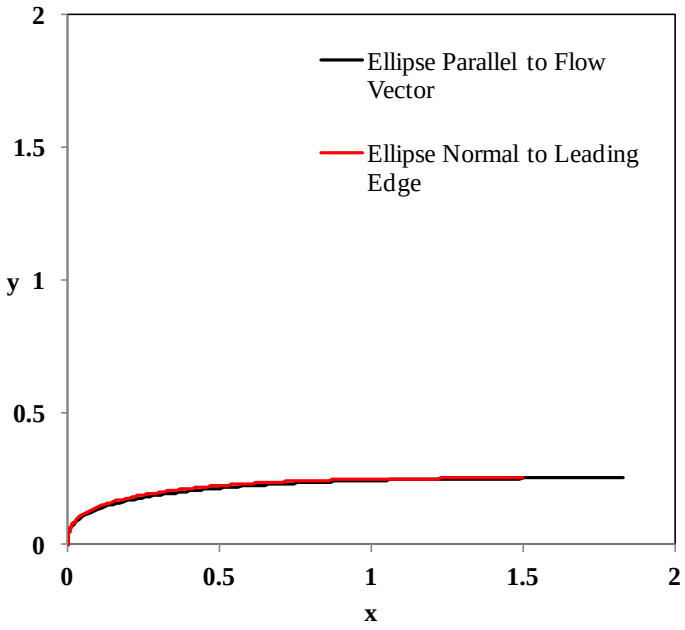

Fig. D.4 Plot of the splitter assembly leading edge shape

The splitter plate assembly was designed using supporting legs rather than extending from wall to wall in the wind tunnel to accommodate an existing wake generator. The wake generator conveys thin cylinders around the outer wall of the wind tunnel and directly in front of the cascade. The cylinders simulate wakes from an

upstream blade row. The developing plate section was designed to be freestanding apart from the inlet guide rail to leave a gap for passing cylinders in wake studies. Note that in the current study I did not consider the effect of passing wakes and the wake generator was not in the tunnel for any of the experiments. Accordingly, the developing plate and inlet guide rails were flush mounted with a tongue and groove joint to run without a gap at the inlet.

In summary, the splitter plate assembly was designed to be flexible and accommodate different kinds of experiments. As one might expect, the addition of the splitter plate introduced some non-uniformity at the cascade inlet. As will be shown, however, the non-uniformity is reasonably small and I show a procedure for zeroing out bias errors in total pressure loss due to that non-uniformity.

D.2 Cascade Inlet Conditions

I acquired velocity, turbulence and total pressure measurements $1.4C_{ax}$ upstream of the blade row in the axial direction to characterize the cascade inlet conditions. Fig. D.5 shows the traverse plane relative to the blade row. As shown, the origin of the inlet traverse plane is upstream of the center airfoil leading edge. I used a pair of pitot-static probes, indicated by the blue dots, to simultaneously measure the inlet velocity at separate locations to determine how to set the outer end-flow adjuster and achieve a reasonably periodic inlet flow. The inlet pitot-static probes were at z/H = 0.20 inside the measurement passage and were fixed to the splitter plate. For inlet velocity and turbulence measurements I used a single-normal hot-film probe to traverse the inlet boundary layer and also the freestream at several spanwise locations. I measured the total pressure variation with a kiel probe.

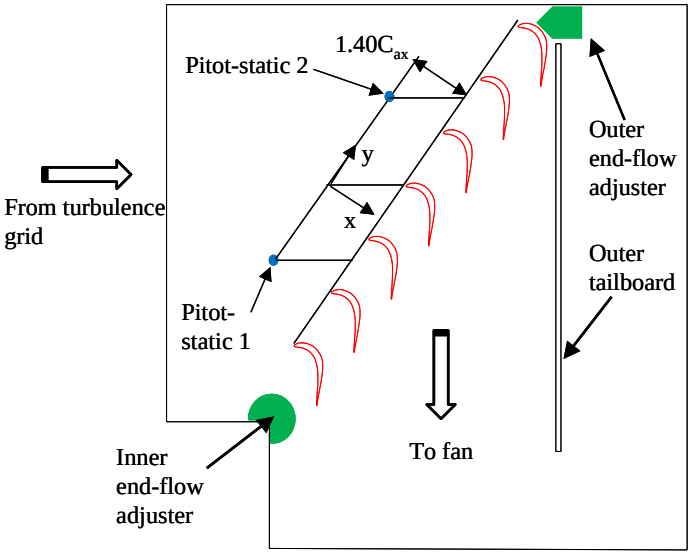

Fig. D.5. Schematic of the test section showing the inlet traverse plane

Figure D.6 shows the inlet freestream velocity at several spanwise locations, ranging from z/H = 0.10 to z/H = 0.40. I chose to take measurements out to z/H = 0.40 because downstream of the blade row, that spanwise location is sufficiently far from the endwall (splitter plate) to capture all significant endwall effects. The measurements are for Re = 100,000. Figure D.6a shows the inlet velocity in dimensional variables. In Fig. D.6b the velocity measurements are normalized by the average freestream velocity to show the variation. As shown, the velocity is within 2% of the average over most of the measurement area. The worst non-uniformity shown is near z/H = 0.40 and y/S = -0.45, yet the velocity is still within 3% of the average.

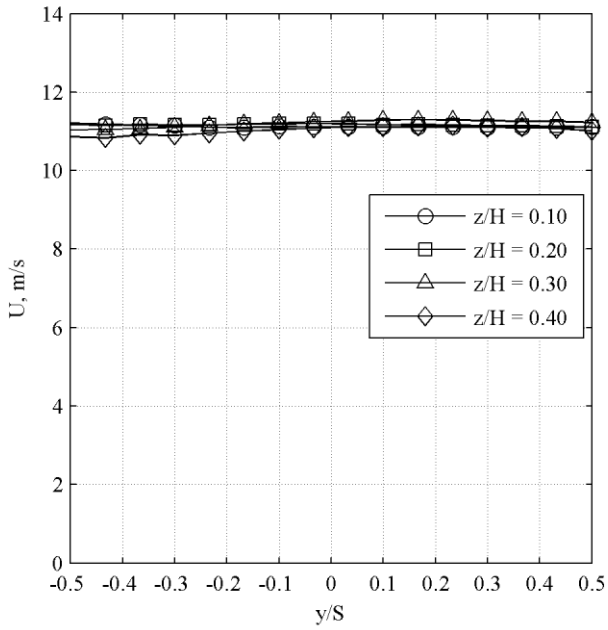

a) Dimensional velocity variation

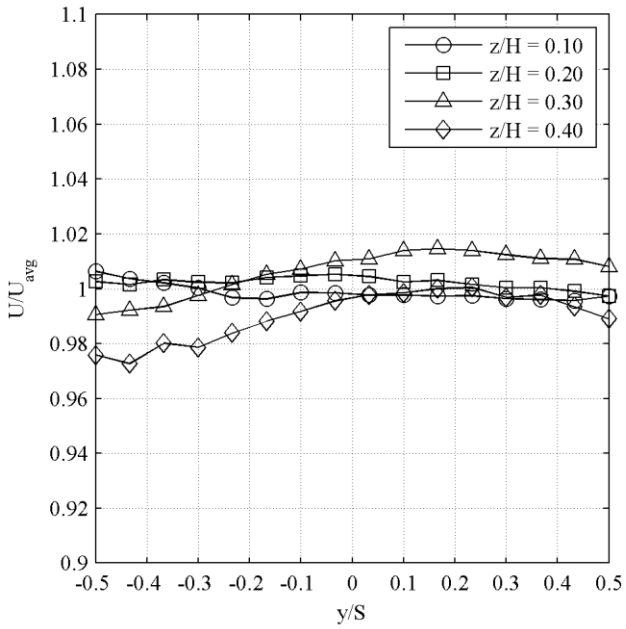

b) Normalized velocity variation

Fig. D.6 Cascade inlet velocity

The total pressure at the cascade inlet is shown in Fig. D.7. Loss coefficients, Y, are used to show the total pressure variation. Y is defined as the difference between the total pressure of pitot-static probe 1 in Fig. D.5 and the traversing kiel probe, normalized

by the dynamic head of pitot-static probe 1. I chose the Y scale in Fig. D.7 to be consistent with the peak levels of Y that occur in the endwall wake, approximately 0.85 and 0.90 for L2F and L2A, respectively. Compared to the peak levels of Y in the endwall wake, the variation in total pressure is small. The worst total pressure non-uniformity shown occurs at z/H = 0.40 and y/S = -0.5, consistent with the inlet velocity variation in Fig. D.6. Although the non-uniformity is small compared to peak Y values of the whole wake, the non-uniformity at z/H = 0.40 is approximately 10% of the peak loss downstream of the blade row at z/H = 0.40. Therefore, correcting for inlet non-uniformity seems warranted to avoid a bias error when calculating Y downstream of the blade row.

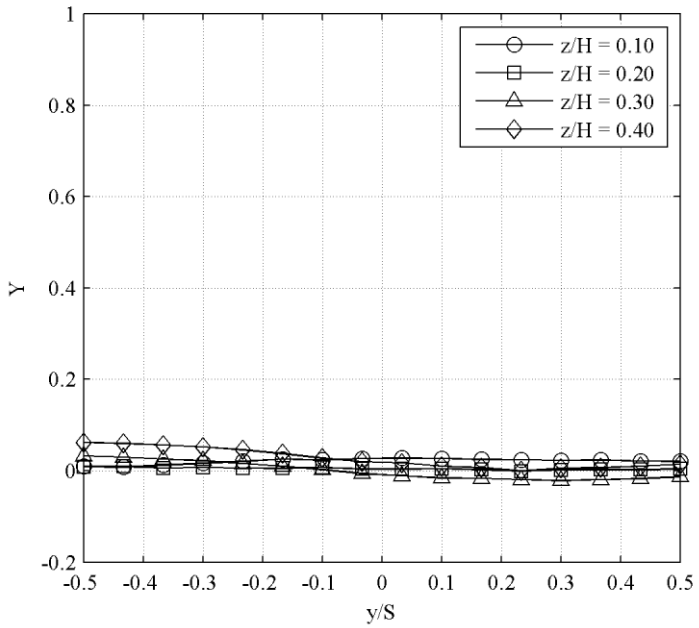

Fig. D.7 Cascade inlet total pressure

I corrected for inlet non-uniformity by using Matlab (surface fit tool of the curve fitting toolbox) to calculate a least squares surface fit of the measured loss data outside of the wake between z/H = 0.10 and z/H = 0.40. Outside of the wake we expect Y = 0.

Between z/H = 0.10 and z/H = 0 at the endwall, wake effects occur over most of the pitch so I did not apply the correction in this region. The surface fit provided an estimate of the bias error across the measurement area that I subtracted from the original measurements. I used this correction method for both the L2A and L2F profiles.

Figure D.8 shows Y contours for L2F over the whole measurement area downstream of the blade row before and after correcting for inlet non-uniformity. The measurements were captured in the measurement plane of Fig. 4.2. As shown, the Y = 0.05 contour line on the left of the wake in Fig. D.8a is evidence of the inlet non-uniformity. The contour lines indicate that Y increases slightly approaching midspan on the left side of the wake. As shown in Fig. D.8b, the correction results in nearly parallel contour lines approaching midspan where the flow is predominantly two-dimensional. Midwake across the pitch, the correction does not significantly influence peak Y levels.

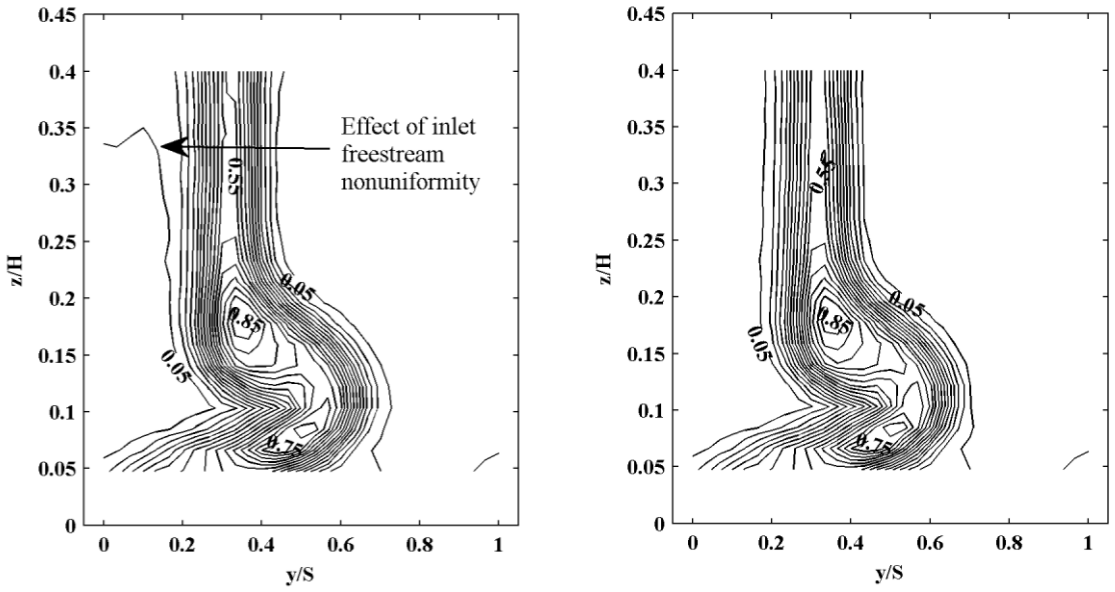

a) Before correction b) After Correction

Fig. D.8 Y contours of the L2F wake before and after correcting for inlet non-uniformity (ΔY = 0.05 between contour lines)

Having discussed the freestream inlet velocity and total pressure, Fig. D.9 shows inlet boundary layer traverses at y/S = -1, 0 and +1. As shown, the 99% boundary layer thickness is approximately $\delta_{99}/H = 0.025$. The boundary layer thickness seems small, but the passage has an aspect ratio of $H/C_{ax} = 3.5$. Relative to the profile geometry, the 99% boundary layer thickness is approximately $\delta_{99}/C_{ax} = 0.088$. The average ratio of displacement to momentum thickness, referred to as the shape factor, is approximately 2.2. This shape factor falls in between the values for fully laminar and turbulent boundary layers, 2.6 and 1.3, respectively (cf., Pope, 2000). Therefore, the inlet boundary layer may actually be transitional at the inlet traverse plane. I am not attributing special significance to the state of the inlet boundary layer. Rather, I am reporting this information so another researcher can put their work in context with the current work.

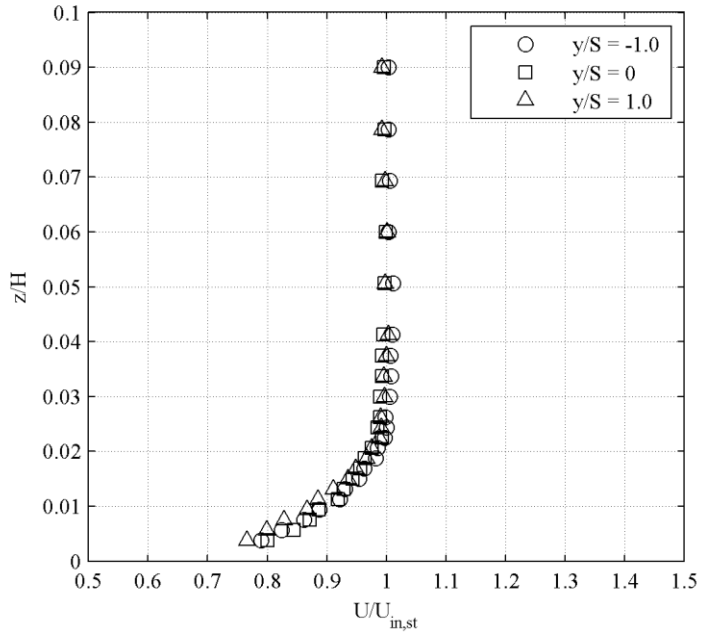

Fig. D.9 Inlet boundary layer traverses at three pitchwise positions

Turning now to the freestream turbulence entering the cascade, Figs. D.10 and D.11 show the inlet turbulence intensity and approximate integral length scale, respectively. The overall average turbulence intensity at the inlet is approximately 3.0%. I acquired the length scale data of Fig. D.11 at z/H = 0.20. The average integral length scale is approximately 39.4 mm, or $0.26C_{ax}$.

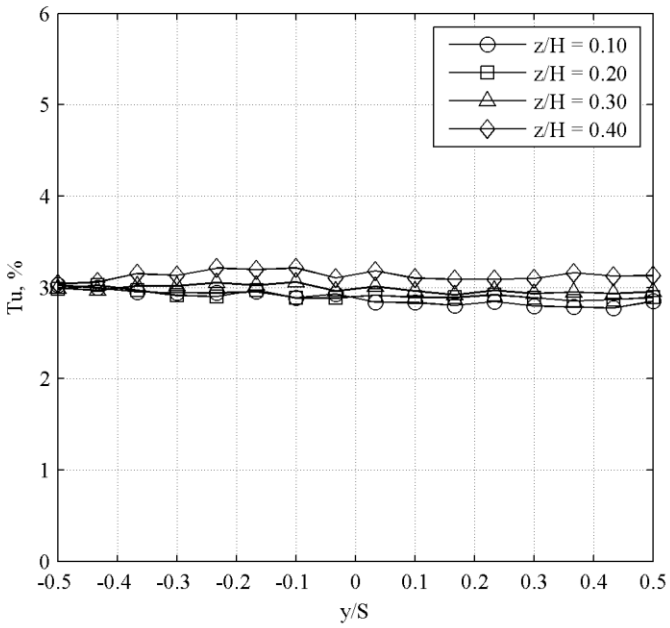

Fig. D.10 Cascade inlet turbulence intensity

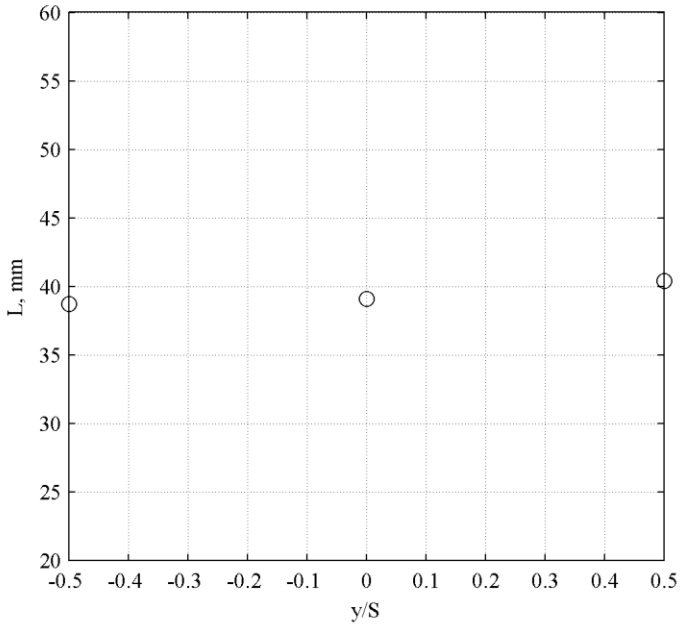

Fig. D.11 Measurements of the inlet integral length scale at z/H = 0.20

Appendix E: In-line Kiel Probe Design and Angle Sensitivity Test Results

In the current study I used a custom in-line kiel probe for sensing total pressure downstream of the blade row. Dr. Rolf Sondergaard of AFRL/RQTT designed the probe and the AFIT model shop fabricated it. The need for an in-line kiel probe stemmed from the need to traverse in three dimensions inside the wind tunnel. Conventional kiel probes are designed to pass through slots in wind tunnels to access the flow. The AFRL low speed wind tunnel only has two access slots downstream of the blade row oriented in the cascade pitchwise direction, thereby limiting movement in the axial direction. The solution was to mount a small traverse inside the wind tunnel to enable traversing in the axial direction. A large traverse mounted outside the tunnel was used to move the small traverse inside the tunnel in the pitchwise and spanwise directions, thus enabling three-dimensional freedom of movement inside the tunnel. Figure E.1 depicts the traverse orientations relative to the blade row.

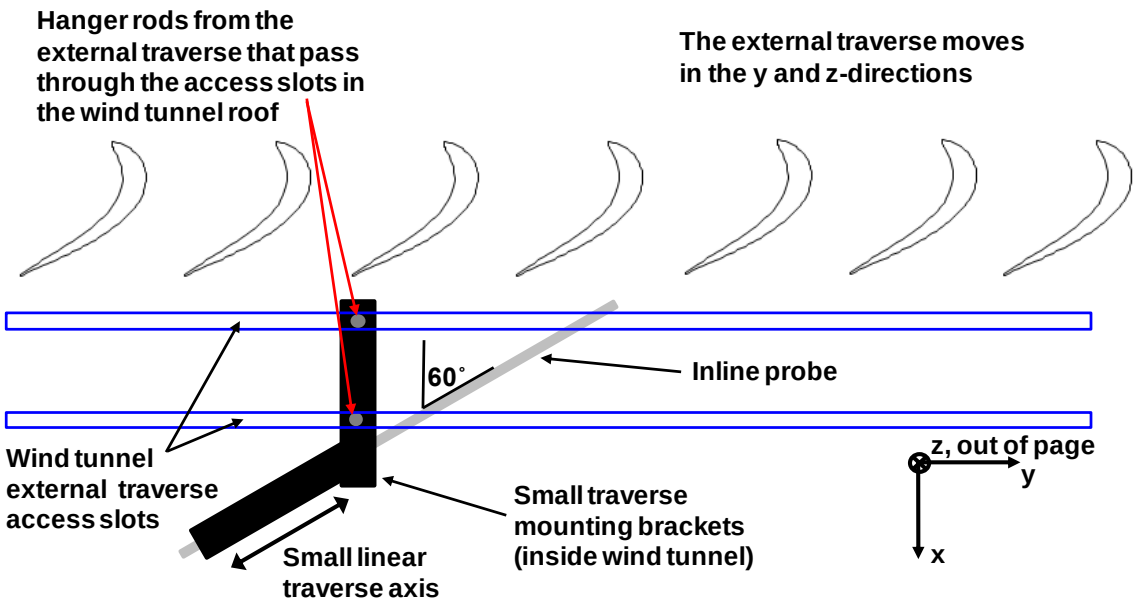

Fig. E.1 Traverse arrangement to enable 3D movement inside the wind tunnel

Three-dimensional freedom of movement was primarily needed for the triple-sensor hot-film measurements that were used for the mixing calculations of Chapter 6. For consistency between the hot-film and total pressure measurements we chose to design and fabricate the in-line kiel probe so that it could be mounted to the same traversing hardware as the triple-sensor hot-film probe. Using the in-line kiel probe I was able to acquire total pressure downstream of the blade row in the same planes used for velocity and turbulence measurements.

A diagram of the in-line kiel probe is shown in Fig. E.2, the design of which was inspired by the X-31 aircraft kiel probe (NASA, 2002), not of typical laboratory probes. The probe was designed with concentric tubes. The outer tube was machined near the inlet to form a bell mouth contraction, typical of conventional kiel probes. The leading edge of the inner tube was placed at the throat of the bell mouth inlet. The inner tube is the sensing port of the probe. The plug was used to both seal the gap between the inner and outer tubes and also keep the inner tube centered inside the outer tube. Slots were cut in the outer tube to allow the flow surrounding the inner tube to exhaust to the freestream, consistent with conventional kiel probes. Fig. E.3 shows a picture of one of the in-line kiel probes the AFIT model shop fabricated to get a sense of scale. As shown, the outer tube has a 1/8 in = 3.2 mm outer diameter. The overall length is 18 in = 45.7 cm.

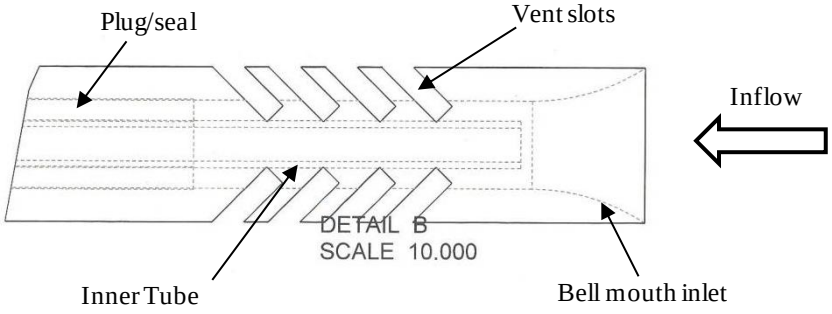

Fig. E.2 Diagram of in-line kiel probe

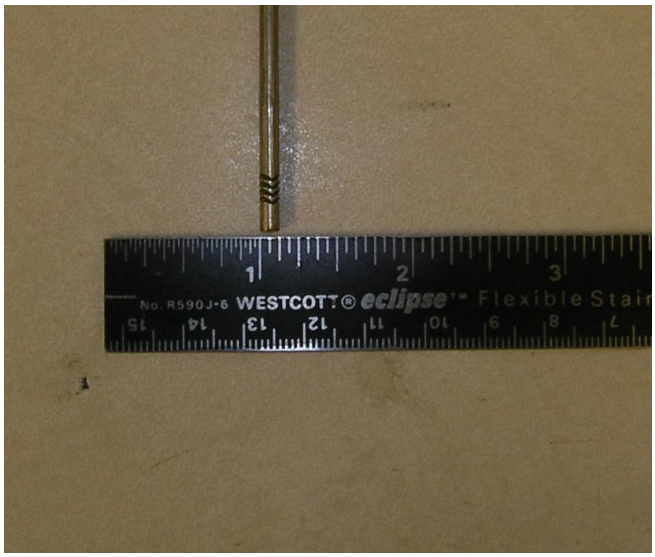

Fig. E.3 Picture of an in-line kiel probe to show the scale

The primary reason for using kiel probes to sense total pressure is that they are insensitive to the flow angle, typically out to 40˚ or more. I used a TSI Model 1127 hot-wire velocity calibrator to verify that the new in-line kiel probe design is also insensitive to the flow angle. The velocity calibrator was used to orient the probe head at a known angle relative to an air jet. I varied the flow angle in the range of -30˚ to +30˚ for three separate roll angles about the axis of the probe, spaced 120˚ apart. A 30˚ flow angle is the maximum that can be obtained with the velocity calibrator. Based on triple-sensor hot-film measurements, flow angles in the experiment relative to the probe were typically within 10˚. Therefore, checking the angle sensitivity out to 30˚ should be sufficient. Finally, I used a 10 m/s jet to correspond to the cascade inlet velocity for Re = 100,000. Depending on the season, the cascade inlet velocity varies between 10 and 11 m/s.

The results of the angle sensitivity tests are shown in Fig. E.4 where the error is defined as,

$$\text{Error}(\%) = \frac{P_{t,\text{kiel}} - P_{t,\text{calibrator}}}{P_{dyn,jet}} \times 100\% . \qquad \text{(E.1)}$$

The error is expressed as a fraction of the jet dynamic head to give insight into possible errors in loss coefficient that is based on the cascade inlet dynamic head. As shown in Fig. E.4, the worst case error is less than 0.15%. Therefore, the new in-line kiel probe appears to be reasonably insensitive to the flow angle, at least for the range of flow angles in this study.

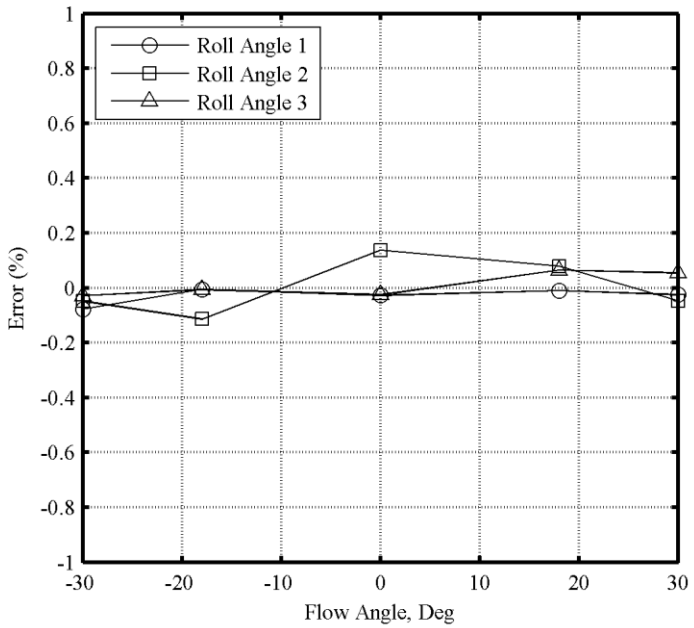

Fig. E.4. Angle sensitivity results of the new in-line kiel probe

Appendix F: Thermal Anemometry

In this appendix I describe how I set up and used hot-film probes for obtaining velocity and turbulence data. Anemometry using hot-wires and hot-films is a mature technology, so the focus of this discussion will be on the practical aspects of taking the measurements. I first discuss calibration and use of single-normal probes (TSI Model 1210-20 or 1211-20) followed by the data reduction methodology for a triple-sensor hot-film probe (TSI Model 1299-18-20). Finally I discuss methods used for calculating turbulent properties such as turbulence intensity, time and length scales as well as Reynolds stresses.

F.1 Use of a Single-Normal Probe

A TSI Inc. IFA300 constant temperature anemometer was used for all hot-film measurements. The hot-film sensor forms one leg of a Wheatstone bridge circuit. In constant temperature mode, the bridge circuit is usually balanced with the film temperature approximately at 250˚C. Other operating temperatures can be used but 250˚C appears to be standard for air. As the velocity of the flow passing over the sensor changes, the resulting change in heat transfer from the wire will cause the sensor to either cool or heat up, unbalancing the bridge. The unbalanced bridge voltage produces a feedback current signal that rebalances the bridge, holding the temperature constant. Depending on the sensor being used, the bridge circuit can operate with a frequency response exceeding 200 kHz, making such an instrument ideal for time-resolved measurements of turbulent flows.

The IFA300 was controlled using in-house codes written with National Instruments Labview software. Figure F.1 shows the front panel of the virtual instrument (VI) used for controlling the IFA300. The buttons on the front panel show the commands that are used for setting up and operating probes. In the following discussion I describe the command sequence.

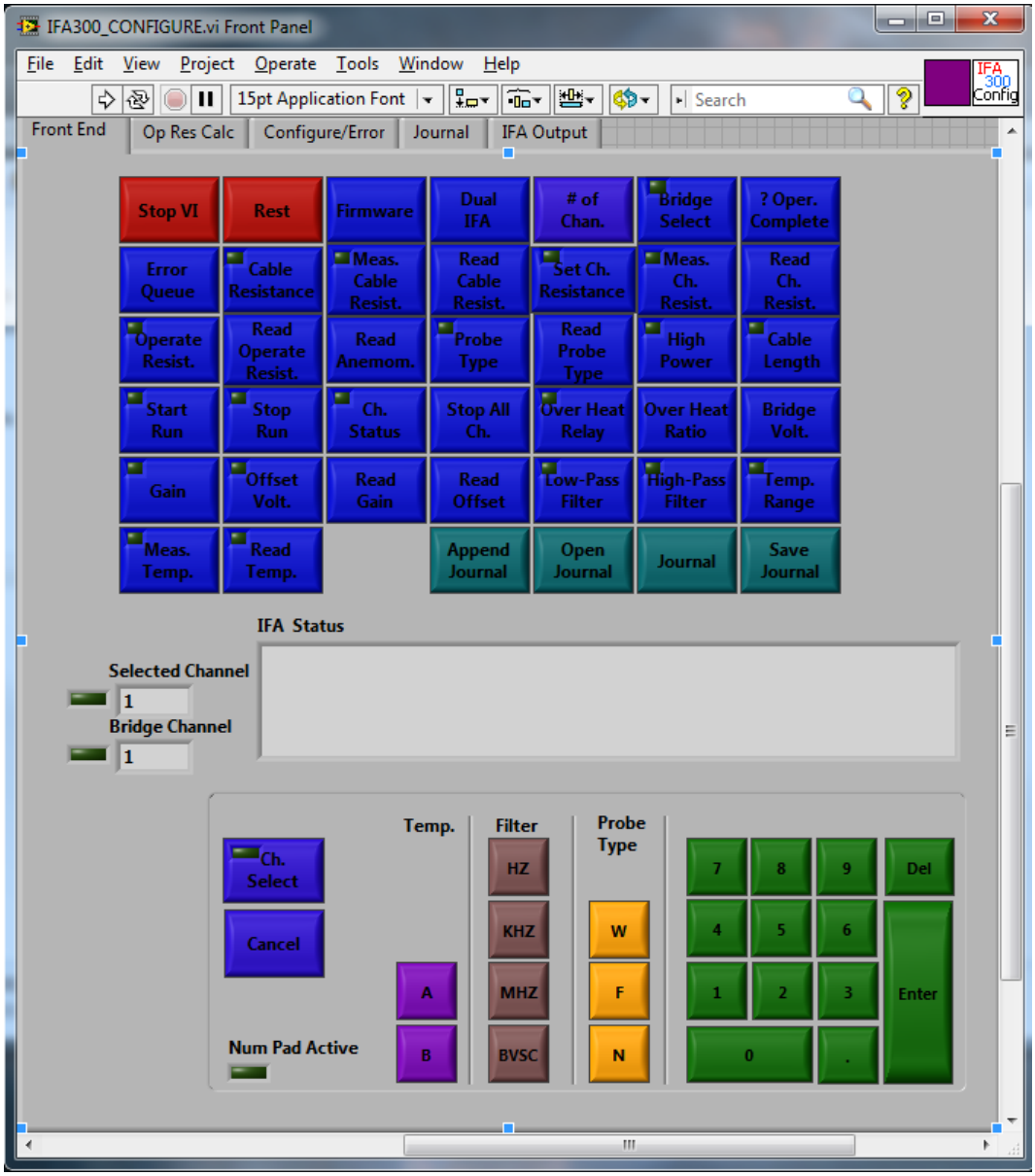

Fig. F.1 Front panel of the Labview VI used for controlling the IFA300

Before using a probe, the first step is to measure the cable resistance. The IFA300 has an ohmmeter and a cable resistance measurement command is available. The cable resistance usually contributes to about 3% of the total resistance (0.3 Ω) in the sensing leg of the bridge circuit when the probe is in run mode. A shorting plug is used in place of the probe when checking the cable resistance. Using the shorting plug is vitally important and a user should be sure to never activate the "measure cable resistance" command with a sensor plugged into the cable instead of the shorting plug. One of my student colleagues from Ohio State University once made this mistake and said that the probe lit up like a light bulb filament. Consequently the probe never worked properly after that.

The next step is to measure the channel resistance. (Note that the IFA300 has eight channels to support eight simultaneous hot-wire or hot-film measurements.) For this step the probe should be plugged into the cable. A typical channel resistance is about 6.4 Ω and represents the resistance of a probe when the sensor is at ambient, or room temperature prior to activating the run mode. This setting is particularly important when the lab temperature changes significantly between tests. Ideally the room would be air conditioned to maintain stable air temperatures. When weather fronts pass through overnight, however, the temperature of the room containing the AFRL low speed wind tunnel may drop 8˚C or more from evening to the next morning, thus requiring that the bridge voltage be corrected for temperature. The temperature correction to be discussed later requires the channel resistance to be properly set.

The operating resistance is the resistance of a probe in run mode with the sensor at 250˚C. The manufacturer determines the operating resistance, which is unique to each probe and is typically about 9.6 Ω. For TSI probes, the probe operating resistance is written on the box containing the probe and is an input to the IFA300. As the channel is set to run mode, current is driven through the sensor to balance the bridge circuit. The resistance of the sensor increases with temperature until the operating resistance is obtained, at which point the sensor temperature is expected to be about 250˚C.

Besides setting the resistances of the bridge circuit, there are several other settings that need to be adjusted before starting a probe. First, it is necessary to set the probe type and cable length. These settings are important because they influence the tuning of the feedback amplifier circuit that holds a constant sensor temperature in run mode. In the current study I only used film probes, but wire and non-cylindrical probe types are available. As for the cable length, only 5 m or 30 m BNC cables can be used. In the AFRL low speed wind tunnel lab we only use 5 m cables.

The next settings are the output amplifier gain and offset. These settings are adjusted to cause the IFA300 output bridge voltage to encompass a large portion of the input voltage range of the National Instruments data acquisition (DAQ) system. Utilizing a large portion of the input voltage range of the DAQ system reduces quantization error. The input voltage range of the A/D converter is ± 5 V. Using a gain of one and zero offset the bridge voltage may only vary by 1 V or less over the calibrated velocity range, so only a tenth of the DAQ input voltage range is utilized. Based on experience with several film sensors, an offset of 2 V with a gain of eight usually produces output voltages that vary by 5 to 6 V for the calibrated velocity range, thus providing a better

input voltage range for the DAQ system. It is also worth noting that I used a 16 bit A/D converter, so quantization error is expected to be negligible. Utilizing most of the input voltage range of the DAQ system was more critical for older measurement systems where 12 bit A/D converters were more common.

The final step before starting a probe is setting the low pass filter. A high pass filter is available but I never used it. Whether or not the low pass filter is used depends on the type information that is needed. The only reason for filtering is if the fluctuating velocity signal has to be constructed in the frequency domain. In that case, the sampling rate should correspond to at least twice the cutoff frequency of the low pass filter to satisfy the Nyquist criterion for preventing aliasing. The available cutoff frequencies of the IFA300 are in the user's manual. For tests requiring the frequency content of the signals, such as for obtaining the energy spectra or integral time scales, I used a 2 kHz cutoff frequency for the low pass filter and sampled at 6 kHz. The energy spectra indicated that 2 kHz is in the dissipative range of the turbulence scales in the AFRL low speed wind tunnel. For capturing data used only for computing statistics of the fluctuating signals, I acquired samples without filtering at about 160 Hz, slow enough for the samples to be uncorrelated in time.

Having discussed how to set up a probe, I will now discuss the calibration process. The purpose of the calibration is to obtain a mathematical relationship between the recorded bridge voltages, E, and the instantaneous flow velocity, v. Based on heat transfer arguments, Bruun (1995) shows that the often assumed form of the relationship between E and v is,

$$E^2 = A + Bv^n, \tag{F.1}$$

where A, B and n are constants to be determined through calibration. Equation (F.1) is commonly referred to as King's Law. The IFA300 user's manual, however, recommends a fourth order polynomial of the form,

$$v = A + BE + CE^2 + DE^3 + FE^4, \qquad \text{(F.2)}$$

where A, B, C, D and F are constants to be determined through calibration. In the IFA300 user's manual it is stated that Eq. (F.2) provides a better curve fit than Eq. (F.1). Furthermore, Eq. (F.2) is linear in the constants and the velocity is expressed directly as a function of E, making that equation more convenient than Eq. (F.1). I used the form of Eq. (F.2) for calibrations in this study.

To perform the calibrations I used a TSI Model 1127 velocity calibrator. The velocity calibrator is basically a plenum chamber with a nozzle on one end to provide a jet with a known velocity. A pressure tap on the side of the plenum chamber is used to obtain the total pressure of the jet. The difference between the jet total pressure and the room static pressure is the jet dynamic head. Calculating the jet velocity is straight forward after obtaining the density of the room air. Throttling valves upstream of the plenum are used to control the jet velocity. Figure F.2 shows a sample calibration curve.

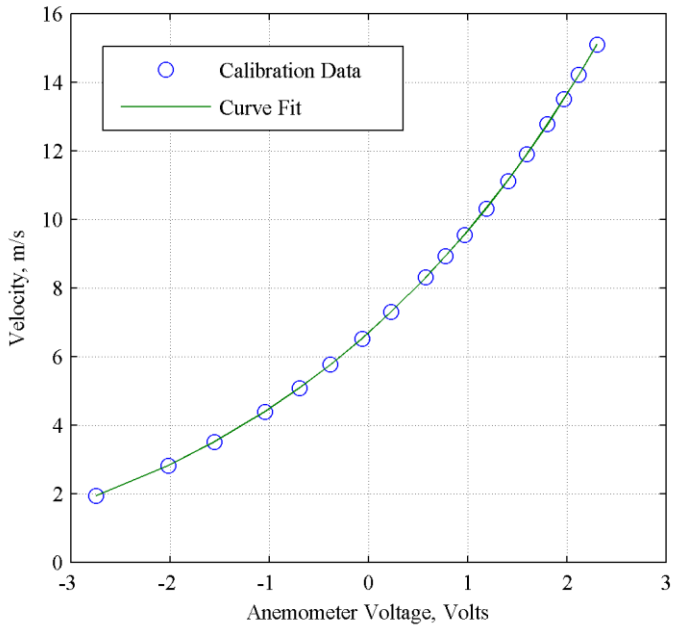

Fig. F.2 Sample calibration curve of a single hot-film sensor

The calibration curves of hot-film and hot-wire sensors are also known to be temperature dependent. The IFA300 user's manual recommends that the bridge voltages be corrected for temperature changes according to,

$$E_c = E\left(\frac{T_w - T_c}{T_w - T_e}\right)^{1/2}, \tag{F.3}$$

where E is the bridge voltage during the experiment, E_c is the corrected voltage to be used with the calibration curve, T_w is the wire temperature, T_c is the fluid temperature during calibration, and T_e is the fluid temperature during the experiment. Bruun (1995) also describes Eq. (F.3) as a temperature correction method. Equation (F.3) implies that for the temperature correction to work, T_w must be the same during experiments as it was for the calibration. For this reason it is important to recheck the channel resistance of the probes if the room temperature is different than what it was when the probe was

calibrated. If not, the sensor temperature will not be the same as it was during calibration, thus introducing an error when attempting to correct for temperature changes.

The velocities obtained from calibration curves can also be corrected for density changes. In the IFA300 user's manual, the density correction is given as,

$$v_{corr} = v_c \frac{P_c}{P}, \tag{F.4}$$

where v_{corr} is the velocity corrected for density, v_c is the velocity from the calibration curve, P_c is the atmospheric pressure during calibration, and P is the atmospheric pressure during the experiment. I corrected the hot-film measurements in this study for both temperature and density changes.

Having discussed the probe setup and calibration of individual hot-film sensors, some additional comments are in order regarding their use. In this study I used single-normal probes where the flow direction is assumed known, such as upstream of the blade row. Even downstream of the blade row the angle variation is small far away from the endwalls where the flow is primarily two-dimensional. For such applications it is important to orient the sensor normal to the jet velocity during calibration, consistent with how they are used in experiments. For complex three-dimensional flows, single-normal probes have limited use. Rather, a triple-sensor probe is used for more complex flows. Each sensor of a triple-sensor probe is set up to run using the methods described in this section for single sensors. The calibration and use of a triple-sensor probe, however, is quite different than a single-normal probe and the details are discussed in the following section.

F.2 Use of a Triple-Sensor Probe

Data reduction and analysis routines of triple-sensor probes are significantly more complex than for single-sensor probes. Such analysis routines typically relate the effective cooling velocities of each sensor to the velocity vector. The effective cooling velocity can roughly be described as the component of the velocity vector normal to the axis of the hot-film sensor. The component of velocity tangential to the sensor axis cannot convect heat away from the sensor, so that component will have less influence on cooling. Jorgensen (1971) gives the commonly used directional response equation relating the effective sensor cooling velocity, Q, to a three-dimensional velocity vector as,

$$Q^2 = v_n^2 + k^2 v_t^2 + h^2 v_b^2, \tag{F.5}$$

where v_n is the component of the velocity vector in the sensor normal direction, v_t is the component of the velocity vector in the sensor tangential direction, v_b is the component of the velocity vector in the sensor binormal direction, and k and h are yaw a pitch coefficients, respectively. Note that the normal direction is normal to the sensor and lies in a plane parallel to the prongs that hold the sensor. The binormal direction is normal to both the sensor and the plane parallel to the prongs that hold the sensor. The tangential direction is in the direction of the sensor axis. Furthermore, a right-hand coordinate system is usually assumed. For a triple-sensor probe, a Jorgenson response equation is applied to each sensor. The challenge is to invert the resulting system of nonlinear Jorgensen equations to obtain all three components of the velocity vector.

Before presenting the inversion procedure, the probe coordinate system and sensor orientations for the triple-sensor probe used in this study are shown in Fig. F.3. The beginning assumptions in the analysis are that sensor three defines the z-coordinate

direction and the velocity vector is invariant across the effective measurement diameter. The six angles, θ_i and δ_i, where i = 1, 2, and 3, define the overall probe geometry. TSI provides these angles with the probes when shipped. The open arrows connecting the long and short prongs in Fig. F.3 indicate the orientation of the tangential direction along the sensor axes. Each sensor has a unique set of axes defining the tangential, normal and binormal directions.

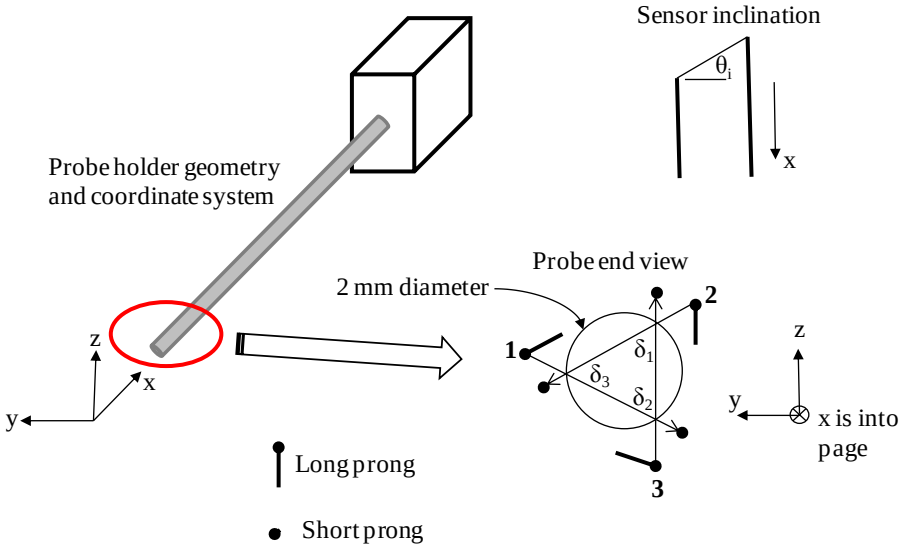

Fig. F.3 Diagram of TSI 1299-18-20 triple-sensor hot-film probe coordinate system

To begin the discussion of how to invert the Jorgensen equations, it is useful to first consider that the component of the velocity vector in a given direction is equal to the dot product of the velocity vector and a unit vector oriented in that direction. Using this idea, the Jorgensen equations for all three sensors can be written as,

$$Q_1^2 = \left(\vec{v}\cdot\vec{s}_{1,n}\right)^2 + k_1^2\left(\vec{v}\cdot\vec{s}_{1,t}\right)^2 + h_1^2\left(\vec{v}\cdot\vec{s}_{1,b}\right)^2 \tag{F.6}$$

$$Q_2^2 = \left(\vec{v}\cdot\vec{s}_{2,n}\right)^2 + k_2^2\left(\vec{v}\cdot\vec{s}_{2,t}\right)^2 + h_2^2\left(\vec{v}\cdot\vec{s}_{2,b}\right)^2 \tag{F.7}$$

$$Q_3^2 = \left(\vec{v}\cdot\vec{s}_{3,n}\right)^2 + k_3^2\left(\vec{v}\cdot\vec{s}_{3,t}\right)^2 + h_3^2\left(\vec{v}\cdot\vec{s}_{3,b}\right)^2, \tag{F.8}$$

where $\vec{v}$ is the velocity vector, $\vec{s}$ is a unit vector, the numerical subscripts indicate the sensor number and n, t, and b indicate the normal, tangential, and binormal directions, respectively. The unknowns in Eqs. (F.6) through (F.8) are the components of the velocity vector. The effective cooling velocities, Q_1 through Q_3, are outputs from the probe obtained from the calibration curves that I will discuss later. Lekakis et al. (1989) reported that typical yaw and pitch coefficients for the TSI 1299 probe are k = 0.2 and h = 1.0, respectively. I obtained reasonable angle accuracy assuming these values.

Equations (F.6) through (F.8) can be simplified if the velocity vector is written as,

$$\vec{v} = u\{1, v/u, w/u\}, \tag{F.9}$$

primarily because u can be factored out of all the terms on the right hand side. Following Gieseke and Guezennec (1993), factoring out u allows two new equations to be written,

$$Q_1^2/Q_3^2 = A = f(v/u, w/u), \tag{F.10}$$

and,

$$Q_2^2/Q_3^2 = B = f(v/u, w/u). \tag{F.11}$$

When using the probe for taking measurements, v/u and w/u are unknowns. Once v/u and w/u are known, u can be solved for using any of Eqs. (F.6) through (F.8). Due to nonlinearity, inverting Eqs. (F.10) and (F.11) analytically can be quite complex. Instead of an analytical approach, I adopted the method of Gieseke and Guezennec (1993) and used look-up tables. Since there are two unknowns, v/u and w/u, two look-up tables are needed to determine the following relations,

$$v/u = f(A, B), \tag{F.12}$$

and,

$$w/u = f(A, B). \tag{F.13}$$

To produce the look-up tables I generated an array of velocity vectors (totaling 250,000 vectors) in the uniqueness domain of the probe. The uniqueness domain is a measure of the maximum flow angle relative to the probe stem axis that has a unique solution for the velocity vector. (The probe stem is aligned with the x-axis in Fig. F.3.) Lekakis et al. (1989) show that the uniqueness domain is about 35˚ for the TSI Model 1299 probe. Furthermore to compute A and B when generating the look-up tables the unit vectors defining the normal, binormal, and tangential directions of each sensor must be defined for use with Eqs. (F.6) through (F.8). These definitions are given as,

$$\vec{s}_{1,t} = \{ \sin(\theta_1), \cos(\theta_1)\cos(3\pi/2 - \delta_2), \cos(\theta_1)\sin(3\pi/2 - \delta_2) \} \quad \text{(F.14)}$$

$$\vec{s}_{1,n} = \{ \cos(\theta_1), \sin(\theta_1)\cos(\pi/2 - \delta_2), \sin(\theta_1)\sin(\pi/2 - \delta_2) \} \quad \text{(F.15)}$$

$$\vec{s}_{1,b} = \{ 0, \cos(\pi - \delta_2), \sin(\pi - \delta_2) \} \quad \text{(F.16)}$$

$$\vec{s}_{2,t} = \{ \sin(\theta_2), \cos(\theta_2)\cos(3\pi/2 + \delta_1), \cos(\theta_2)\sin(3\pi/2 + \delta_1) \} \quad \text{(F.17)}$$

$$\vec{s}_{2,n} = \{ \cos(\theta_2), \sin(\theta_2)\cos(\pi/2 + \delta_1), \sin(\theta_2)\sin(\pi/2 + \delta_1) \} \quad \text{(F.18)}$$

$$\vec{s}_{2,b} = \{ 0, \cos(\pi + \delta_1), \sin(\pi + \delta_1) \} \quad \text{(F.19)}$$

$$\vec{s}_{3,t} = \{ \sin(\theta_3), 0, \cos(\theta_3) \} \quad \text{(F.20)}$$

$$\vec{s}_{3,n} = \{ \cos(\theta_3), 0, -\sin(\theta_3) \} \quad \text{(F.21)}$$

$$\vec{s}_{3,b} = \{ 0, 1, 0 \}. \quad \text{(F.22)}$$

As shown, the unit vectors defined by Eqs. (F.14) through (F.22) depend on the sensor angles supplied by the manufacturer.

Graphical representations of look-up tables for a probe used in the current study are shown in Figs. F.4 and F.5. The look-up tables are used for interpolating to obtain v/u and w/u, given measured values of A and B. As long as a probe does not become

damaged, one set of look-up tables is all that is needed as long as that probe is in use. To obtain the whole velocity vector I used Eq. (F.8) to solve for u,

$$u = \left[\frac{Q_3^2}{c_1(v/u)^2 + c_2(w/u)^2 + c_3(w/u) + c_4} \right]^{1/2}, \qquad \text{(F.23)}$$

where the constants c_1 through c_4 are defined in Table F.1.

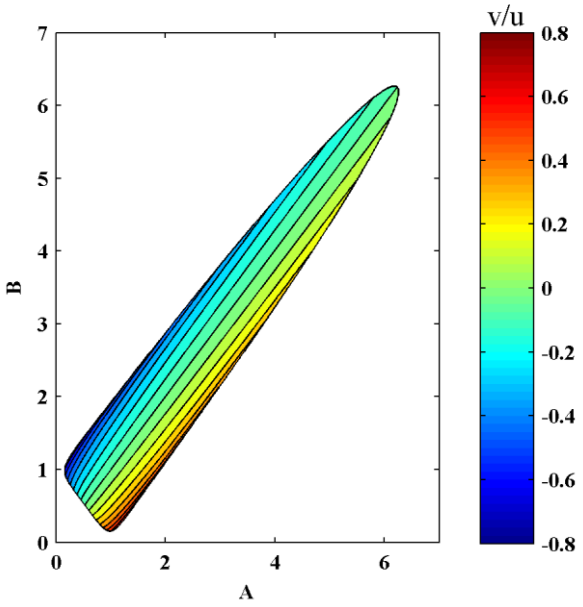

Fig. F.4 Look-up table results of v/u within the uniqueness domain of a Model 1299 probe

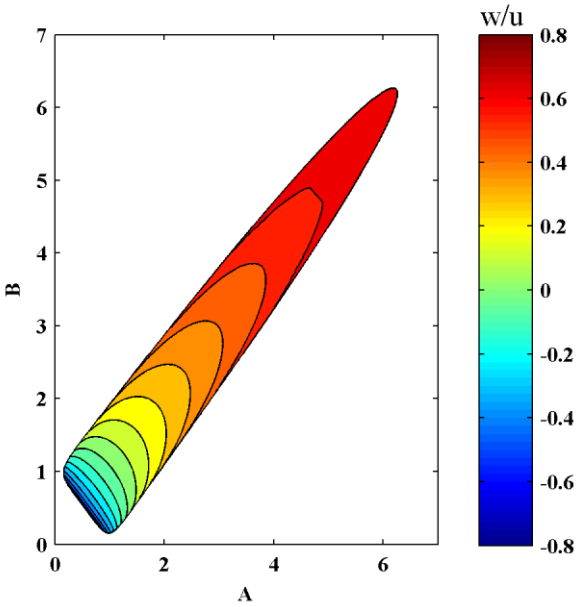

Fig. F.5 Look-up table results of w/u within the uniqueness domain of a Model 1299 probe

Table F.1 Definitions of constants used for Eq. (F.23)

c_1	h_3^2
c_2	$c_5^2 + c_6^2 k_3^2$
c_3	$2c_5c_6 + 2c_6c_7k_3^2$
c_4	$c_6^2 + c_7^2 k_3^2$
c_5	$-\sin\theta_3$
c_6	$\cos\theta_3$
c_7	$\sin\theta_3$

It is important to determine the amount of error due to the look-up table inversion algorithm. By feeding into the algorithm the effective cooling velocities, Q, that were used to produce the look-up tables, we can compare the original velocity vectors used to produce the look-up tables with the velocity vectors obtained from the algorithm. To facilitate the comparison I define two angles, γ and φ. The angle γ is the angle between the velocity vector and the x-axis (probe stem), in the range $0 \leq \gamma \leq 35^{\circ}$. The angle φ is

the rotation of the velocity vector around the x-axis and can vary in the range of $0 \leq \varphi \leq 360^{\circ}$. Together γ and φ define the range of possible velocity vectors in the probe uniqueness domain.

Errors in magnitude and flow angle due to the inversion algorithm are shown in Figs. F.6 and F.7. As shown, errors due to the inversion algorithm increase with increasing γ, with the error in the flow angle being more significant than the velocity magnitude. The flow angle γ in the experiments was typically within 10°, so the errors in flow angle and magnitude due to the inversion algorithm are essentially negligible for the experimental results.

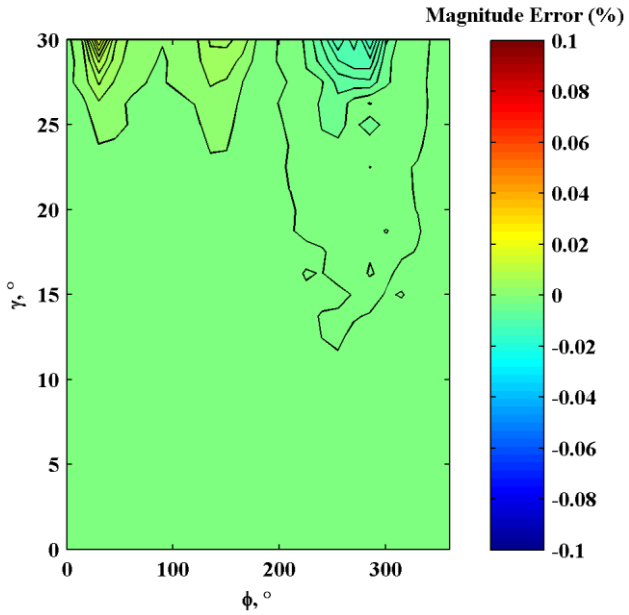

Fig. F.6 Error in velocity magnitude due to the look-up table inversion algorithm

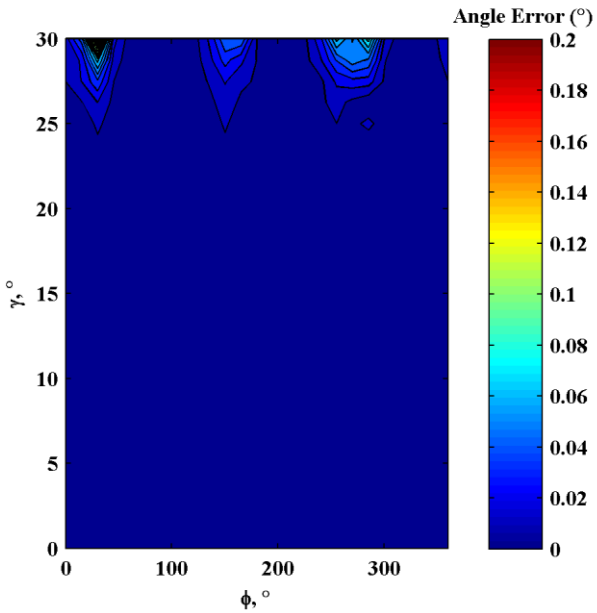

Fig. F.7 Error in flow angle due to the look-up table inversion algorithm

Having discussed the inversion procedure for obtaining the components of the velocity vector, I will now discuss the methodology for calibrating the triple probes. The purpose of the calibration is to obtain a relationship between the effective cooling velocity, Q, and the bridge voltage of each sensor. To calibrate a probe, inspection of Eqs. (F.6) through (F.8) indicates that the yaw and pitch coefficients as well as the velocity vector must be known to define the effective cooling velocities of each sensor. Recall that Lekakis et al. (1989) reported that typical yaw and pitch coefficients of the Model 1299 triple probe are k = 0.2 and h = 1.0, respectively. To define the velocity vector, the TSI Model 1127 velocity calibrator can be used to hold a probe with the probe stem in a known orientation relative to the calibration jet. Having the yaw and pitch coefficients and velocity direction defined, the calibration can be performed by varying the jet velocity magnitude to encompass the range expected in the experiment. Each

sensor can be calibrated using the methods described in Section F.1 for single sensor probes.

For all triple probe calibrations I held the probe stem in-line with the calibration jet. Subsequent checks of angle accuracy on the calibration stand indicated that the flow angle bias error is less than 0.9˚ for ± 18˚ pitch and yaw. The angle accuracy improves with reduced flow angles. Average flow angles in the experiment were typically within 10˚ of the probe stem, suggesting reasonable flow angle bias error.

In this and the previous section I discussed how to acquire instantaneous velocity measurements using single and triple-sensor hot-film probes. In the following section I discuss the methods used for calculating turbulence properties using experimental hot-film data.

F.3 Calculation of Turbulence Properties

Several turbulence parameters are presented as part of the current work, so this section is devoted to how those parameters were calculated. Specifically I will focus on the Reynolds stress tenor, the cascade inlet turbulence level, and the integral time and length scales.

For describing turbulent flows, the flow field is most often decoupled into mean and fluctuating parts,

$$v = U + u, \tag{F.24}$$

where v is the instantaneous velocity and U and u are the mean and fluctuating parts, respectively. Assuming N independent samples, the Reynolds stress tensor is calculated as (cf., Bruun, 1995),

$$\left\langle u_i u_j \right\rangle = \frac{1}{N}\sum_{n=1}^{N} u_i(n) u_j(n). \tag{F.25}$$

The cascade inlet turbulence level is calculated according to,

$$Tu_{in,st}(\%) = \frac{\sqrt{\left\langle u_{in,st}^2 \right\rangle}}{U_{in,st}} \times 100\%. \tag{F.26}$$

The numerator of Eq. (F.26) is often referred to as the r.m.s. (root mean square) level of the incoming turbulence.

The integral time scale, τ, is a useful parameter used to determine whether or not samples can be considered independent. Samples are assumed to be independent if the time lag between samples equals or exceeds approximately 2τ (cf., Bruun, 1995). The integral time scale is derived from the autocorrelation function,

$$R_{xx}(s) = \frac{\int_0^T u(t)u(t+s)dt}{\left\langle u^2 \right\rangle}. \tag{F.27}$$

In turbulence texts, T in Eq. (F.27) is usually written as ∞. I used T instead of ∞ to be representative of finite experimental sampling times. A sample autocorrelation function taken upstream of the blade row at approximately Re = 100,000 is shown in Fig. F.8. Using experimental data, τ is often calculated as the integral of R_{xx} from s = 0 to the first zero crossing of R_{xx}, approximately at 0.022 s in Fig. F.8. Tritton (1988), however, proposed an alternative definition, whereby τ is taken to be the value of s such that $R_{xx}(s) = 1/e$. For flows that contain unsteadiness in addition to being turbulent, such as for wakes downstream of blade rows, I found that the Tritton (1988) definition of τ gives more precise results. The values of τ used in the current work are therefore based on the Tritton (1988) definition. As for differences between the two methods of computing τ,

the data of Fig. F.8 indicates that τ will be approximately 4% smaller using the Tritton (1988) method compared to integrating to the first zero crossing of R_{xx}. Considering that τ is only a descriptive scaling parameter, a 4% difference between the calculation methods is of little consequence.

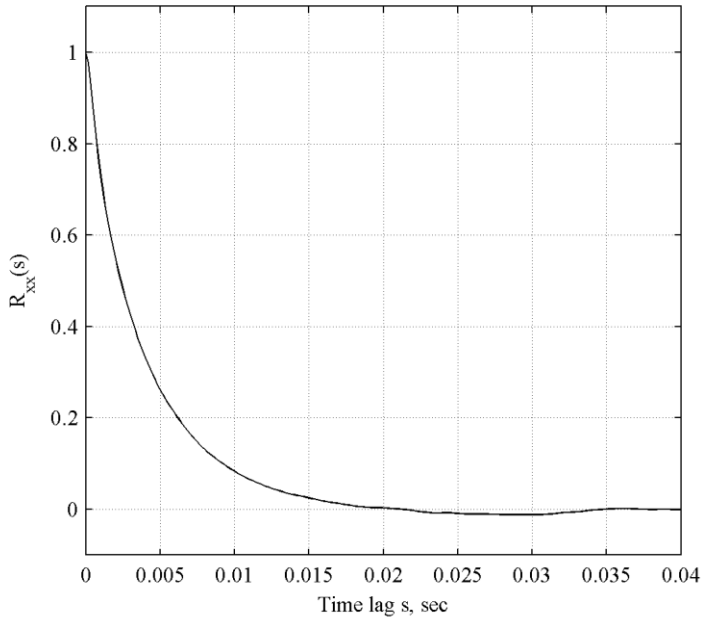

Fig. F.8 Sample autocorrelation function taken upstream of the blade row at Re = 100,000

The integral length scale, L, is a parameter used to describe the size of the large energy-containing eddies of a turbulent flow. Using Taylor's frozen turbulence approximation, L is usually estimated from stationary hot-wire and hot-film measurements as,

$$L = U\tau\,, \tag{F.28}$$

where U is the mean flow velocity.

Appendix G: Surface Flow Visualization Technique

In this appendix I briefly describe the procedures for conducting the surface flow visualization tests. The purpose of surface flow visualization is to gain insight into the state of the boundary layer on the wetted surfaces, at least qualitatively. By coating the airfoil surfaces with oil and running the wind tunnel, the resulting motion or lack of motion of the oil indicates whether or not the boundary layers are attached. A surface where the oil flows indicates an attached boundary layer as well as the flow direction. The lack of oil motion results from very small shear stress on the surface, perhaps due to separated flow. Furthermore, oil collection and dispersion on the surface indicates separation and reattachment, respectively.

I conducted oil flow visualizations on the suction surfaces of the L2A and L2F profiles near the endwall to look for the presence of separation effects. The orientation of the camera relative to the blade surface is shown in Fig. G.1. As shown, I mounted the camera outside of the tailboard with the lens placed to view through a hole in the tailboard. Line of sight of the camera was nearly orthogonal to the suction surfaces of the profiles. I used an Olympus C-5060 digital camera for acquiring images. I used a halogen T-3 lamp placed outside of the wind tunnel for illuminating the surface while acquiring images.

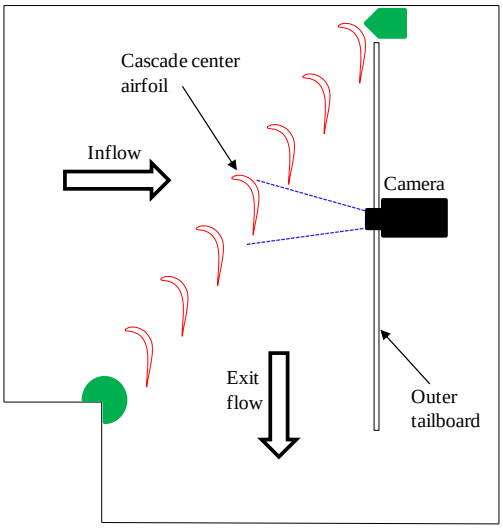

Fig. G.1 Diagram of camera orientation and view angle for suction surface flow visualization

Oil flow visualization in the AFRL low speed wind tunnel was challenging, primarily due to weak surface shear associated with low Mach numbers ($M < 0.06$). The typical problem was that fluids that can be applied to the surface without being influenced by gravity prior to starting the wind tunnel will usually be too viscous to be driven by the air flow. A mixture of dish washing detergent and food coloring had reasonable viscosity, but was prone to producing bubbles on the surface during application. I also tried to use propylene glycol, but the viscosity was too low. In the end I used a mixture of approximately 1 part black chalk line chalk to 20 parts mineral oil. The mineral oil had about the right viscosity and I added chalk line chalk for visualization. The mixing ratio of the mineral oil and chalk does not have to be exact and the chosen mixture will depend on the application of the technique and the available lighting.

Avoiding gravity effects during application of the oil also required that a very thin layer of oil be applied to the blade surface. To apply thin layers of oil I used a double

action Paasche VL airbrush. Using the airbrush I was able to apply a thin and relatively even layer of oil-chalk mixture to the surface. Figure G.2 shows the suction surface of the L2F airfoil after applying the oil-chalk mixture but before turning on the wind tunnel. As shown, there is some variation in darkness across the surface but the whole area is covered with oil. Since the results are based on the oil motion, the varying darkness prior to exposing the surface to the air flow is not significant. Furthermore, the oil did not run down the surface prior to turning on the wind tunnel.

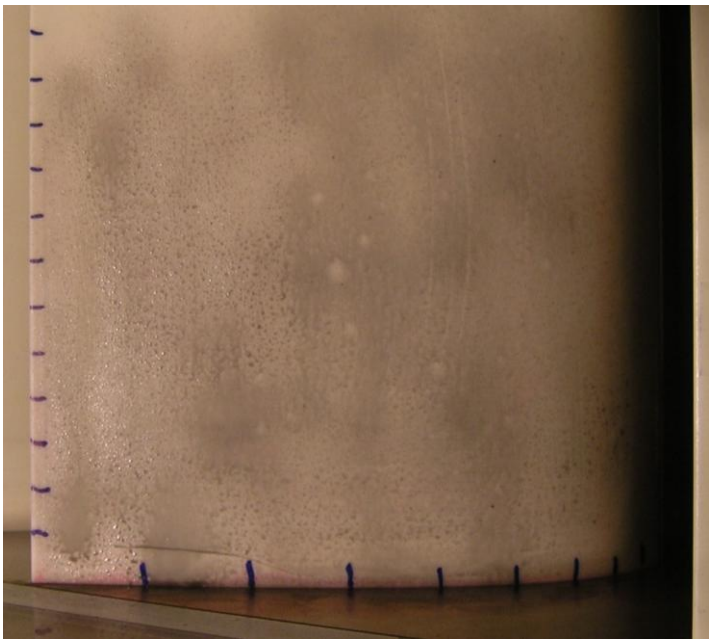

Fig. G.2 L2F suction surface with oil-chalk mixture applied prior to air flow exposure

After applying the oil-chalk mixture and capturing a baseline image with no air flow, I turned on the wind tunnel to the desired Reynolds number, Re = 100,000 for all tests in this study. I acquired images for 25 to 30 minutes in approximately one minute intervals or until the oil had essentially stopped moving. To interpret the data I cropped the images to the desired viewing area and compiled them into videos using Matlab.

Using the videos to virtually speed up the tests indicated surface flow features such as separations and reattachments as well as flow directions. Furthermore based on the videos, it was clear that although gravity did not play a role prior to starting the wind tunnel, gravity effects occurred later in the tests as oil built up on certain regions of the surface. For example, the shear stress near the leading edge is strong, driving most of the fluid towards the trailing edge. As the shear stress weakens in the presence of the adverse pressure gradient, the flow tends to build up and run down the profile toward the endwall. Because of this effect, one must be careful when looking for direction information and should focus on the beginning of the video before significant gravity effects occur. Analyzed flow visualization results are shown and discussed in Chapters 6 and 7.

Appendix H: Turbulent Boundary Conditions for the Wilcox (1998) k-ω Model

In this appendix I describe the process of determining reasonable turbulent boundary conditions for use with the LEO code that uses the Wilcox (1998) k-ω turbulence model. In the end I used the recommended default turbulent boundary conditions from the LEO user's manual, equaling $Tu_{in,st}$ = 1% and $L_{in,st} = 0.0017C_{ax}$ for the geometries in this study. Seemingly arbitrary boundary condition specifications should be taken with skepticism, so I investigated how the model behaves with boundary conditions closer to experimental levels. As will be shown, the length scale significantly influences the total pressure loss. In fact, using experimental values of turbulence level and length scale produces errors in total pressure loss exceeding 50%. Therefore in this appendix I discuss how to set the turbulent boundary conditions to produce good results. I first show how experimental length scales relate to the length scale definition of Wilcox (2006), followed by a discussion of the sensitivity of calculation results to the specified length scale. Although I use the Wilcox (2006) book as a reference in the following analysis, he did not change the length scale definition from what he used in earlier versions of the model.

Wilcox (2006) defines the integral length scale as,

$$L(\vec{x},t) = \frac{3}{16}\int_0^\infty \frac{R_{ii}(\vec{x},t;r)}{k(\vec{x},t)}dr, \tag{H.1}$$

where k is the turbulent kinetic energy ($k = (\langle u^2\rangle + \langle v^2\rangle + \langle w^2\rangle)/2$), R_{ii} is the trace of the two-point velocity correlation tensor,

$$R_{ij}(\vec{x},t;r) = \left\langle u_i(\vec{x},t)u_j(\vec{x}+r,t)\right\rangle, \tag{H.2}$$

$\vec{x}$ is a vector denoting the position in the flow, t is time, and r is the distance separating the two points in the correlation. The brackets in Eq. H.2 indicate the time-averaging operator. The term R_{ii} is expanded as,

$$R_{ii} = R_{11}(\vec{x}, t; r) + R_{22}(\vec{x}, t; r) + R_{33}(\vec{x}, t; r), \tag{H.3}$$

where R_{11} is the two-point velocity correlation in the longitudinal, or streamwise direction, and R_{22} and R_{33} are for the transverse directions. R_{11} can be approximated from experimental data by applying Taylor's frozen turbulence approximation and multiplying the autocovariance function by the mean streamwise velocity,

$$R_{11} = U_{st} Q_{xx}(s), \tag{H.4}$$

where,

$$Q_{xx}(s) = \langle u(t) u(t+s) \rangle, \tag{H.5}$$

and s is the time lag. Assuming isotropic turbulence, Pope (2000) shows that $R_{22} = R_{33} = R_{11}/2$. Hence, $R_{ii} = 2R_{11}$. Now assuming that the turbulence is both homogeneous and statistically stationary, an adequate assumption for grid turbulence, we can drop the arguments $\vec{x}$ and t to restate the definition of the length scale as,

$$L = \frac{3}{8} \int_0^\infty \frac{R_{11}(r)}{k} dr. \tag{H.6}$$

In experiments, the integral length scale is commonly defined as,

$$L_{exp} = \int_0^\infty \frac{R_{11}(r)}{< u^2 >} dr. \tag{H.7}$$

Substituting Eq. H.7 into Eq. H.6 gives,

$$L = \frac{3}{8} \frac{L_{exp} < u^2 >}{k}. \tag{H.8}$$

Assuming isotropic turbulence,

$$k = \frac{3}{2} < u^2 > . \tag{H.9}$$

Substituting Eq. (H.9) into Eq. (H.8) shows that,

$$L = L_{exp}/4 . \tag{H.10}$$

Had I determined the relationship of the Wilcox (2006) definition of length scale to the experimental length scale using only the longitudinal component of R_{ii} (the only component we usually measure) rather than finding the relationship for the full trace, the result would have been $L = L_{exp}/8$.

Preliminary calculations with LEO indicated that using the experimental levels of turbulence intensity and length scale (prior to conducting the above analysis) resulted in unreasonably high total pressure loss. This result of excessive loss is what prompted me to further investigate the effect of length scale and determine the relationship of the experimental length scale to the definition used with the k-ω model. Unfortunately, specifying the length scale based on the above analysis also resulted in poor results. Figure H.1 compares with experiments predictions of the L2F profile loss based on the above analysis (triangles) and also based on the recommended default inputs from the LEO user's manual (squares, chosen settings in this work). Although in the analysis I determined a relationship between the measured integral length scale and the definition of length scale based on the turbulence model, the agreement with experiments is poor. The difference is primarily due to sensitivity of the turbulence model to the length scale. One may note that the turbulence level is different for the two sets of predictions in Fig. H.1, suggesting a possible confounding effect. However, calculations using different turbulence levels while holding the length scale constant showed that the turbulence model is much less sensitive to the turbulence intensity than the length scale. Unlike the

results using boundary conditions derived from the experiments (triangles), results using the default settings (squares, chosen settings in this work) are in much better agreement with experiments. The code developers presumably chose the default settings because they provide good results for typical turbomachinery flows.

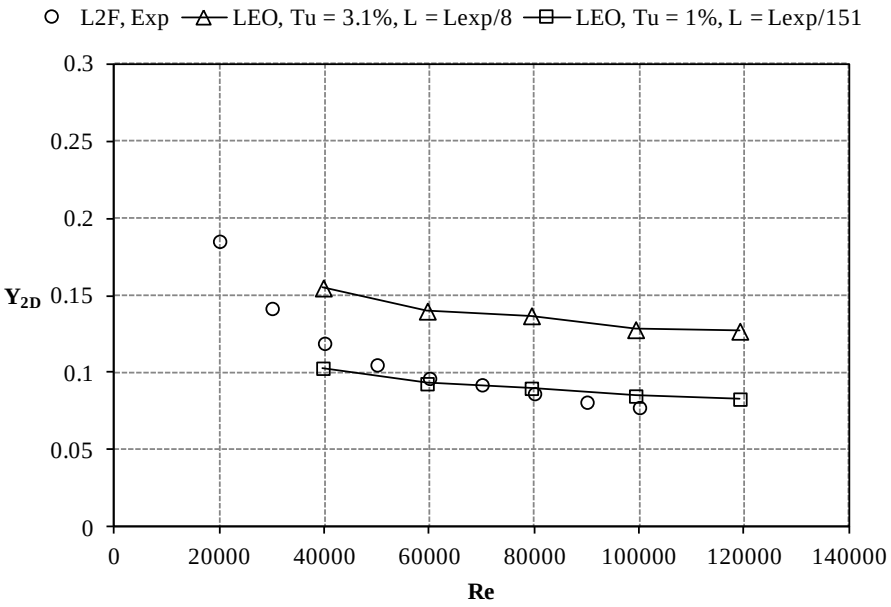

Fig. H.1 Comparison of LEO predictions with experimental profile loss of L2F to show the effect of turbulent boundary conditions (Computed with fully turbulent calculations)

To provide more insight into the effect of the length scale, Fig. H.2 shows the calculated profile loss of L2F for several length scales. As shown, reducing the length scale in LEO significantly reduces the total pressure loss, with the default settings in LEO providing reasonable results. Reductions in integral scale beyond the default setting have less of an influence on the predicted loss compared to the larger settings. Subsequent calculations with L2A indicated that the default settings also provide reasonable results with that profile, so I used the defaults settings for all calculations of the current study.

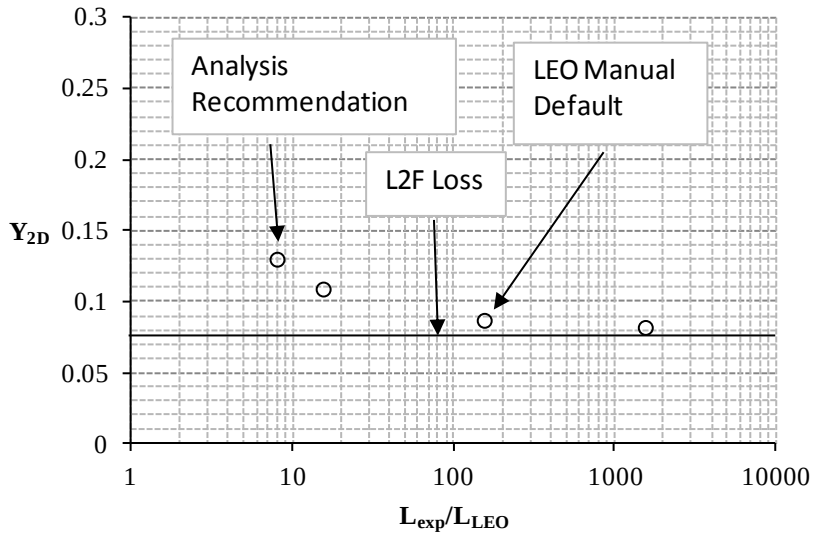

Fig. H.2 Effect of the integral length scale on L2F loss predictions using LEO, Tu_{in} = 3.1%, Re = 100,000

The implication of the results of Figs. H.1 and H.2 is that the integral scale used for calculations with the Wilcox (1998) k-ω turbulence model does not appear to correlate to the physical scales present in the flow. Wilcox (2006) shows a significant sensitivity of the k-ω model to finite freestream boundary conditions. Furthermore in his book, Wilcox (2006) does not provide practical guidance for specifying the freestream turbulent boundary conditions and suggests that they can be adjusted as calculations proceed. For the LEO code to be practical, it is necessary to determine appropriate turbulent boundary conditions for the type of flow being considered, a task apparently accomplished by the LEO code developers. The results of Fig. H.2 suggests that the integral length scale can be reduced to the point that it no longer has a significant influence on the results. Fortunately, this reduction in length scale also provides much improved results (see Fig. H.1) compared to those obtained using boundary conditions derived from experiments, which were of poor quality.

In conclusion, shortcomings of the turbulence model do not preclude the use of the LEO code as a valuable design tool. Being a RANS code, it should be understood that LEO is not wholly reliable in terms of absolute accuracy. The primary use of the code is to detect the presence of physical effects and compare results between profiles. Any CFD user should always be skeptical of results and be familiar with known shortcomings of the code and turbulence models they are using.

Appendix I: Profile Loss Calculations using Fluent with the Walters and Leylek (2005) k-k_l-ω Laminar-Turbulent Transition Model

In this appendix I describe the methodology for calculating the profile loss of the L2A and L2F profiles using the commercial code Fluent, which included the transition model of Walters and Leylek (2005). The results using this code are discussed in Chapter 5. I used calculations using Fluent along with results for the TDAAS code (supplied by Dr. John Clark of AFRL/RQTT) as benchmarks to compare with the LEO code. For flows with Re in the range of interest in the current study, blade surface boundary layers tend to be transitional. As shown in Chapter 5, the Fluent code with transition capability provides a slight improvement over the LEO code at high Re, but predicts stall prematurely with decreasing Re compared to experiment. On the other hand, fully turbulent calculations using the LEO code tend to eliminate separation bubbles, thus causing the boundary layers to remain attached at low Re when they should be separated. Thus, neither code performs well at low Re. The additional complexity of manual grid generation and the higher fidelity turbulence model available in Fluent did not provide a sufficient improvement over the design code LEO to warrant the use of the Fluent code. Nevertheless for completeness, I describe the k-k_l-ω model and summarize the procedures for performing the Fluent calculations in this appendix.

I.1 Model Description

Walters and Leylek (2004, 2005) developed the transition model implemented in Fluent for modeling both natural and bypass transition. In natural transition, laminar boundary layers grow, eventually becoming unstable with the formation of Tollmien-

Schlichting waves. As the flow continues, the Tollmein-Schlichting waves break down, forming turbulent spots, which are followed by a fully turbulent boundary layer. In bypass transition, freestream turbulence causes the natural process to be bypassed. (Schlichting and Gersten (2000) discuss both types of transition.) The three transport equations in Fluent are used to solve for the turbulent kinetic energy, k, the laminar kinetic energy, k_l, and the specific dissipation, ω. Walters and Leylek (2004, 2005) added the transport equation for k_l to model streamwise laminar fluctuations in a pre-transitional boundary layer that eventually transitions to a turbulent boundary layer. After transition initiates, k_l is transferred to k to model the transition to full turbulence.

The k-k_l-ω model in Fluent was originally proposed as k-k_l-ε (2004), where ε is the farfield turbulence dissipation rate. The authors then recast the transport equation for ε in terms of ω (Walters and Leylek, 2005). The model constants were determined from direct numerical simulations of fully turbulent channel flow and flat plate boundary layer experiments (Walters and Leylek, 2005). The latter model is commercially available in Fluent and was used in the current study.

Because the k-k_l-ω model is recent, there are few studies in the literature using it. Sanders et al. (2009, 2011) reported that the model is a more accurate predictive tool for LPT airfoils as compared to conventional RANS based models. Cutrone et al. (2007) compared the predictive quality of the k-k_l-ω model with five other transition models, all derived by combining a transition onset correlation with an intermittency factor based transition model to model the transition length. Cutrone et al. (2007) concluded that the k-k_l-ω model performed best in all cases except a flat plate case that had a strong pressure gradient in the transition region.

I.2 Calculation Methods and Grid Refinement

As for performing the calculations in Fluent, I used the pressure-based solver due to low Mach numbers in the experiment ($M_{ex} < 0.06$). Second order accurate finite volume spatial discretization was utilized. For time integration, either steady or unsteady formulations were used, depending on the Reynolds number. In general, the steady solver was used for high Reynolds numbers with convergence being assumed when the scaled residuals for mass flow and momentum dropped by at least five orders of magnitude. At low Reynolds numbers solutions usually failed to converge using the steady solver, which was evident by the lift coefficient and scaled residuals not reaching steady state. In that case, unsteady solutions were computed with an implicit, dual time-stepping formulation with second order accuracy. The time-steps were adjusted to allow the scaled residuals to decrease by five orders of magnitude within 20 to 30 sub-iterations. Solutions were assumed converged when the lift coefficient became steady periodic, indicating that all effects of initialization had decayed. I calculated the loss coefficients for the unsteady cases by time-averaging the loss results over one period of the lift coefficient.

The domain modeled in Fluent was based on a single airfoil, with the inlet extending approximately $0.80C_{ax}$ upstream of the leading edge in the axial direction. The pressure outlet was placed approximately $1.07C_{ax}$ downstream of the trailing edge in the axial direction. Periodic boundaries were assigned approximately mid-pitch from the pressure and suction surfaces to model a single blade passage. I assigned a constant velocity inlet to precisely set Re for each case. I set the turbulence level and integral

scale at the inlet to be consistent with the experimental values given in Table C.1. According to Roach (1987) and verified by monitoring the inlet turbulence level during experiments, the inlet turbulence conditions are insensitive to Re.

The calculations were carried out using two dimensional multi-block hybrid grids. A structured block with an O-type topology was used for discretizing the boundary layer around the airfoil surface, while an unstructured block was used for discretizing the remainder of the domain. The leading edge region of the L2A computational mesh is shown in Fig. I.1to illustrate the hybrid grid topology.

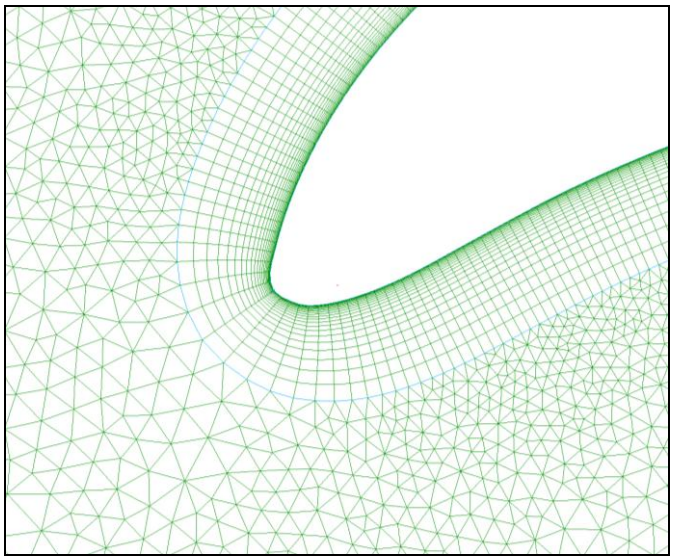

Fig. I.1 Close-up image of the L2A leading edge to show the hybrid grid topology

Unlike the WAND code that is optimized for producing turbomachinery grids for use with the flow solver LEO, I used the general purpose mesh generator Gridgen to define the computational domain for use in Fluent. Since the intent of the Fluent calculations was to predict the profile loss and the onset of flow separation, it was very important to determine that the results are mesh independent. I determined a sufficient

mesh density by checking both the blade surface static pressure coefficients and the mass-averaged total pressure loss at Re = 100,000. I chose Re = 100,000 to conduct the grid independence study because gradients in the flow are stronger at high Re than low Re. Further note that at the time I conducted the grid independence study, I did not know the experimental turbulent conditions at the inlet. For the purpose of conducting the grid independence study I arbitrarily used $Tu_{in,st}$ = 1% and $L_{in,st} = 0.03C_{ax}$ as turbulent boundary conditions. Figure I.2 is a plot of the static pressure coefficients for three different mesh densities for the L2A profile. As shown, results for grids two and three are nearly identical. Likewise in Fig. I.3 for L2A, Y_{2D} is basically the same for grids two and three, demonstrating that the results are essentially grid independent. I chose the grid density corresponding to grid two for all Reynolds lapse calculations for the L2A and L2F profiles.

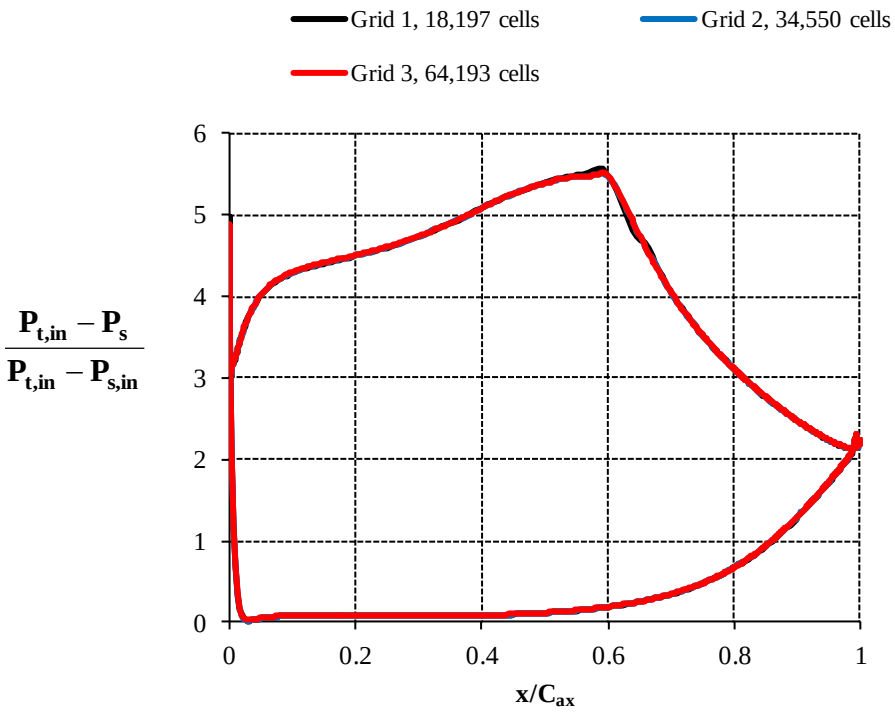

Fig. I.2 Plot of static pressure coefficients with different mesh densities to show grid independence

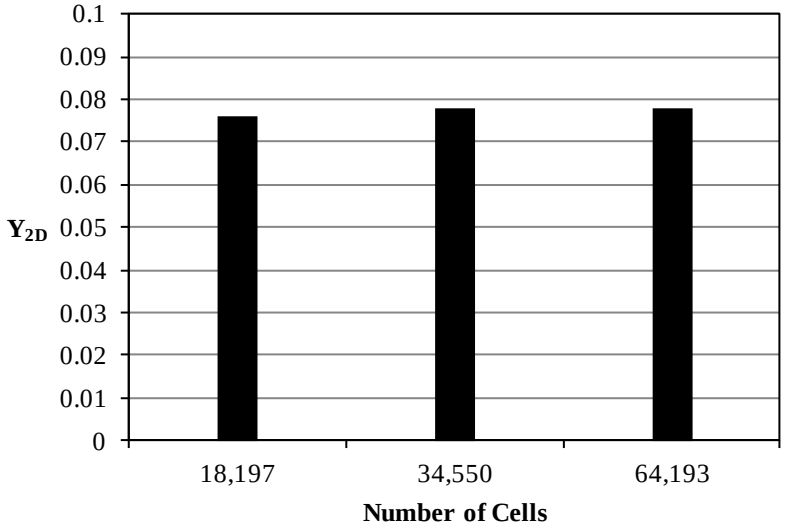

Fig. I.3 Plot of Y_{2D} with different mesh densities to show grid independence

As an additional check of the grid, I ran cases with the outlet of the flow domain extending $0.53C_{ax}$, $1.07C_{ax}$, and $1.60C_{ax}$ downstream of the trailing edge in the axial direction, but with the grid density of grid two in Figs. I.2 and I.3. The different extents of the flow domain had a negligible influence on the total pressure loss. Note that for the grid sensitivity study, the flow domain extended $0.53C_{ax}$ downstream of the blade row. For all profile loss calculations shown in Chapter 5 using Fluent, I used the mesh extending $1.07C_{ax}$ downstream of the blade row to be able to extract data $0.75C_{ax}$ downstream of the blade row, consistent with the experiments. The final mesh had approximately 60,000 cells for the L2A and L2F profiles.

As a final note, the k-k_l-ω turbulence model required that the equations be integrated all the way to the wall, without the use of wall functions. As shown in Fig. I.4

for L2A, the y^+ levels are less than unity over most all of the airfoil surface, indicating sufficient grid resolution of the near wall region.

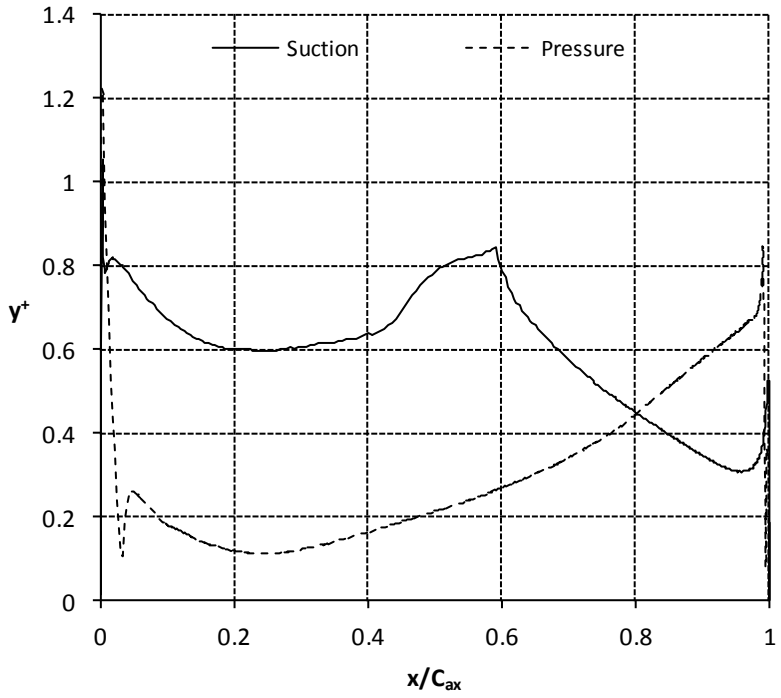

Fig. I.4 Plot of surface y^+ levels for L2A showing sufficient near wall grid resolution

Appendix J: Two and Three-Dimensional CFD Results Obtained Using LEO for Calculating the Endwall Loss of the Research Profiles

This appendix contains the results of calculations using the LEO code for predicting Y_{2D} and Y_{ps}. I used two-dimensional models without endwall effects for calculating Y_{2D} and modeled the entire passage for calculating Y_{ps}. The reason I used separate models was to isolate effects due to the profile and endwall flows. As a consequence of using separate models and the way in which Re is manipulated using the LEO code via adjusting the back pressure, matching Re between the two and three-dimensional models was impractical. As a work-around, I ran cases over a range of Re values to enable curve-fitting to obtain Y_{2D} and Y_{ps} at desired Re values. Least squares fits of nonlinear curves of the form $Y = aRe^{b} + c$, where a, b and c are constants fit the data reasonably well for all cases. Having Y_{2D} and Y_{ps} at the same Re setting enables a more accurate calculation of Y_{ew}, which is the difference between Y_{ps} and Y_{2D}.

All total pressure loss data in this appendix were obtained directly from the output files of the LEO code based on mass-weighted averages. Total pressure loss is scaled by the inlet dynamic head for computing the loss coefficients. The downstream total pressure was captured one axial chord downstream of the blade row for all cases.

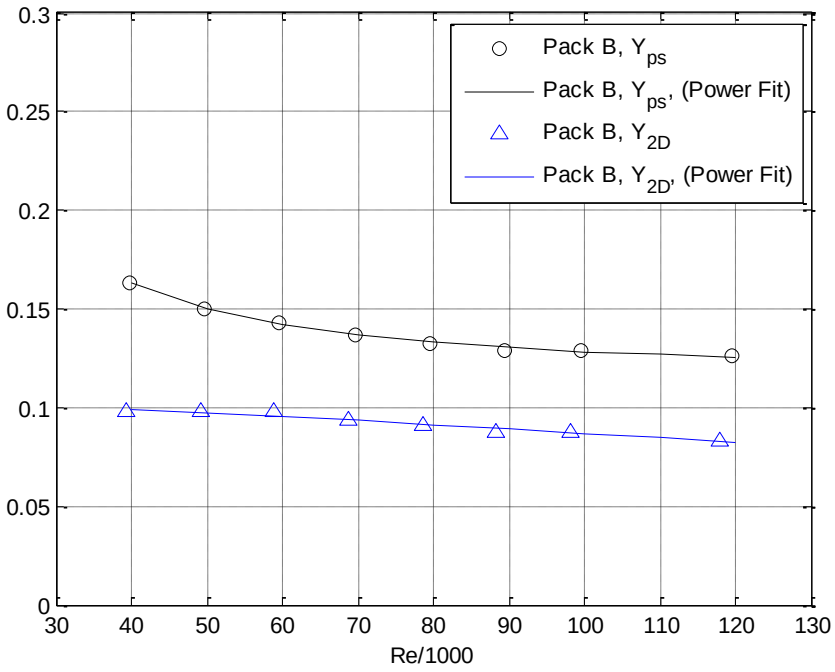

Fig. J.1 Y_{ps} and Y_{2D} Reynolds lapse data using LEO for Pack B

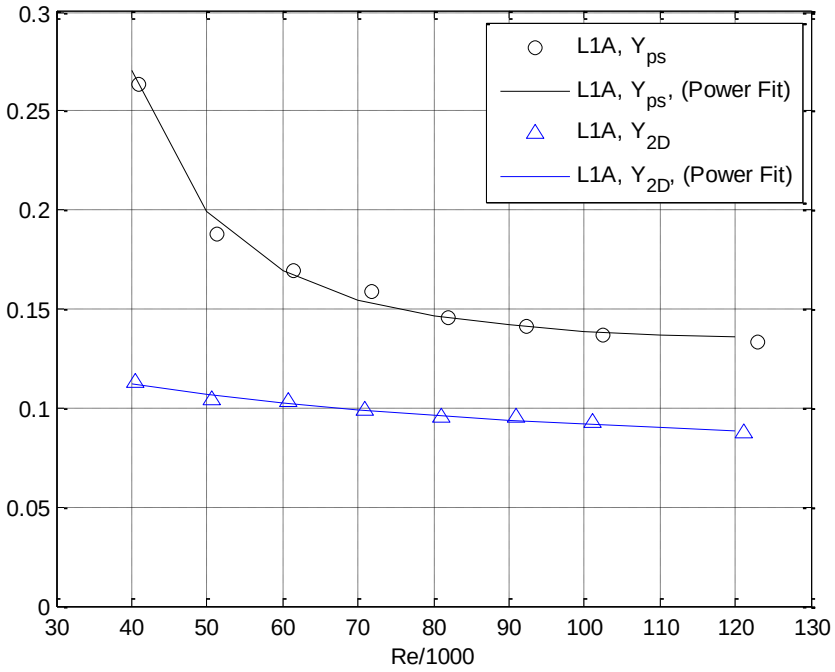

Fig. J.2 Y_{ps} and Y_{2D} Reynolds lapse data using LEO for L1A

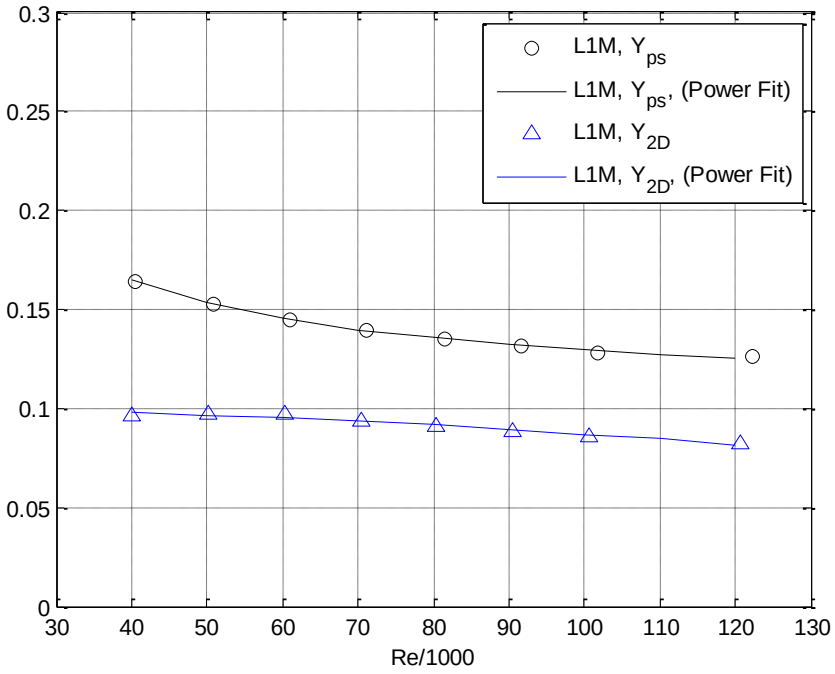

Fig. J.3 Y_{ps} and Y_{2D} Reynolds lapse data using LEO for L1M

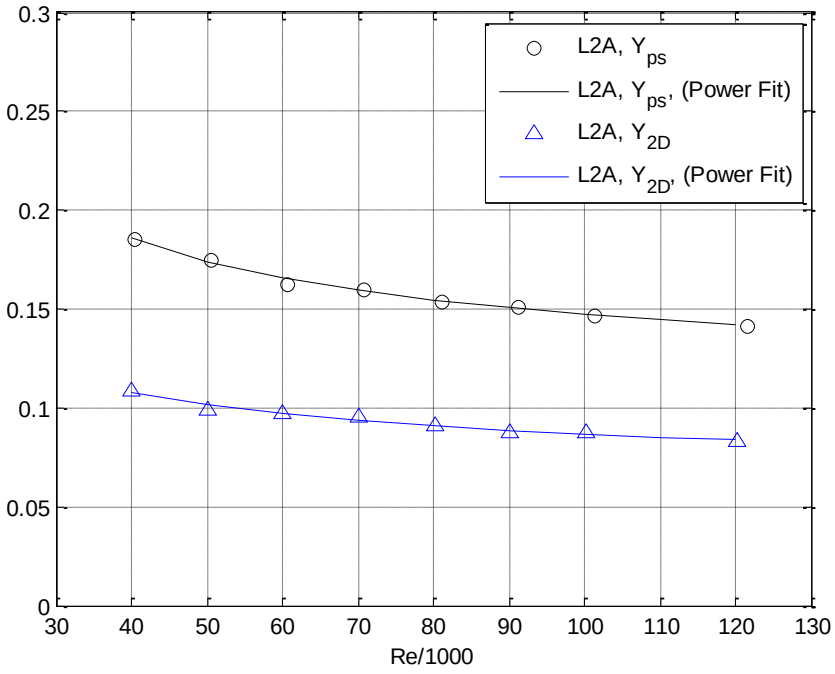

Fig. J.4 Y_{ps} and Y_{2D} Reynolds lapse data using LEO for L2A

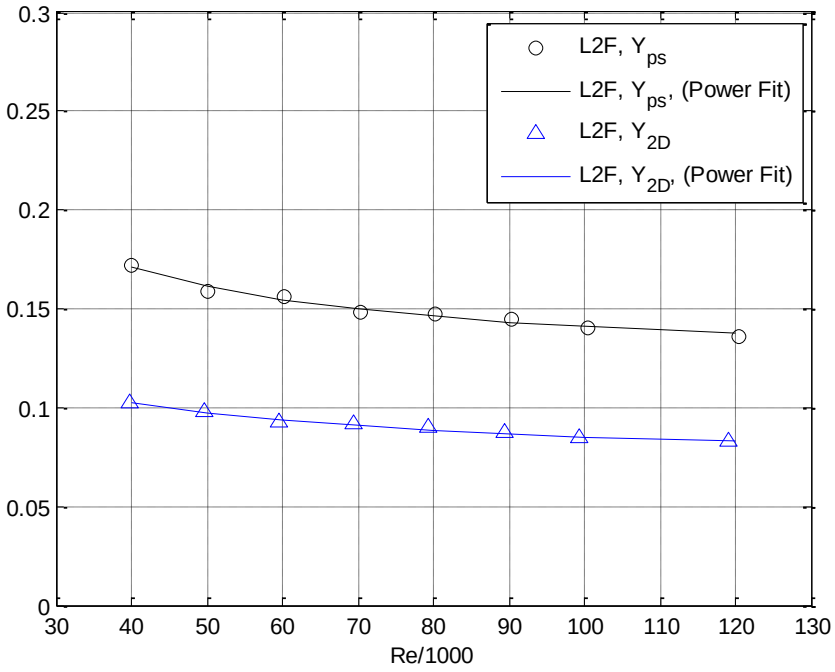

Fig. J.5 Y_{ps} and Y_{2D} Reynolds lapse data using LEO for L2F

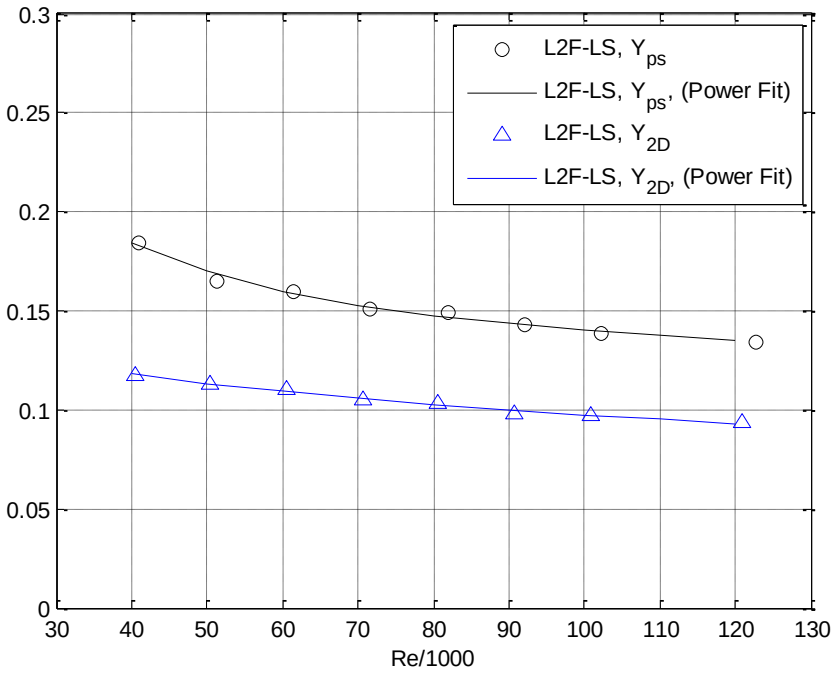

Fig. J.6 Y_{ps} and Y_{2D} Reynolds lapse data using LEO for L2F-LS

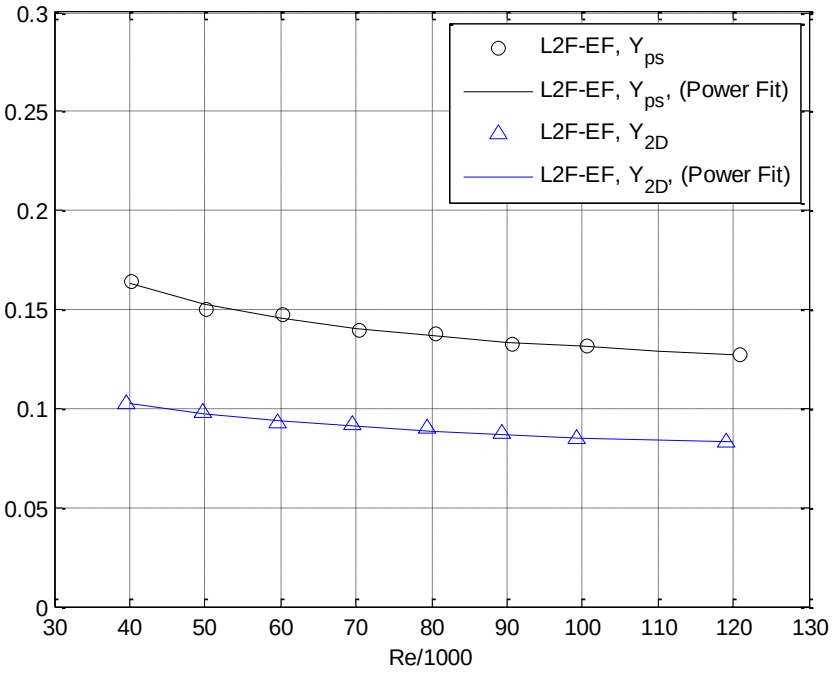

Fig. J.7 Y_{ps} and Y_{2D} Reynolds lapse data using LEO for L2F-EF

Appendix K: Design of the L2F-LS Profile

This appendix documents the design of the L2F-LS profile. The design intent was to produce a low stagger version of the L2F profile to provide an additional testbed for investigating stagger angle effects. L2F-LS was designed to have the same pitchwise spacing, gas angles and front-loading as L2F, but with a stagger angle consistent with the L1-series profiles and Pack B.

As shown in Chapter 3, the BLFP number (See Eq. 3.10) is indicative of how front-loaded a profile is. To preserve good low Re performance, the new profile will need $BLFP_{new} \geq BLFP_{L2F}$. Furthermore, the results of Section 8.1 suggest that reducing the stagger setting will limit Y_{ew}. The L1M stagger setting, $\lambda = 25.8^{\circ}$, which is nearly equivalent to that of Pack B is expected to reduce Y_{ew} compared to L2F and is the chosen stagger angle of the new profile.

Dr. John Clark of AFRL/RQTT implemented the BLFP and λ constraints in the Turbine Design and Analysis System (TDAAS) to produce the new profile while preserving the pitchwise spacing and flow turning of L2F. The TDAAS system employs the profile generator of Clark et al. (2009). That algorithm uses Bezier curves in conjunction with typical leading- and trailing-edge specifications (e.g., wedge angles, edge radii of curvature, gage areas, and uncovered turning) to define airfoil shapes using a small number of control points according to the method described by Casey (1994). Once the profile was defined, the Wildcat code of Dorney and Davis (1992) was used along with an ad hoc implementation of Praisner and Clark's (2007) separated flow transition model to determine airfoil performance. Graphical User Interfaces (GUIs) and

both design optimization (Vanderplaats, 1984) and design-of-experiments techniques (Santner et al., 2003) were used during the design process to define the shape of the profile.

The new profile generated using TDAAS is shown in Fig. K.1 and compared with L2F. This new profile is a baseline design that I later modify to further improve its performance. As shown, the constraint that limits the stagger setting, combined with the large pitchwise spacing and front-loading of L2F results in an extremely thick profile. The suction surface of the new profile is also highly curved, extending upstream of the leading edge. The primary effect of the large profile thickness is that the stagnation point moves from just under the leading edge for L2F to the front side of the new profile. Flow passing over the leading edge of the new profile induces a pressure surface separation bubble. I later modify the pressure surface to eliminate the separation bubble.

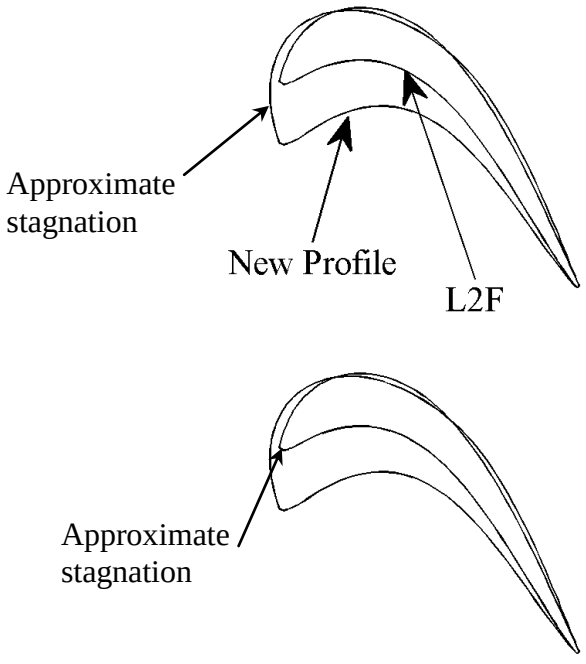

Fig. K.1 Comparison of the new baseline profile with L2F

Figure K.2 shows the predicted pressure loadings and Reynolds lapse performance of the new baseline profile and L2F. As shown, the baseline profile is front-loaded, reaching peak suction approximately at x/C_{ax} = 0.19. The resulting BLFP number is 6.74, 14% larger than the L2F BLFP number. Accordingly, the Reynolds lapse shown in Fig. K.2b shows that the baseline profile performs quite well at low Re, similar to L2F. The new profile, however, is predicted to stall below Re = 15,000, which is still very low. Although experimental data are not available to verify the Reynolds lapse of the new profile, predictions for L2F using TDAAS are in good agreement with the experimental data. For all Re, the baseline profile is expected to have higher Y_{2D} than L2F. The elevated loss may partly be due to the previously mentioned pressure surface separation bubble, visualized in Fig. K.3 using Y contours. The notch in the Cp curve approximately at x/C_{ax} = 0.05 in Fig. K.2a suggests the presence of the pressure surface separation bubble. There is also a notch in the suction side Cp curve of the new baseline profile approximately at x/C_{ax} = 0.65. It is not known whether the notch in the suction side Cp curve has a favorable or adverse effect on Y_{2D}.

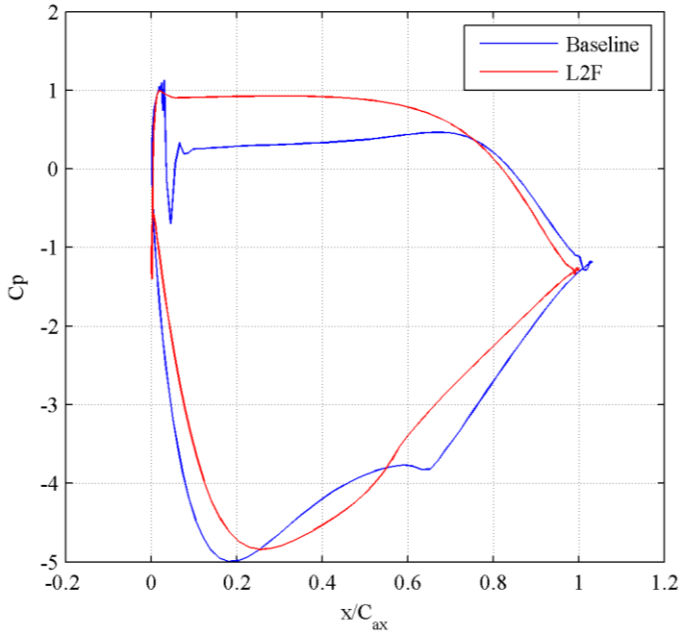

a) Pressure Loading, LEO

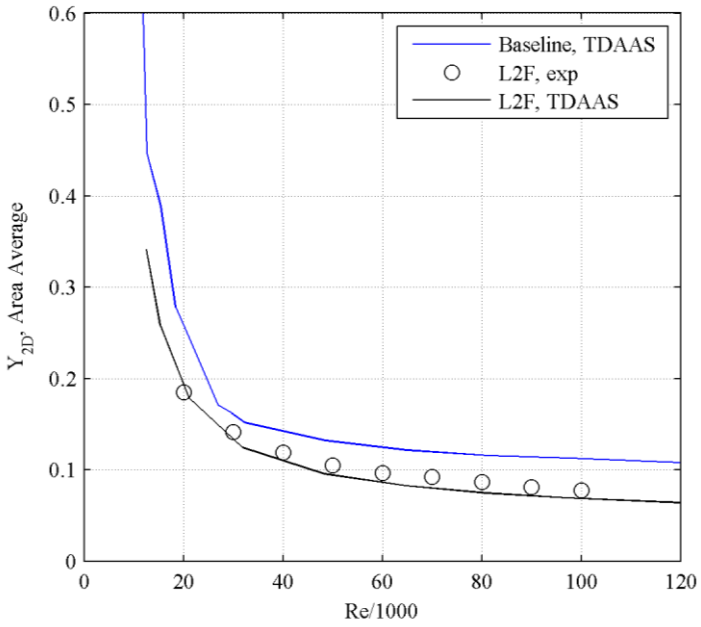

b) Reynolds lapse, TDAAS

Fig. K.2 Pressure loading and Reynolds lapse performance of the new baseline profile

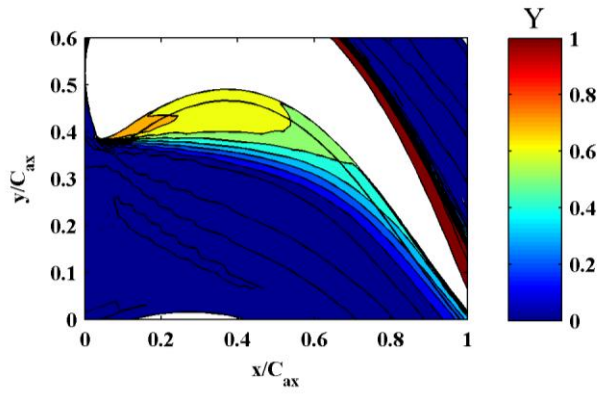

Fig. K.3 Pressure surface separation of the new baseline low stagger, front-loaded profile (Obtained using the LEO code, Re = 100k)

Blanco et al. (2003) has shown that pressure surface separation bubbles can increase Y_{ew}. In practice, profiles are often modified to eliminate pressure surface separation bubbles. Figure K.4 shows several variations of the baseline profile and also illustrates the procedure for modifying the pressure surface. The idea is to manipulate the airfoil shape to occupy the space of the separation bubble that occurs for the baseline design. The modified pressure surfaces of Fig. K.4a resemble the Y contours adjacent to the pressure surface of the baseline design in Fig. K.3 that indicate the presence of the separation bubble.

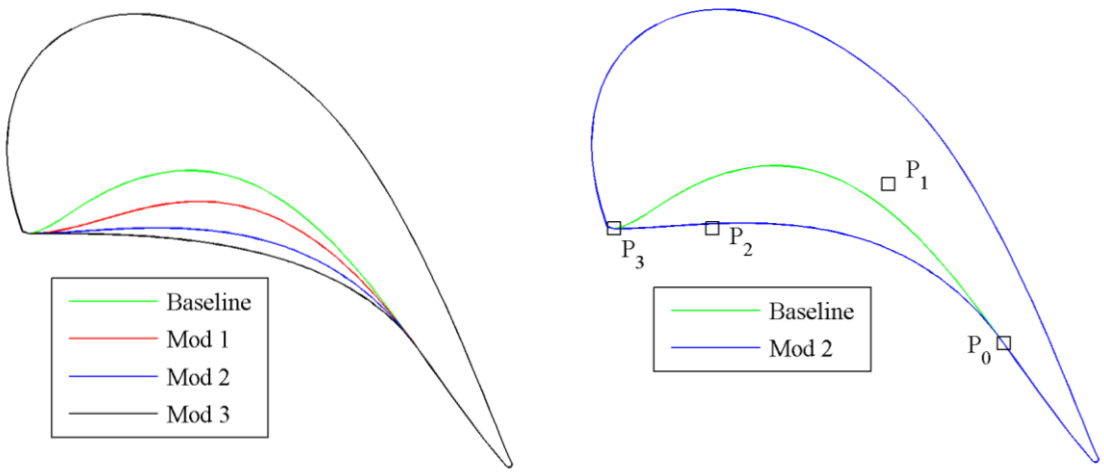

a) Pressure surface modifications b) Control point placement

Fig. K.4 Illustration of pressure surface modifications to the baseline low stagger profile along with cubic Bezier curve control points

I used cubic Bezier curves to modify the baseline profile, beginning at point P_0 in Fig. K.4b (x/C_{ax} = 0.81) aft of bubble reattachment, up to point P_3 at the leading edge. As shown in Fig. K.4b, the slope of the pair of control points at each end of the Bezier curve determines the slope of the new pressure surface at the endpoints. The distance between the pairs of control points at each end of the curve determines the amount of curvature. For all modified profile shapes of Fig. K.4a, I set the slope to zero for the line connecting points P_2 and P_3, with the length equal to $0.2C_{ax}$. The slope of the line connecting points P_0 and P_1 equaled the slope of the pressure surface aft of P_0. Modifications one to three in Fig. K.4a resulted from setting the length between points P_0 and P_1 to 0.6, 0.4, and $0.3C_{ax}$, respectively.

Predictions of Y_{2D} and Y_{ew} computed using LEO for the baseline and modified profiles are shown in Fig. K.5. As shown, Y_{2D} is significantly reduced for all the modified profiles. Both Mod 1 and Mod 2 have equal Y_{2D} that is 14% lower than the

baseline design. The predicted Y_{2D} increases by about 1% for Mod 3 compared to Mod 1 and Mod 2. Only Mod 2 and Mod 3 have reduced Y_{ew} compared to the baseline design, both having 6.7% reductions in Y_{ew}. Overall, the Mod 2 design has the lowest overall passage loss and is therefore selected as the new profile design. This new profile is designated as L2F-LS ("L2F-Low Stagger").

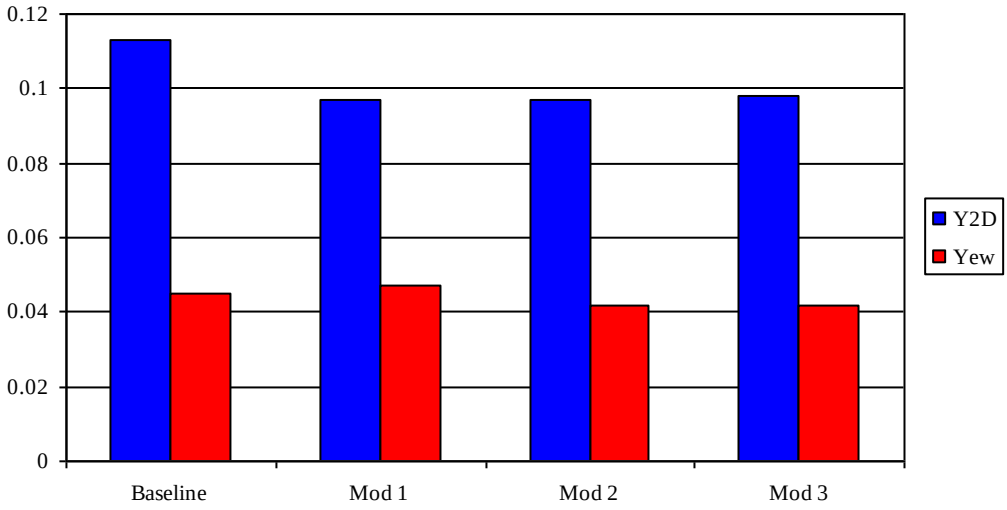

Fig. K.5 Predictions using LEO (Re = 100k) of Y_{2D} and Y_{ew} of the new baseline profile and modified designs

The loss reduction of L2F-LS compared to the baseline design is most likely due to eliminating the pressure surface separation bubble. Figure K.6 shows Y contour plots of the baseline and L2F-LS profiles indicating the absence of the high loss region adjacent to the pressure surface of L2F-LS. Figure K.7a shows that the pressure surface modification had a negligible influence on the pressure loading, and hence caused no change to the BLFP number. Therefore, the modified profile is still expected to perform well at low Re. As shown in Fig. K.7b, Reynolds lapse predictions using TDAAS indicate that L2F-LS maintains good low Re performance with lower Y_{2D} at high Re than

the baseline profile, consistent with the LEO predictions in Fig. K.5. In Section 8.2 I compare Y_{ps} and Y_{ew} of the new L2F-LS profile with L2F.

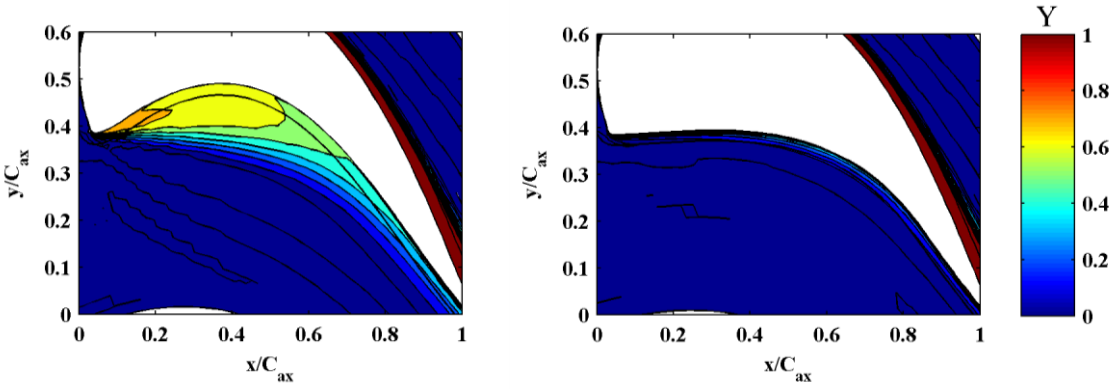

a) Baseline new profile design b) L2F-LS profile

Fig. K.6 Comparison of the baseline new profile design and the L2F-LS profile showing the elimination of the pressure surface separation bubble (Obtained using the LEO code, Re = 100k)

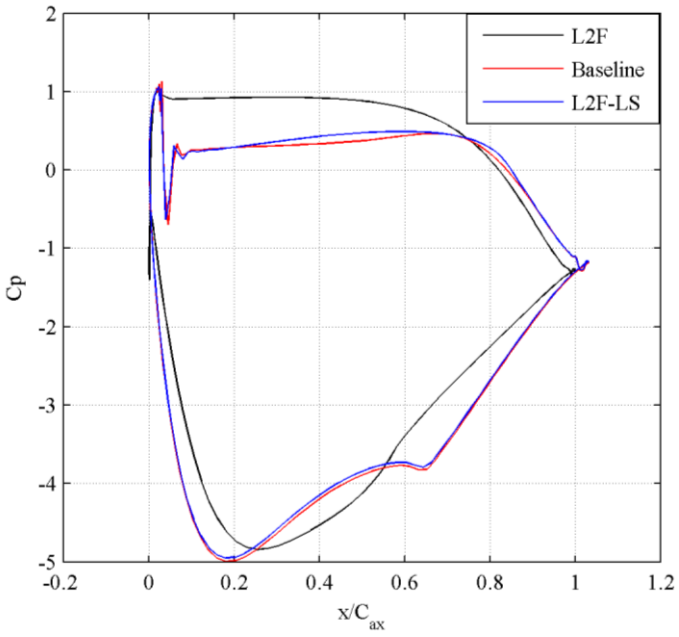

a) Pressure Loading, LEO

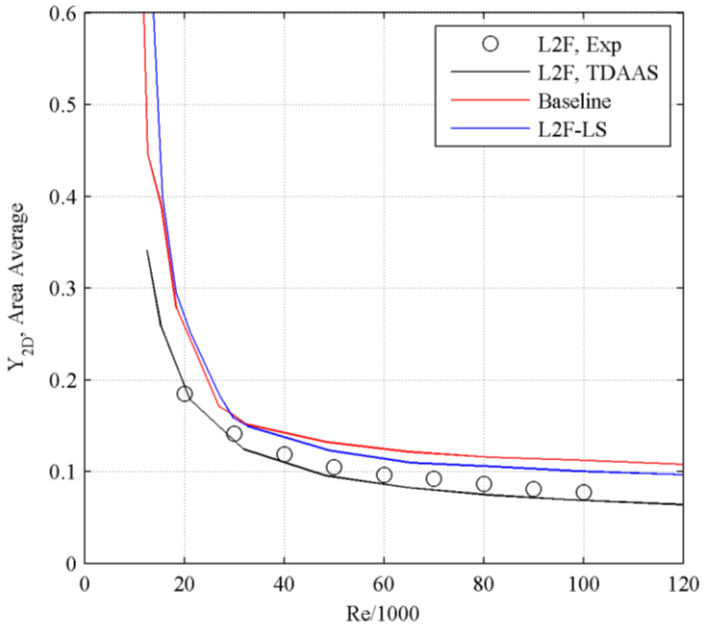

b) Reynolds lapse, TDAAS

Fig. K.7 Effect of the pressure surface modification on the pressure loading and Reynolds lapse

References

Aerodynamic Solutions Inc., 2012, http://www.aerodynamic-solutions.com/: Pleasanton, California.

Ainley, D.G., and Mathieson, G.C.R., 1951, "A Method of Performance Estimation for Axial-Flow Turbines," *Aeronautical Research Council*, R&M 2974, HMSO.

Becz, S., Majewski, M.S., and Langston, L.S., 2003, "Leading Edge Modification Effects on Turbine Cascade Endwall Loss," ASME Paper GT2003-38898.

Benner, M.W., Sjolander, S.A., and Moustapha, S.H., 2006a, "An Empirical Prediction Method for Secondary Losses in Turbines – Part I: A New Loss Breakdown Scheme and Penetration Depth Correlation," *ASME J. of Turbomachinery*, Vol. 128, pp. 273-280.

Benner, M.W., Sjolander, S.A., and Moustapha, S.H., 2006b, "An Empirical Prediction Method for Secondary Losses in Turbines – Part II: A New Secondary Loss Correlation," *ASME J. of Turbomachinery*, Vol. 128, pp. 281-291.

Blanco, E. de la Rosa, Hodson, H.P., Vazquez, R., and Torre, D., 2003, "Influence of the State of the Inlet Endwall Boundary Layer on the Interaction Between Pressure Surface Separation and Endwall Flows," Proc. Instn Mech. Engrs Vol. 217 Part A*: J. of Power and Energy*, pp. 433-441.

Bloxham, M.J., 2010, "A Global Approach to Turbomachinery Flow Control: Loss Reduction using Endwall Suction and Midspan Vortex Generator Jet Blowing," PhD Dissertation, The Ohio State University.

Bruun, H.H., 1995, "Hot-Wire Anemometry," 1st Edition. New York, New York: Oxford University Press.

Casey, M.V., 1994, "Computational Methods for Preliminary Design and Geometry Definition in Turbomachinery," in Turbomachinery Design Using CFD, AGARD Lecture Series 195, pp. 1-1:1-22.

Clark, J.P., Koch, P.J., Ooten, M.K., Johnson, J.J., Dagg, J., McQuilling, M.W., Huber, F., and Johnson, P.D., 2009, "Design of Turbine Components to Answer Research Questions in Unsteady Aerodynamics and Heat Transfer," AFRL Report No. AFRL-RZ-WP-TR-2009-2180.

Cutrone, L., De Palma, P., Pascazio, G., and Napolitano, M., 2007, "An Evaluation of Bypass Transition Models for Turbomachinery Flows," *International Journal of Heat and Fluid Flow*, Vol. 28, pp. 161-177.

Dorney, D., and Davis, R., 1992, "Navier-Stokes Analysis of Turbine Blade Heat Transfer and Performance," *ASME J. of Turbomachinery*, Vol. 114, pp. 795-806.

Dunham, J., and Came, P.M., 1970, "Improvements to the Ainley-Mathieson Method of Turbine Performance Prediction," *ASME J. of Engineering for Power*, Vol. 92, Series A, No. 3, pp. 252-256.

Gieseke, I.C., and Guezennec, 1993, "An Experimental Approach to the Calibration and Use of Triple Hot-Wire Probes," *Experiments in Fluids*, Vol. 14, pp. 305-315.

Harrison, S., 1990, "Secondary Loss Generation in a Linear Cascade of High-Turning Turbine Blades," *ASME J. of Turbomachinery*, Vol. 112, pp. 618-624.

Harvey, N.W., Rose, M.G., Taylor, M.D., Shahpar, S., Hartland, J., and Gregory-Smith, D.G., 2000, "Non-Axisymmetric Turbine Endwall Design: Part I – Three-Dimensional Linear Design System," *ASME J. of Turbomachinery*, Vol. 122, pp. 278-285.

Hill, P.G., and Peterson, C.R., 1992, "Mechanics and Thermodynamics of Propulsion," 2nd Edition. Reading, Massachusetts: Addison-Wesley Publishing Company, Inc.

Hinze, J.O., 1975, "Turbulence," 2nd Edition. New York, New York: McGraw Hill.

Hirsch, C., 2007, "Numerical Computation of Internal & External Flows – The Fundamentals of Computational Fluid Dynamics," 2nd Edition. Oxford, UK: Elsevier, p. 596.

Hodson, H.P., and Dominy, R.G., 1987, "Three-Dimensional Flow in a Low-Pressure Turbine Cascade at its Design Condition," *ASME J. of Turbomachinery*, Vol. 109, pp. 177-185.

Howell, R.J., Hodson, H.P., Schulte, V., Stieger, R.D., Schiffer, H., Haselbach, F., and Harvery, N.W., 2002, "Boundary Layer Development in the BR710 and BR715 LP Turbines—The Implementation of High-Lift and Ultra-High-Lift Concepts," *ASME J. of Turbomachinery*, Vol. 124, pp. 385-392.

Ibrahim, M., Kartuzova, O., and Volino, R.J., 2008, "Experimental and Computational Investigations of Separation and Transition on a Highly Loaded Low-Pressure Turbine Airfoil: Part I – Low Freestream Turbulence Intensity," ASME Paper No. IMECE2008-68879.

Jorgensen, F.E., 1971, "Directional Sensitivity of Wire and Fiber-Film Probes," DISA Information, Vol. 11, pp. 31-37

Kacker, S.C., and Okapuu, U., 1982, "A Mean Line Prediction Method for Axial Flow Turbine Efficiency," *ASME J. of Engineering for Power*, Vol. 104, pp. 111-119.

Kline, S.J., and McClintock, F.A., 1953, "Describing Uncertainties in Single Sample Experiments," *Mechanical Engineering*, Vol. 75.

Knezevici, D.C., Sjolander, S.A., Praisner, T.J., Allen-Bradley, E., and Grover, E.A., 2008, "Measurements of Secondary Losses in a Turbine Cascade with the Implementation of Non-Axisymmetric Endwall Contouring," ASME Paper GT2008-51311.

Knezevici, D.C., Sjolander, S.A., Praisner, T.J., Allen-Bradley, E., and Grover, E.A., 2009, "Measurements of Secondary Losses in a High-Lift Front-Loaded Turbine Cascade with the Implementation of Non-Axisymmetric Endwall Contouring," ASME Paper GT2009-59677.

Korakianitis, T., 1993, "Prescribed-Curvature-Distribution Airfoils for the Preliminary Geometric Design of Axial-Turbomachinery Cascades," *ASME J. of Turbomachinery*, Vol. 115, pp. 325-333.

Korakianitis, T., and Papagiannidis, P., 1993, "Surface-Curvature-Distribution Effects on Turbine-Cascade Performance," *ASME J. of Turbomachinery*, Vol. 115, pp. 334-340.

Langston, L.S., 2001, "Secondary Flows in Axial Turbines – A Review," Anals New York Academy of Sciences, Vol. 934, *Heat Transfer in Gas Turbine Systems*, pp. 11-26.

Lekakis, I.C., Adrian, R.J., and Jones, B.G., 1989, "Measurement of Velocity Vectors with Orthogonal and Non-Orthogonal Triple-Sensor Probes," *Experiments in Fluids*, Vol. 7, pp. 228-240.

MacIsaac, G.D., Sjolander, S.A., and Praisner, T.J., 2010, "Measurements of Losses and Reynolds Stresses in the Secondary Flow Downstream of a Low-Speed Linear Turbine Cascade," ASME Paper GT2010-22727.

Marks, C., Sondergaard, R., Wolff, M., and Estevadeordal, J., 2009, "PIV Investigation of a Highly-Loaded LPT Blade Using a Curved Laser-Sheet," AIAA Paper 2009-0301.

McQuilling, M., 2007. "Design and Validation of a High Lift Low-Pressure Turbine Blade," PhD Thesis, Wright State University, Dayton, OH.

Moffat, R.J., 1988, "Describing the Uncertainties in Experimental Results," *Experimental and Thermal Fluid Science*, Vol. 1, pp. 3-17.

Moore, J., and Adhye, R.Y., 1985, "Secondary Flows and Losses Downstream of a Turbine Cascade," *ASME J. of Engineering for Gas Turbines and Power*, Vol. 107, pp. 961-968.

Moore, J., Shaffer, D.M., and Moore, J.G., 1987, "Reynolds Stresses and Dissipation Mechanisms Downstream of a Turbine Cascade," *ASME J. of Turbomachinery*, Vol. 109, pp. 258-267.

Narasimha, R., and Prasad, S.N., 1994, "Leading Edge Shape for Flat Plate Boundary Layer Studies," *Experiments in Fluids*, Vol. 17, No. 5, pp. 358-360.

NASA, 2002, "Photo Collection for the X-31 EFMD Enhanced Fighter Maneuverability Demonstrator," http://www.dfrc.nasa.gov/gallery/photo/X-31/HTML/EC93-42024-4.html.

Panton, R.L., 1996, "Incompressible Flow", 2nd Edition. New York, New York: John Wiley & Sons, Inc.

Pope, S.B., 2000, "Turbulent Flows," 1st Edition. Cambridge, UK: Cambridge University Press.

Praisner, T.J., and Clark, J.P., 2007, "Predicting Transition in Turbomachinery – Part I: A Review and New Model Development," *ASME J. of Turbomachinery*, Vol. 129, pp. 1-13.

Praisner, T.J., Allen-Bradley, E., Grover, E.A., Knezevici, D.C., and Sjolander, S.A., 2007, "Application of Non-axisymmetric Endwall Contouring to Conventional and High-Lift Turbine Airfoils," ASME Paper GT2007-27579.

Praisner, T.J., Grover, E.A., Knezevici, D.C., Popovic, I., Sjolander, S.A., Clark, J.P., and Sondergaard, R., 2008, "Toward the Expansion of Low-Pressure Turbine Airfoil Design Space," ASME Paper No. GT2008-50898.

Prümper, H., 1972, "Application of Boundary Layer Fences in Turbomachinery," AGARD-AG-164, pp. 311-331.

Roach, P.E., 1987, "The Generation of Nearly Isotropic Turbulence by Means of Grids," *International Journal of Heat and Fluid Flow*," Vol. 8, No. 2, pp. 82-92.

Sanders, D.D., O'Brien, W.F., Sondergaard, R., Polanka, M.D., and Rabe, D.C., 2009, "A Mixing Plane Model Investigation of Separation and Transitional Flow at Low Reynolds Numbers in a Multistage Low Pressure Turbine," AIAA Paper 2009-1467.

Sanders, D.D., O'Brien, W.F., Sondergaard, R., Polanka, M.D., and Rabe, D.C., 2011, "Predicting Separation and Transitional Flow in Turbine Blades at Low Reynolds Numbers – Part I: Development of Prediction Methodology," ASME J. of Turbomachinery, Vol. 133, pp. 031011-1:031011-10.

Santner, T.J., Williams, B.J., and Notz, W.I., 2003, "The Design and Analysis of Computer Experiments," New York, New York: Springer-Verlag.

Schlichting, H., and Gersten, K, 2000, "Boundary Layer Theory," 8th Edition. Berlin, Germany: Springer-Verlag.

Sharma, O.P. and Butler, T.L., 1987, "Predictions of Endwall Losses and Secondary Flows in Axial Flow Turbine Cascades," *ASME J. of Turbomachinery,* Vol. 109, pp. 229-236.

Sondergaard, R., 2008, "LPT Flow Control at AFRL," AIAA Paper 2009-4156.

Tannehill, J.C., Anderson, D.A., and Pletcher, R.H., 1997, "Computational Fluid Mechanics and Heat Transfer," 2nd Edition. Philadelphia, Pennsylvania: Taylor & Francis.

Tritton, D.J., 1988, "Physical Fluid Dynamics," 2nd Edition. New York, New York: Oxford University Press.

Vanderplaats, G.N., 1984, "Numerical Optimization Techniques for Engineering Design: With Applications," New York, New York: McGraw Hill.

Walters, D.K., and Leyled, J.H., 2004, "A New Model for Boundary Layer Transition Using a Single-Point RANS Approach," *ASME J. of Turbomachinery,* Vol. 126, pp. 193-202.

Walters, D.K., and Leylek, J.H., 2005, "Computational Fluid Dynamics Study of Wake-Induced Transition on a compressor-Like Flat Plate," *ASME J. of Turbomachinery,* Vol. 127, pp. 52-63.

Weiss, A.P. and Fottner, L., 1995, "The Influence of Load Distribution on Secondary Flow in Straight Turbine Cascades," *ASME J. of Turbomachinery,* Vol. 117, pp. 133-141.

Wilcox, D.C., 1998, "Turbulence Modeling for CFD," 2nd Edition. La Cañada, California: DCW Industries Inc.

Wilcox, D.C., 2006, "Turbulence Modeling for CFD," 3rd Edition. La Cañada, California: DCW Industries Inc.

Wilson, D.G. and Korakianitus, T., 1998, "The Design of High-Efficiency Turbomachinery and Gas Turbines," 2nd Edition. Upper Saddle River, New Jersey: Prentice Hall Inc.

Zess, G.A., and Thole, K.A., 2002, "Computational Design and Experimental Evaluation of Using a Leading Edge Fillet on a Gas Turbine Vane," *ASME J. of Turbomachinery*, Vol. 124, pp. 167-175.

Zoric, T., Popovic, I., Sjolander, S.A., Praisner, T., and Grover, E., 2007 "Comparative Investigation of Three Highly Loaded LP Turbine Airfoils: Part I – Measured Profile and Secondary Losses at Design Incidence," ASME Paper GT2007-27537.

REPORT DOCUMENTATION PAGE

Form Approved
OMB No. 0704-0188

1. REPORT DATE *(DD-MM-YYYY)*	**2. REPORT TYPE**	**3. DATES COVERED** *(From - To)*
30-08-2012	Doctoral Dissertation	Sep 2009 - Sep 2012

4. TITLE AND SUBTITLE

Effects of Front-Loading and Stagger Angle on Endwall Losses of High Lift Low Pressure Turbine Vanes

5a. CONTRACT NUMBER

5b. GRANT NUMBER

5c. PROGRAM ELEMENT NUMBER

6. AUTHOR(S)

Lyall, M. Eric, Captain, USAF

5d. PROJECT NUMBER

5e. TASK NUMBER

5f. WORK UNIT NUMBER

7. PERFORMING ORGANIZATION NAME(S) AND ADDRESS(ES)

Air Force Institute of Technology
Graduate School of Engineering and Management (AFIT/EN)
2950 P Street, Building 640
WPAFB, OH 45433

8. PERFORMING ORGANIZATION REPORT NUMBER

AFIT/DS/ENY/12-05

9. SPONSORING / MONITORING AGENCY NAME(S) AND ADDRESS(ES)

Air Force Research Laboratory
Aerospace Systems Directorate, Turbomachinery Branch (AFRL/RQTT)
Attn: Dr. Rolf Sondergaard
1950 5th St, Bldg 18 DSN: 785-7190
WPAFB, OH 45433 Email: rolf.sondergaard@wpafb.af.mil

10. SPONSOR/MONITOR'S ACRONYM(S)

AFRL/RQTT

11. SPONSOR/MONITOR'S REPORT NUMBER(S)

12. DISTRIBUTION / AVAILABILITY STATEMENT

APPROVED FOR PUBLIC RELEASE; DISTRIBUTION UNLIMITED

13. SUPPLEMENTARY NOTES

14. ABSTRACT

Past efforts to reduce the airfoil count in low pressure turbines have produced high lift profiles with unacceptably high endwall loss. The purpose of the current work is to suggest alternative approaches for reducing endwall losses. The effects of the fluid mechanics and high lift profile geometry are considered. Mixing effects of the mean flow and turbulence fields are decoupled to show that mean flow shear in the endwall wake is negligible compared to turbulent shear, indicating that turbulence dissipation is the primary cause of total pressure loss. The mean endwall flow field does influence total pressure loss by causing excessive wake growth and perhaps outright separation on the suction surface. For equivalent stagger angles, a front-loaded high lift profile will produce less endwall loss than one aft-loaded, primarily by suppressing suction surface flow separation. Increasing the stagger setting, however, increases the endwall loss due to the static pressure field generating a stronger blockage relative to the incoming endwall boundary layer flow and causing a larger mass of fluid to become entrained in the horseshoe vortex. In short, front-loading the pressure distribution suppresses suction surface separation whereas limiting the stagger angle suppresses inlet boundary layer separation. Results of this work suggest that a front-loaded low stagger profile be used at the endwall to reduce the endwall loss.

15. SUBJECT TERMS

low pressure turbine, high lift LPT airfoils, endwall loss reduction, LPT endwall loss

16. SECURITY CLASSIFICATION OF:			**17. LIMITATION OF ABSTRACT**	**18. NUMBER OF PAGES**	**19a. NAME OF RESPONSIBLE PERSON**
a. REPORT	**b. ABSTRACT**	**c. THIS PAGE**			Paul I. King (ENY)
U	U	U	UU	211	**19b. TELEPHONE NUMBER** *(include area code)* (937) 255-3636, ext 4628